MINISTÉRIO DA CIÊNCIA, TECNOLOGIA E INOVAÇÃO
INSTITUTO NACIONAL DE PESQUISAS ESPACIAIS

sid.inpe.br/mtc-m21d/2023/02.14.14.53-TDI

CHARACTERIZATION OF X-RAY EMISSIONS ASSOCIATED WITH NATURAL LIGHTNING

Edith Tueros Cuadros

Doctorate Thesis of the Graduate Course in Space Geophysics, guided by Drs. Marcelo Magalhães Fares Saba, and Joseph R. Dwyer, approved in December 16, 2022.

URL of the original document:
<http://urlib.net/8JMKD3MGP3W34T/48HEE9E>

INPE
São José dos Campos
2023

PUBLISHED BY:

Instituto Nacional de Pesquisas Espaciais - INPE
Coordenação de Ensino, Pesquisa e Extensão (COEPE)
Divisão de Biblioteca (DIBIB)
CEP 12.227-010
São José dos Campos - SP - Brasil
Tel.:(012) 3208-6923/7348
E-mail: pubtc@inpe.br

MINISTÉRIO DA CIÊNCIA, TECNOLOGIA E INOVAÇÃO
INSTITUTO NACIONAL DE PESQUISAS ESPACIAIS

sid.inpe.br/mtc-m21d/2023/02.14.14.53-TDI

CHARACTERIZATION OF X-RAY EMISSIONS ASSOCIATED WITH NATURAL LIGHTNING

Edith Tueros Cuadros

Doctorate Thesis of the Graduate Course in Space Geophysics, guided by Drs. Marcelo Magalhães Fares Saba, and Joseph R. Dwyer, approved in December 16, 2022.

URL of the original document:
<http://urlib.net/8JMKD3MGP3W34T/48HEE9E>

INPE
São José dos Campos
2023

Cataloging in Publication Data

Tueros Cuadros, Edith.

T814c Characterization of X-Ray emissions associated with natural lightning / Edith Tueros Cuadros. – São José dos Campos : INPE, 2023.

xx + 99 p. ; (sid.inpe.br/mtc-m21d/2023/02.14.14.53-TDI)

Thesis (Doctorate in Space Geophysics) – Instituto Nacional de Pesquisas Espaciais, São José dos Campos, 2022.

Guiding : Drs. Marcelo Magalhães Fares Saba, and Joseph R. Dwyer.

1. X-rays. 2. Runaway electrons. 3. Return stroke. 4. Dart-stepped-leader. 5. Monte Carlo. I.Title.

CDU 551.594

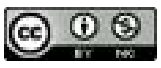

MINISTÉRIO DA CIÊNCIA, TECNOLOGIA E INOVAÇÃO

INSTITUTO NACIONAL DE PESQUISAS ESPACIAIS
Serviço de Pós-Graduação - SEPGR

DEFESA FINAL DE TESE DE EDITH TUEROS CUADROS
REG. 132292/2018, BANCA Nº 335/2022

No dia 16 de dezembro de 2022, por teleconferência, o(a) aluno(a) mencionado(a) acima defendeu seu trabalho final (apresentação oral seguida de arguição) perante uma Banca Examinadora, cujos membros estão listados abaixo. O(A) aluno(a) foi APROVADO(A) pela Banca Examinadora, por unanimidade, em cumprimento ao requisito exigido para obtenção do Título de Doutora em Geofísica Espacial/Ciências Atmosféricas. O trabalho precisa da incorporação das correções sugeridas pela Banca Examinadora e revisão final pelo(s) orientador(es).

Novo Título: "Characterization of X-Ray emissions associated with natural lightning"

Membros da banca:

Dra. Inez Staciarini Batista - Presidente - INPE
Dr. Marcelo Magalhães Fares Saba - Orientador - INPE
Dr. Joseph R. Dwyer - Orientador - University New Hampshire/Department of Physics and Astronomy
Dr. Severino Luiz Guimaraes Dutra - Membro Interno - INPE
Dr. Miguel de Brito Guimarães Neto - Membro Externo - CEFET/MG
Dr. István Kérészy - Membro Externo - University Florida

Declaração do orientador Joseph R. Dwyer e de István Kérészy anexas ao processo.

Documento assinado eletronicamente por **Inez Staciarini Batista (E)**, **Usuário Externo**, em 06/04/2023, às 08:42 (horário oficial de Brasília), com fundamento no § 3º do art. 4º do Decreto nº 10.543, de 13 de novembro de 2020.

Documento assinado eletronicamente por **Miguel de brito guimaraes neto (E)**, **Usuário Externo**, em 06/04/2023, às 09:51 (horário oficial de Brasília), com fundamento no § 3º do art. 4º do Decreto nº 10.543, de 13 de novembro de 2020.

Documento assinado eletronicamente por **Severino Luiz Guimarães Dutra (E)**, **Usuário Externo**, em 06/04/2023, às 21:28 (horário oficial de Brasília), com fundamento no § 3º do art. 4º do Decreto nº 10.543, de 13 de novembro de 2020.

Documento assinado eletronicamente por **Marcelo Magalhães Fares Saba**, **Pesquisador**, em 13/04/2023, às 16:07 (horário oficial de Brasília), com fundamento no § 3º do art. 4º do Decreto nº 10.543, de 13 de novembro de 2020.

A autenticidade deste documento pode ser conferida no site https://sei.mcti.gov.br/verifica.html, informando o código verificador **10972295** e o código CRC **33963E94**.

Referência: Processo nº 01340.010163/2022-26 SEI nº 10972295

Dedicated to my professor, Jean-Pierre Raulin, and my Master's partner, Ray Fernando, for their invaluable support throughout my academic journey. Their constructive criticisms and insightful advice have been a guide for me, providing me with the motivation and determination to overcome challenges and complete my Ph.D. I am deeply appreciative of those criticisms which have helped me develop my research skills.

ACKNOWLEDGEMENTS

After reading the title of the thesis, the reading of the acknowledgments is next. And writing it is without a doubt the most difficult part of writing. While I'm sure I'll forget someone, keep in mind that it wasn't a bad intention, but the age and mental state of a Ph.D. student after writing this thesis.

First, I thank God for everything he has given me in this life, for my family and me, for the achievements so far, but I ask Him to provide me with the wisdom to achieve much more.

I want to thank my advisor, Dr. Marcelo Magalhães Fares Saba, for letting me choose and accepting to do this new research topic, which was both pleasant and very difficult. In addition, this work allows me to preserve everything, learn more about my skills, and develop a passion for the relationship between lightning and particle physics. My deep gratitude, admiration, and respect for my co-advisor Dr. Joseph R. Dwyer, for the enriching conversations, always pertinent advice, and observations that clarified many doubts and enriched knowledge. Without the support and patience in explaining the behavior of physical phenomena during my stay in the United States, it would not have been possible to carry out part of my Ph.D.

To the professors of the Space Geophysics course at INPE, especially to professors Cristiano, and Virginia, for their words and help in all the bureaucratic procedures to be able to do a sandwich doctorate.

To my friends in the house that I share, they have become my family. I am incredibly grateful to them for their company and long conversations throughout the doctoral stage with Julia, Palmira, Daniele, Gisele, and Geane.

To my colleagues and friends from the Geophysics course and other areas at INPE, Hadassa, Daniele, Adriany, Paulo, Amanda, Saúl, Adriano, Arturo, Isela, Jonas, Mateus, Rafael, William, Guilherme, Michael, David, João, Tagianne, Ivan all old friends and recent ones that I have fun with at INPE.

To Lucíola, and Carol, my friends from Mackenzie University, for always helping with some bureaucratic issues at CAPES or CNPq, and for their availability and conversations.

To Walter Guevara, my teacher and friend, my gratitude for the trust and motivation provided.

To my great friends and partners in every madness in this stage called life, Deysi, Liliana, Cristian, Riano, José, Ray, Josue, and Martin, great people who are always waiting for me despite the distance at every moment.

To Professor Marco Ferro, and my friend Paulo for their help in calibrating the instruments.

To my friends at the University of New Hampshire whom I met during my sandwich Ph.D. stay, Taheo, Nicholas, Emily, Cristin, Karla, Alma, David, Suellen, Mauro, Ady, Eduardo, Samuel, Dianne, Mary, Ginny and Thener my gratitude, for the trust, help and funny conversations about science and soccer.

To the examining board members of this work who contributed with valuable suggestions.

Finally, I thank CAPES (Coordination for the Improvement of Higher Education Personnel) and CNPq (National Council for Scientific and Technological Development) for the essential and indispensable financial support during my Ph.D.

ABSTRACT

Lightning produces x-rays. However, the physical processes involved in this production are still poorly understood. The goal of this work is to characterize the x-ray emissions related to natural lighting, and for that, collected data and simulations were used. In Brazil, two occurrences of x-rays were recorded for the first time. X-ray events were recorded on December 16, 2018 (18:43:37 UT) and on January 24, 2019 (17:52:20 UT), using the x-ray sensors, electric field, high-speed and common video cameras in the building located in São Paulo, called P1P2. In the first event, the first three return strokes of the lightning that produced x-rays followed different paths, but the fourth stroke, which followed the initial part of the path of the first return stroke, began to propagate towards the ground and branch out during its propagation. The recorded x-rays were produced by the fifth return stroke, generating a high current (-38 kA) compared to the other return strokes. In the second event, all lightning strikes that produced x-rays followed the same path as the first return stroke. Recorded x-rays were produced by the second, third and sixth return strokes, generating high currents of $\sim$ -20, -91, and -46 kA, compared to the other return strokes. In both cases, the x-ray emissions were produced by the dart-stepped leader, which occurred approximately 100 to 330 μs before the return strokes. From the first event, we concluded that the x-rays were recorded only when the leader tip was in a certain portion of the lightning channel confirming that the leader orientation plays an important role in the detection of x-rays. Based on this statement, we modeled the leader propagation using Monte Carlo simulation. In this case, we consider only photon interaction in order to know how the x-rays are emitted and what behavior we should have when modeling the optical data, later comparing them with the data recorded by the x-ray sensors. This comparison was done for the first time, so we found some limitations in the data comparison. Even so, we can conclude that the predominant physical processes in the leader propagation channel can be attributed to the Compton effect and pair creation. Furthermore, based on the results of our theoretical simulations, we can conclude that the energy of photons produced by lightning varies between 10^3 and 10^7 KeV at a given altitude (from 0 to 1000 m).

Keywords: X-rays. Runaway Electrons. Return Stroke. Dart-stepped-leader. Monte Carlo.

CARACTERIZACÃO DAS EMISSÕES DE RAIOS-X ASSOSIADOS A RELÂMPAGOS

RESUMO

As descargas atmosféricas produzem raios-x. No entanto, os processos físicos envolvidos nessa produção ainda são pouco compreendidos. O objetivo deste trabalho foi caracterizar as emissões de raios-x relacionadas com os raios naturais, e para isso, foram usados dados coletados e simulações. No Brasil, duas ocorrências de raio-x foram registradas pela primeira vez. O primeiro evento de raios-x foi registrado no dia 16 de dezembro de 2018 (18:43:37 UT) e o segundo evento de raios-x foi registrado no dia 24 de janeiro de 2019 (17:52:20 UT) com os sensores de raios-x, campo elétrico e dois tipos de câmeras (de alta velocidade e comum), no prédio localizado na cidade de São Paulo, chamado P1P2. No primeiro evento, as três primeiras descargas do raio que produziu raios-x seguiram caminhos diferentes, a quarta descarga, após seguir a parte inicial do caminho da primeira descarga de retorno, iniciou um novo caminho para o solo e se ramificou durante sua propagação. O raios-x registrados foram produzidos pela quinta descarga, gerando uma corrente alta (-38 kA) em comparação com as demais descargas de retorno. No segundo evento, todas as descargas do raio que produziram raios-x seguiram o mesmo caminho da primeira descarga de retorno. Os raios-x registrados foram produzidos pela segunda, terceira e sexta descarga de retorno, gerando correntes altas de $\sim$ -20, -91 e -46 kA, em comparação às demais descargas de retorno. Em ambos os casos, raios-x foram produzidos pelos *dart-stepped leader* e começaram aproximadamente 100 a 330 μs antes da descarga de retorno. Por outro lado, do primeiro evento concluímos que os raios-x foram registrados apenas quando a ponta do líder estava em uma determinada porção do canal do relâmpago confirmando que a orientação do líder desempenha um papel importante na detecção de raios-x. Baseado nessa afirmação, fizemos a modelagem de propagação do líder usando simulação Monte Carlo. Neste caso, consideramos só interação de fotons com finalidade de conhecer como os raios-x são emitidos e qual é comportamento que deveriamos ter ao modelar os dados observados, posteriormmente compará-los com os dados registrados pelos sensores de raios-x. Esta comparação foi feita pela primeira vez, por isso, encontramos algumas limitações na comparação de dados. Mesmo assim, podemos concluir que os procesos físicos predomintantes ao modelar fotóns no canal de propagação do lider são devido ao efeito Comptom e criação de pares. Além disso, com base nos resultados de nossas simulações teóricas, podemos concluir que a energia dos fótons produzidos por um raio varia entre 10^3 e 10^7 KeV em uma determinada altitude (de 0 a 1000 m).

Palavras-chave: Raios-x. Elétrons Fugitivos. Descargas Atmosféricas. Dart-stepped-leader. Monte Carlo.

LIST OF FIGURES

Page

LIST OF TABLES

Page

LIST OF ABBREVIATIONS

BrasilDAT	–	from portuguese Rede Brasileira de Detecção de Descargas Atmosféricas
GPS	–	Global Positioning System
HV	–	High Voltage
IEAv	–	from portuguese Instituto de Estudos Avançados
INPE	–	from portuguese Instituto Nacional de Pesquisas Espaciais
ITA	–	from portuguese Instituto Tecnológico de Aeronáutica
LF	–	Low Frequency
PMT	–	Photomultiplier Tube
RINDAT	–	Rede Integrada Nacional de Detecção de Descargas Atmosféricas
RREA	–	Relativistic Runaway Electron Avalanch
RE	–	Runaway electrons
Rx	–	x-ray
REAM	–	Runaway Electron Avalanche Model
RS	–	Return stroke
STP	–	Standard Temperature and Pressure
VHF	–	Very High Frequency
VLF	–	Very Low Frequency

LIST OF SYMBOLS AND UNITS

X_0	–	Length of the Radiation
γ	–	Gamma Ray
λ_{e^-}	–	Length of the Avalanche
μ/ρ	–	Mass Attenuation Coefficient
μ	–	Linear Attenuation Coefficient
μs	–	Microseconds
ρ	–	Density
σ	–	Compton Scattering
τ	–	Photoelectric Effect
Θ	–	Angle
ε_{th}	–	Minimum Kinetic Energy of the RE
φ	–	Latitude
E_b	–	Breakeven Field
k	–	Pair Production
n_{air}	–	Air Density
eV	–	Electron Volt
GeV	–	Giga Electron Volt
I	–	Intensity
K	–	Kelvin
kA	–	Kilo Ampère
keV	–	Kilo Electron Volt
kV	–	Kilo Volt
lat	–	Latitude
lng	–	Longitude
m	–	Metros
MeV	–	Mega Electron Volt
MS	–	Mega Samples
ms	–	Millisecond
MV	–	Mega Volt
Pa	–	Pascal
s	–	Seconds

CONTENTS

1 INTRODUCTION

Benjamin Franklin was one of the first to systematically study lightning. One of nature's most fascinating and energetic phenomena is lightning, which can be classified into two types: intra-cloud and cloud-to-ground. As shown in Figure 1.1, cloud-to-ground lightning can be divided into four types based on their polarity (positive or negative) and propagation direction (upwards or downwards). The most common type of ground discharge is negative lightning (cloud-to-ground) which accounts for about 90% of all ground discharges, with the remaining 10% being positive discharges. The leader of the cloud-to-ground negative lightning is initiated inside the cloud and descends carrying a negative charge to the ground.

The initiation of lightning remains a poorly understood topic in research. It is believed that lightning involves a breakdown of the conventional dielectric strength of air, which requires an electric field of the order of 1 MV m^{-1} at typical storm cloud altitudes (between 7 and 10 km). However, various measurements have been unable to accurately characterize the storm's intense electric field. Through these measurements, electric field strengths in the range of 4.3×10^4V/m to 10^5 V/m and occasionally as high as 400 kVm^{-1} were detected (WINN; MOORE, 1971). This has led some researchers to suggest that high fields can exist locally for a short time. Cooray (2003), suggested that electric field strengths greater than those mentioned above are sufficient for the initiation and propagation of leaders through the interaction of water droplets, because the electric field polarizes the drops, deforming them, or making them elongated. The charge concentrated at the ends of the drops intensifies the field in the region close to them. The field intensity in this region reaches the necessary values to initiate the breakdown of the dielectric strength of the air. Others have suggested that lightning initiation may be triggered by cosmic rays (GUREVICH et al., 1992; GUREVICH et al., 1996).

Regardless of the initiation mechanism, the initiation of a stepped leader is marked by characteristic pulses, known as the preliminary breakout pulses, which mark the transition from the initial phase to the stepped leader phase (BEASLEY et al., 1982). After the staggered leader is formed within the cloud, it emerges from the cloud base and propagates towards the ground at a speed of about 10^5 m s^{-1}. The staggered leader advances in a series of discrete and quick steps (1 μs) separated by intervals of 10 to 50 μs, with a tendency to branch out (RAKOV; UMAN, 2003). When the leader is just over 100 m above the ground, upward positive leaders are initiated from objects on the ground and propagate to intercept the negative leader (or one

Figure 1.1 - Classification of ground discharges based on polarity and leader direction.

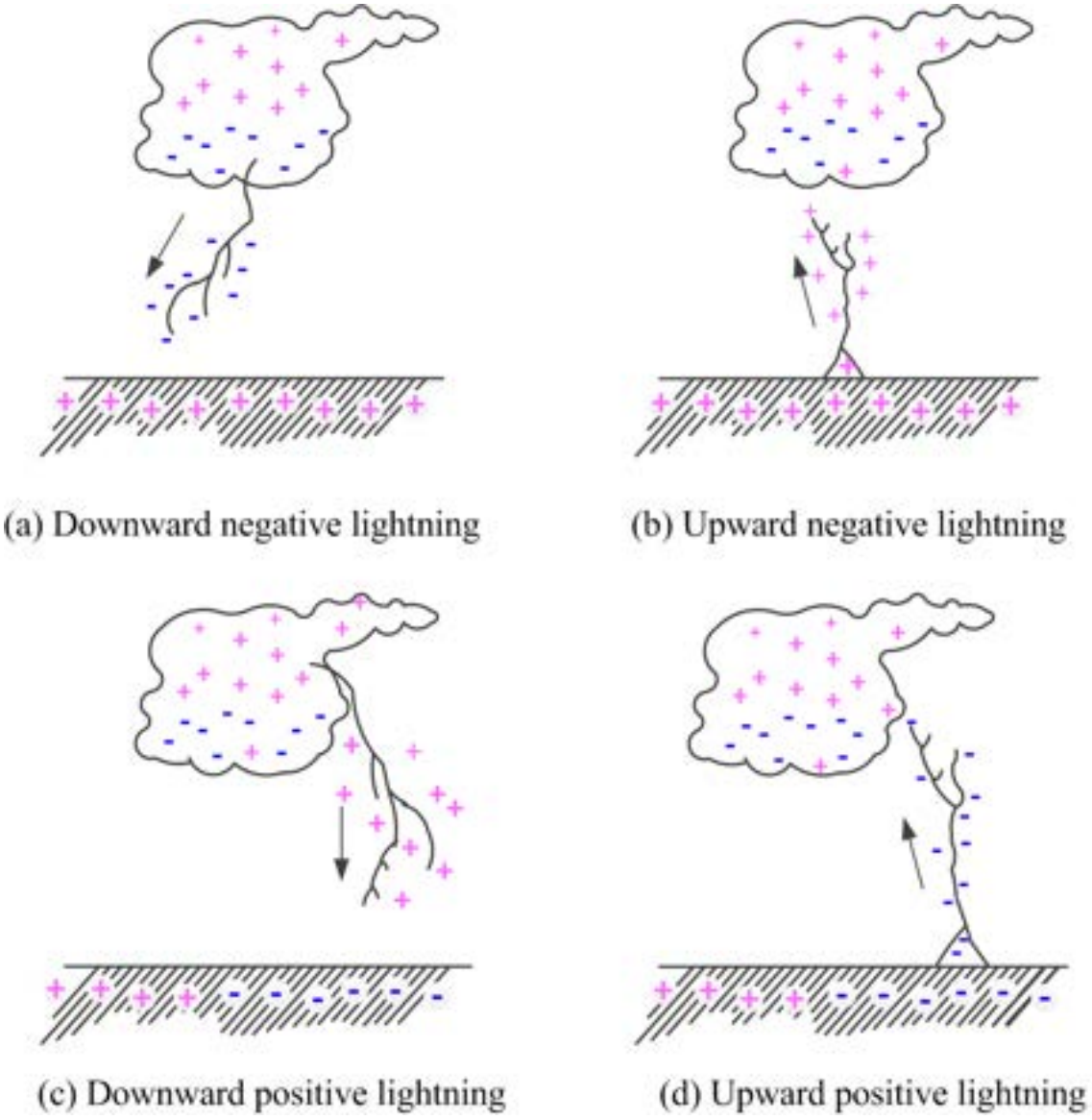

SOURCE: Adapted from Rakov and Uman (2003).

of its branches) in a process called the attachment process (JERAULD et al., 2007). Once the two leaders make contact, a bidirectional wave passes through the formed channel and neutralizes the negative charge deposited along the channel in a process called the return stroke. This sequence can be followed by more sequences of leader and return stroke movement separated by 60ms intervals. Figure 1.2, illustrates the entire sequence of events.

The field of high-energy atmospheric physics began in 1925 with Wilson's work on the production of energetic electrons in our atmosphere (WILSON, 1925). Many researchers have tried to determine whether thunderstorm clouds or lightning produce such energetic radiation. However, until the year 2000, the existence of energetic radiation from storms and especially from lightning was not accepted.

Today, after more than a decade of research, we know that high-energy radiation is commonly produced in the atmosphere and at sea level, (DWYER et al., 2012a).

1.1 X-ray record

In storm clouds, Parks et al. (1981) and McCarthy and Parks (1985), Eack et al. (1996) observed x-ray enhancements several seconds before a lightning strike occurred. Subsequently, Moore et al. (2001), reported the detection of energetic radiation emissions immediately before the first return discharge in negative lightning, and Dwyer (2003) described similar results for dart leaders in rocket-induced or stimulated lightning.

Dwyer (2004) showed that these emissions were composed of multiple, brief x-ray emissions in the range of 30 – 250 keV, with each burst typically lasting less than 1 μs. Furthermore, they showed that the source of the x-ray bursts moved from the storm clouds toward the ground, supporting the hypothesis that the front of the leader is the source of the x-rays. Dwyer and Smith (2005), Saleh et al. (2009), Mallick et al. (2012) and Hettiarachchi et al. (2018) compared to x-ray and electric field waveforms obtained simultaneously during the stepped leader phase of negative cloud-to-ground lightning and concluded that the production of x-rays is associated with the formation of leader steps.

Although many unknown atmospheric processes have been partially understood through observations and simulations, they are still far from being fully understood. Radiation is emitted at different timescales and intensities, such as x-ray emissions lasting less than microseconds. These observations and measurements paved the way for an emerging area of high-energy atmospheric physics, which addresses the production and propagation of energetic radiation, and the effects of these on atmospheric electrodynamics.

Figure 1.2 - Development of negative cloud-to-ground lightning. The time scale is given in milliseconds from the first electrical rigidity-breaking processes in the cloud.

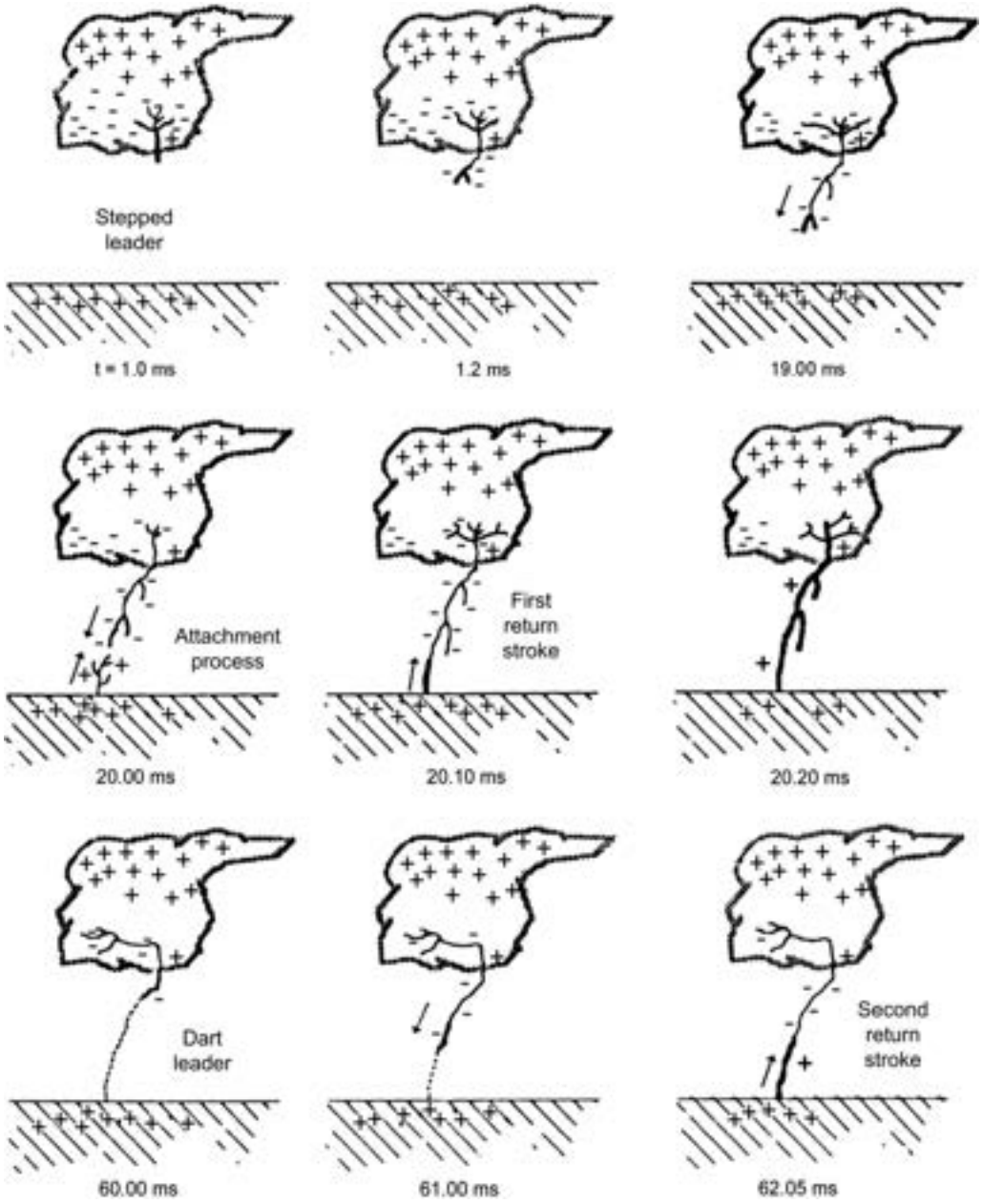

SOURCE: Adapted from Rakov and Uman (2003).

1.2 Motivation

Brazil is one of the countries with the highest incidence of lightning in the world, but most of the studies carried out in the country are focused on the protection of

buildings and other areas. In this thesis, one of the main objectives is to characterize the x-ray emissions associated with natural lightning, in this way, to obtain a better understanding of the physical mechanisms that produce these emissions and their potential impact on the Earth's atmosphere. To achieve this goal, it is necessary to observe the x-rays produced by natural atmospheric discharges, for this purpose, x-ray sensors, an electric field, different cameras, and lightning networks were used. In this way, to be able to analyze the x-ray emissions associated with natural lightning. After the record, we will focus especially on lightning that produces the x-rays, i.e. negative cloud-to-ground lightning especially on dart-stepped leaders.

In addition, x-rays produced by lightning are relevant to space weather research. Space weather is concerned with the effects of solar and cosmic ray sources on Earth's space environment, and x-rays produced by lightning can play a role in this context in several ways such as high-energy particle radiation, global electric circuit, and radiation exposure. Lightning can produce ionizing radiation, x-rays, that can pose a risk to human health. This risk is relevant not only on the ground but also in aircraft, which can be exposed to elevated levels of radiation during thunderstorms. Studying the x-rays produced by lightning can help to assess the risks of radiation exposure and develop strategies for mitigating those risks.

Therefore, x-rays produced by lightning can provide important information about the radiation properties of high-energy particles and their interactions with the Earth's environment, as well as the risks posed by ionizing radiation to human health and technology. These insights can be relevant to the study of space weather and its effects on the Earth.

1.3 Goals

Principal

Characterize the variations of x-ray emissions related to natural lightning.

Specific

- Record x-rays produced by natural lightning.
- Discriminate lightning-related x-rays from their natural background.
- Calculate the distance and orientation of the leader tip at the time of x-ray production.

- Modeling x-ray energy spectra using Monte Carlo simulation.
- Determine the luminosity and energy spectrum of the leader.

2 HIGH ENERGY PHYSICS

2.1 Runaway electrons

The frequency of collisions of an electron with ions and with other electrons in the plasma causes its speed to decrease rapidly. But friction can be neglected for electrons with sufficiently high energy. In this way, if an electric field is present in the plasma, the speed of these electrons increases continuously. These electrons are called runaway electrons (RE[1]) and constitute a key element for understanding high-energy atmospheric physics, such as the initiation and propagation of atmospheric electrical discharges commonly known as lightning.

Energetic electrons reach high energies from static fields in the air. Thus, RE is produced when the rate of energy gain from an electric field exceeds the rate of energy loss from interactions with air, in this way an electron can escape due to the increase in its energy. RE need an electric field with intensity above a break-even field, $E_b = 2,18 \times 10^5 \cdot n_{air}$ V m^{-1}, which corresponds to the minimum ionization rate, where n_{air} is the air density in relation to sea level (WILSON, 1925).

Dwyer (2003) numerically modeled the RE production mechanism taking into account the elastic scattering of electrons and including feedback from gamma rays and positrons. It has been shown that an electric field of approximately 30% greater than E_b is required for RE production. The electric field at the equilibrium point at any altitude is smaller than the electric field necessary for the breakdown of the dielectric strength and propagation of streamers. In a sample of 23 soundings, Marshall et al. (1995) confirmed that lightning occurs when the electric field exceeds the equilibrium point. They also found that the electric field inside storm clouds is smaller or comparable to the electric field at the equilibrium point. In this way, this mechanism could explain why that electric field strengths greater than $1,5 \times 10^5$ V m^{-1} are uncommon within thunderstorms and suggest a connection between lightning initiation and RE production.

Figure 2.1 shows the rate of loss of energy or effective friction force experienced by a free electron propagating in the air at standard temperature and pressure (STP[2]) *i.e.* ($T = 273$ K e $p = 10^5$ Pa), as a function of kinetic energy. The solid curve denotes the inelastic scattering of the electron due to air molecules, the dashed curve denotes the effects of Bremsstrahlung emission, while the horizontal line denotes the

[1]RE: *Runaway electrons*
[2]STP: *Standard Temperature and Pressure*

force produced by an electric field of 5×10^6 V m^{-1}. For RE to be produced, it is necessary that electrons have initial kinetic energy above the threshold ($\varepsilon > \varepsilon_{th}$). These electrons are called seed electrons *e.g.* cosmic rays or radioactive decay. It can also be seen in Figure 2.1 that when the electric field is intense enough, the required threshold energy ε_{th} is smaller. However, when the electric field intensifies above the critical level E_c, all electrons are accelerated by the electric field and become RE. This last hand mechanism requires no seed particles (GUREVICH et al., 1996).

Figure 2.1 - Effective frictional force experienced by a free electron propagating in the air at standard temperature and pressure (*i.e.* $T = 273$ k and $p = 10^5$ Pa) as a function of kinetic energy.

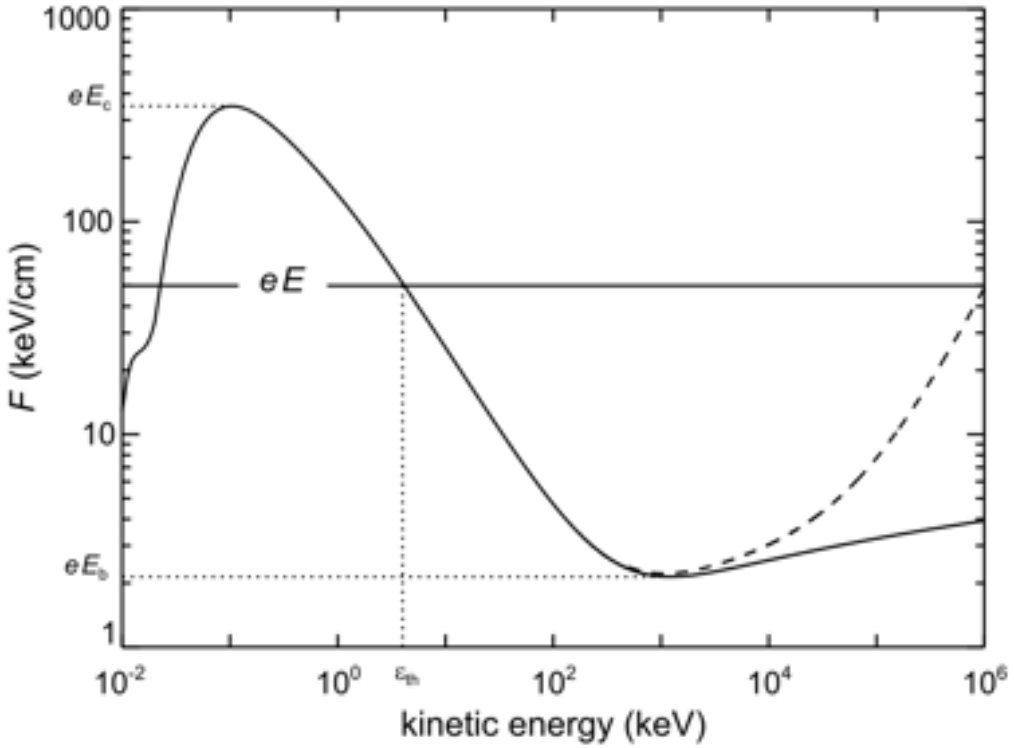

The solid curve denotes the inelastic scattering of the electron due to air molecules, the dashed curve denotes the effects of Bremsstrahlung emission, while the horizontal line denotes the force produced by an electric field of 5×10^6 V m^{-1}.

SOURCE: Dwyer (2004).

As mentioned above, cosmic rays and radioactive decay are commonly the sources of seed electrons. Thus, the secondary electrons, which are part of the cosmic ray shower in the atmosphere, produce at least one RE in a sufficiently intense electric

field (MCCARTHY; PARKS, 1992).

2.2 Avalanche of relativistic runaway electrons

The Figure 2.2 shows a schematic of an avalanche of electrons with a cosmic ray colliding with a molecule or atom in the air, releasing electrons. If an electric field is present ($E > E_{th}$), then free electrons can escape and ionize the air producing more seeds.

Considering Møller dispersion, *i.e.*, electron-electron elastic scattering, the flow of runaway electrons described by Wilson undergoes an avalanche effect, *i.e.*, an intensification of the flow of electrons due to avalanches. Thus, a large number of relativistic runaway electrons will be generated by each energetic seed electron injected into a region of intense electric field (GUREVICH et al., 1992; GUREVICH; ZYBIN, 2001). This avalanche mechanism is known as a relativistic runaway electron avalanche (RREA[3]). The threshold electric field of the runaway electron avalanche is given by the Equation 2.1, estimated by Dwyer (2003):

$$E_{th} = 2,84 \times 10^5 \cdot n_{air} \tag{2.1}$$

where n_{air} is the air density in relation to sea level and E_{th} is given in V m^{-1}.

This threshold electric field E_{th} is slightly larger than the field at the equilibrium point which is the minimum value of the ionization energy loss curve in Figure 2.1. This is the threshold electric field for the propagation of runaway electrons and the for the avalanche effect only in the ideal case where the runaway electrons move exactly along the electric field lines.

Therefore, an electric field overestimated by 30% would be required to produce runaway electrons and the avalanche effect (DWYER, 2012). On the other hand, measurements of electric field strength in storm clouds are close to the threshold electric field E_{th}, suggesting that runaway electron avalanches may be frequent within storm clouds (RAKOV; UMAN, 2003).

The numerical simulations used to characterize RREA production are continuously optimized using a larger number of parameters, including inhomogeneous electric fields and atmospheric cosmic ray seeding.

[3]RREA: *Relativistic Runaway Electron Avalanche*

Figure 2.2 - Scheme of an avalanche of runaway electrons. Initially, a cosmic ray particle strikes an incident primary air molecule.

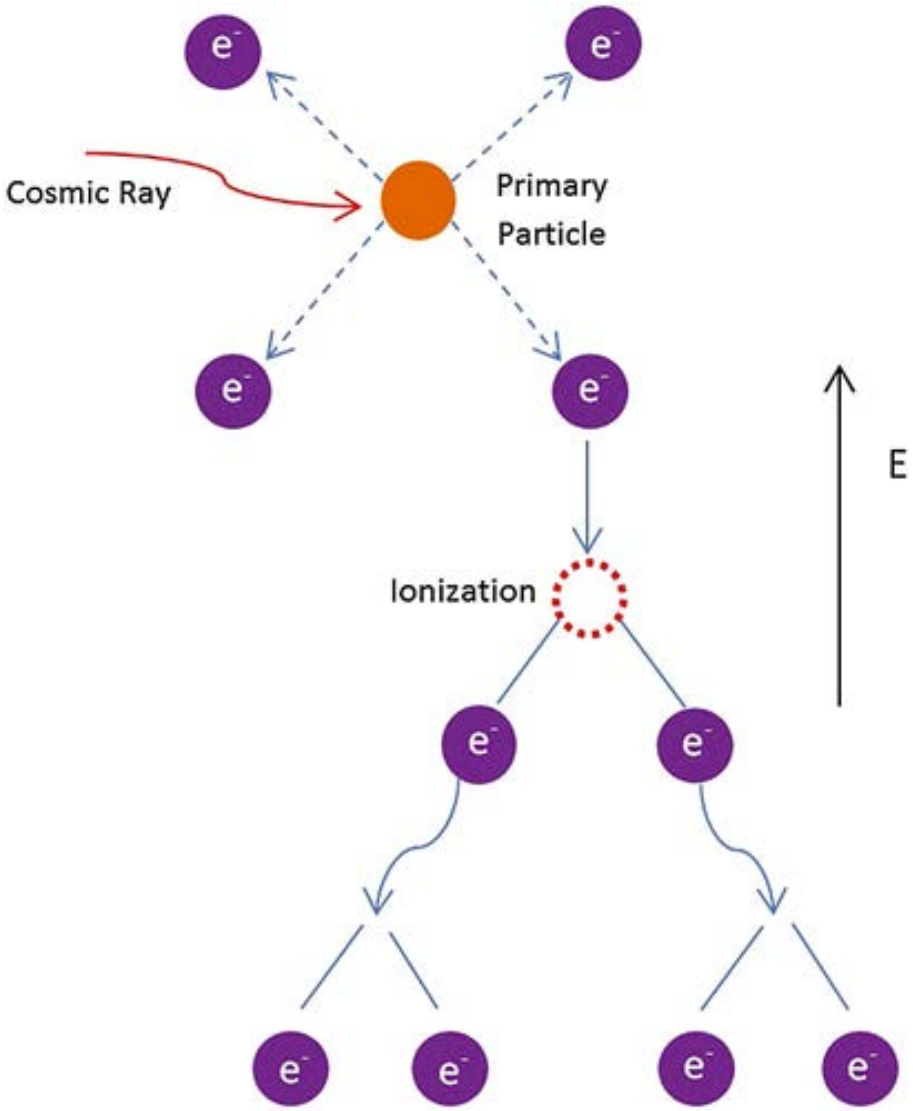

The electrons hit and ionize other atoms or molecules, creating an avalanche of secondary particles.

SOURCE: Cramer et al. (2014).

Although there are computational algorithms that use random sampling to obtain numerical results of complex problems, *e.g.* the Monte Carlo Methods, these methods do not always provide a physical understanding of the problem. Thus, to investigate the physical details responsible for the production of RREA it is necessary to define some useful parameters. The three fundamental parameters are the length of the avalanche (λ_{e^-}), the length of the radiation (X_0), and the minimum kinetic energy of the RE (ε_{th}) (DWYER et al., 2012b; CRAMER et al., 2014).

Considering in a simplified way that the RE flux due to the avalanche (F_{RREA}) is proportional to the flux of external energetic seed particles (F_0), the RE flux at the end of the avalanche region is given by (DWYER et al., 2012b):

$$F_{RREA} = F_0 \, exp \, \xi, \tag{2.2}$$

where:

$$\xi = \int_0^L \frac{dz}{\lambda} \tag{2.3}$$

where ξ is the number for which the length of the avalanche grows by a factor of e (*e-folding*) and λ is the length of the avalanche.

The avalanche length, λ_{e^-}, is a function of the electric field and describes the measure of how far an electron can travel before producing a $1 - e$ increase in the number of secondary electrons. As the electric field intensifies, more low-energy electrons are accelerated. Consequently, the length of the electron avalanche drops off rapidly for highly energetic electrons as shown in Figure 2.3. Empirically, the length of the avalanche can be written as Coleman and Dwyer (2006):

$$\lambda_{e^-} = \frac{7300 \text{ kV}}{E - E_d} \tag{2.4}$$

where E_d is the value of the electric field (276 kV m^{-1}), which generates the force $F_d = eE_d$, which balances the drag force. The speed of the avalanche is approximately constant, with a value of v = 0.89c (COLEMAN; DWYER, 2006). Figure 2.3 shows a graph of the length of the avalanche, λ_{e^-}, as a function of the strength of the

electric field at the sea level.

Figure 2.3 - Length of the avalanche as a function of the electric field.

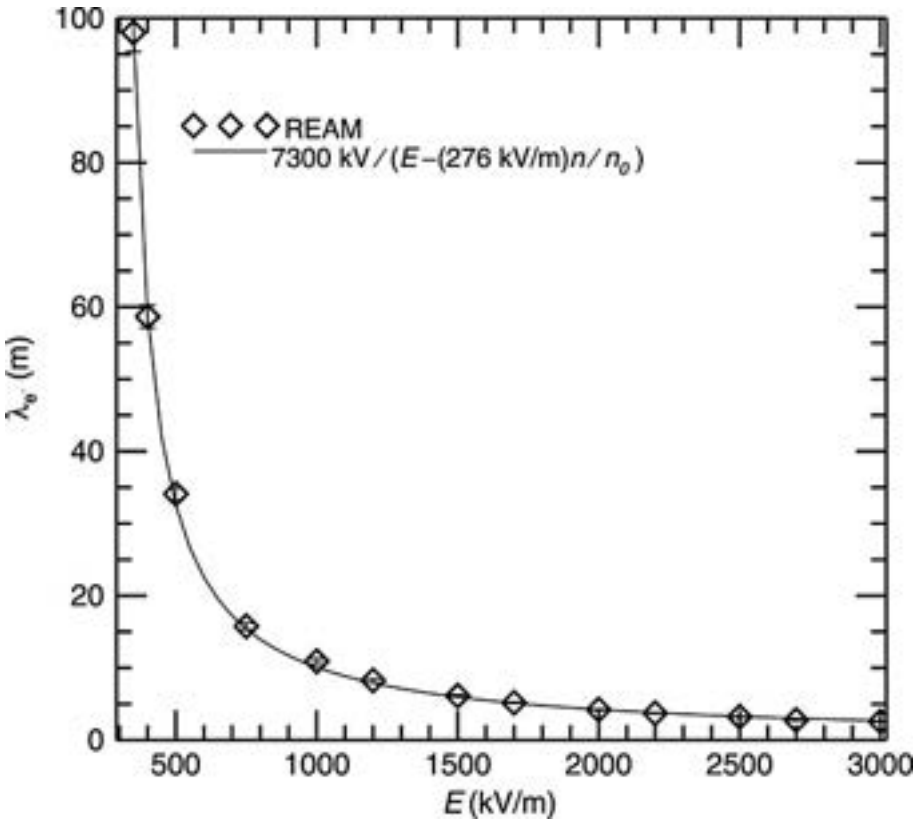

The diamonds denote the result of the relativistic avalanche model of RE while the solid curve is the empirical fit of Equation 2.4.

SOURCE: Cramer et al. (2014).

The radiation length, X_0, is defined as the distance that an electron must travel to lose e^{-1} of its initial energy due to Bremsstrahlung, given by Equation 2.5:

$$\varepsilon(x) = \varepsilon_0 \exp\left(-x/X_0\right) \tag{2.5}$$

where $\varepsilon(x)$ is the energy of the particle; ε_0, is the initial energy, x the distance traveled by the particle. After quantum corrections radiation length is denoted by Equation 2.6 (ROSSI, 1952):

$$X_0 = \left[4N\frac{Z(Z+1)e^2}{\hbar c}\left(\frac{z^2e^2}{Mc^2}\right)\ln\left(\frac{233M}{Z^{1/3}m}\right)\right]^{-1} \tag{2.6}$$

where N is the number of atoms per cubic meter in the air, Z the average atomic number of the constituent atoms of the air, M the mass of the particle, m the mass of the electron ze the charge of the particles (for electrons, z and $M/m = 1$), $\hbar$ Planck's constant and c the speed of light. The term M/m appears because radiative loss implies the acceleration of incident particles, while collision loss implies the acceleration of an electron. Thus, for particles heavier than electrons, plasma shielding becomes negligible in the non-relativistic limit. For example, for electrons, the radiation length is 310 m (37 g cm^{-2}) in the air under STP conditions, 24 g cm^{-2} (8.9 cm) in aluminum and (5.8)g cm^{-2} (0.51 cm) in lead (JACKSON, 1999).

The minimum kinetic energy (or threshold) of the RE, ε_{th} is a parameter that depends on the applied ambient electric field and results from the solution of $eE = F_b(\varepsilon)$, where $F_b(\varepsilon)$ is the force of Bethe (Equation 2.7). Figure 2.4 shows the dependence of the minimum value of the friction force as a function of the electric field. The dashed vertical line shows the value for which the electric force (threshold electric field) equals the frictional force. The dashed asymptotic curve shows that as the electric field strength increases the minimum energy required to produce RE decreases.

For electrons moving through air (CRAMER et al., 2014) with kinetic energy greater than a few hundred eV, a large part of the energy loss is due to the ionization of the air and the other part to the rest of the atomic excitation. The energy losses by ionization or atomic excitation per unit length along the path of energetic particles are well described by Bethe's equation:

$$F_b(\varepsilon) \equiv -\frac{d\varepsilon}{dx} \tag{2.7}$$

2.3 Production of thermal runaway electrons

As shown in Equation 2.2, the RE flux due to the avalanche (F_{RREA}) is proportional to the flux of external energetic seed particles (F_0). In addition to the external particles, the lightning leaders or *streamers* can also provide seed electrons internally.

Figure 2.4 - Minimum energy to produce RE as a function of the electric field.

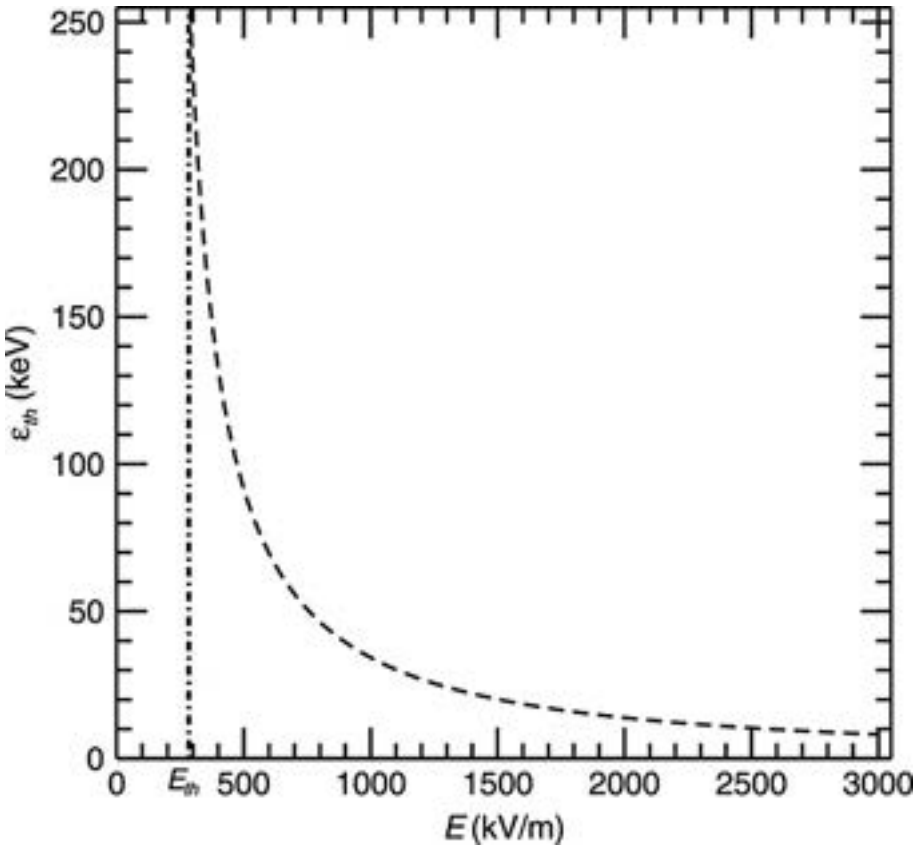

This value is determined by the Bethe friction force equation. The vertical dashed line represents the electric field value of the avalanche threshold, $E_{th} = 2,84 \times 10^5$ V m^{-1}.

SOURCE: Cramer et al. (2014).

Likewise, low-energy RE can be produced if the electric field slightly exceeds the critical electric field E_c through the mechanism of thermal RE production, *e.g.* at the extremes of the leaders the *streamers* (SIZYKH, 1993). This RE production mechanism, where neither an external source of external particles nor an intense electric field is needed, is called a thermal RE production mechanism.

The thermal RE mechanism produces the necessary seeds for the production of Wilson's RE, that is, for each seed electron generated by the thermal process, an energetic electron will be generated. Wilson's RE mechanism favors an increase in RE energy and the distance traveled by each RE seed produced by the thermal process, which represents an increase in x-ray emission. If the region where the electric field is intense intensifies, so that the REs traverse a greater potential, then Wilson's RE mechanism will produce RREAs, either by intensifying the electric field or by increasing the distance that the electrons travel. Thus, one RE is produced by each seed electron injected through the thermal process and the average energy of the RE is around 7 MeV (DWYER et al., 2012b).

Because lightning emits x-rays, a logical consequence is that these are produced by the RREA mechanism. However, x-ray energy and flux spectra constructed from observational data of induced lightning using rockets, show that the RREA mechanism is not consistent with the observations and suggest that the thermal RE mechanism is responsible for the radiation, supported by laboratory observations of emissions from sparks in air (MOORE et al., 2001; DWYER, 2004; DWYER, 2005).

2.4 Relativistic feedback mechanism

Dwyer (2003) performed numerical simulations of electrical discharges in the air, *e.g.* RE avalanches including positive feedback from gamma rays and positrons. In this way, it was found that large explosions of energetic radiation were produced in the air in the presence of an intense electric field, observing peaks of flux up to 10^6 times the values of the conventional models. These results could not be explained by taking into account only the RREA mechanism. Also, these explosions have important consequences for the electrification of storms and for the production of lightning.

In this mechanism, RE avalanches emit x-rays by Bremsstrahlung and can produce Compton backscatter or airborne pairs. Those photons produced in Compton backscatter that propagate to the beginning of the avalanche region produce other REs that produce a secondary avalanche. A common phenomenon is the escape of

positrons created by the production of pairs. The positrons rotate in the ambient electric field and escape in the opposite direction of the electrons. Because positrons are relativistic, they travel approximately on the order of a kilometer at sea level before annihilating. If these positrons propagate to the beginning of the avalanche region, they can produce additional RE through hard elastic scattering with atomic electrons in the air (*i.e.* Bhabha scattering), thus producing secondary avalanches (BABICH et al., 2007). These secondary avalanches emit more x-rays and in this way, the system feeds back (*feedback*). Thus, this positive feedback mechanism allows RE production to become self-sustaining, without needing an external source of energetic seed electrons. As a result of this positive feedback, the number of RE avalanches increases exponentially within a few microseconds (BABICH et al., 2005).

According to (DWYER et al., 2012b) there are main mechanisms called: x-ray feedback, photon feedback, and positron feedback. Feedback occurs when positrons and gamma rays, produced by RREA, propagate to a region where the electric field has its highest negative potential and once there produce more energetic seed electrons. These additional parameters are used in Monte Carlo simulations to calculate the necessary electric field thresholds for which the feedback mechanism becomes important.

Furthermore, the relativistic feedback mechanism is important because it can help explain the very large fluxes of energetic electrons and gamma rays and it also severely limits the electric field regimes in which alternative mechanisms can operate (DWYER, 2003; DWYER et al., 2012b). Finally, Figure 2.5 illustrates the difference between the Wilson RE mechanism, the RREA mechanism, and the relativistic feedback mechanism.

Figure 2.5 - Summary of the three mechanisms responsible for generating energetic electrons in the atmosphere.

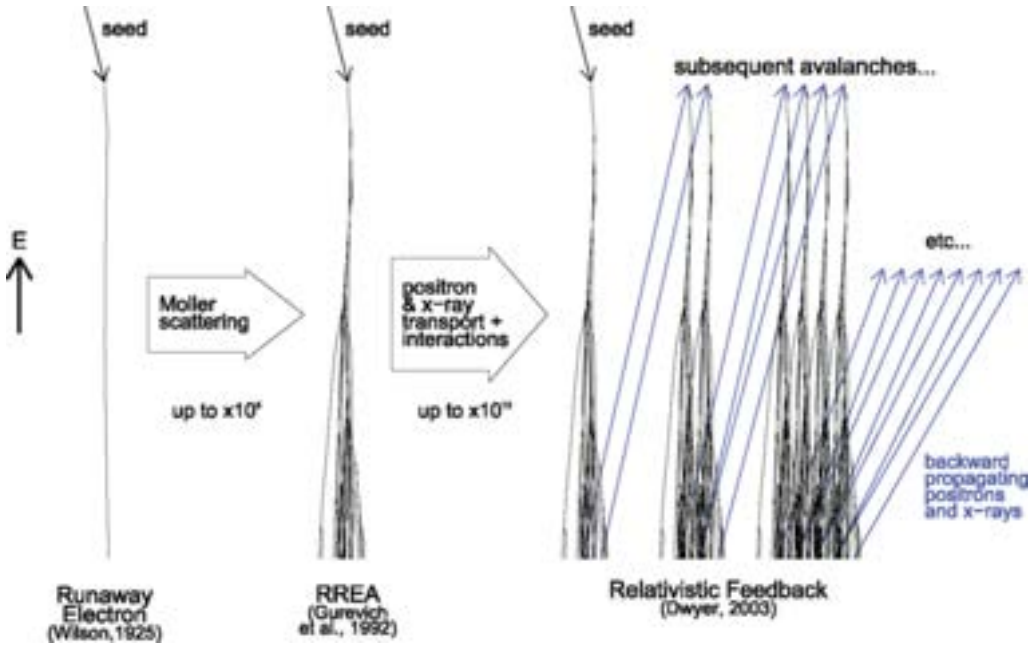

When adding Møller dispersion to the RE mechanism an RREA is produced and consequently the number of RE increases by a factor of 10^5 in relation to Wilson's RE mechanism. When the transport of positrons and x-rays is added, and the interactions with the RREA mechanism, a Relativistic Feedback Mechanism is produced, with an increase in the number of RE of up to 10^{13} in relation to the RREA mechanism. The backward propagating positrons and x-rays (blue arrows) and the resulting subsequent avalanches are shifted to the right because they often overlap with the initial avalanche. The energetic seed particle that becomes the first RE can be intensified by atmospheric cosmic rays, radioactive decay, or by the production of thermal RE during lightning

SOURCE: Dwyer et al. (2012b).

3 METHODOLOGY

To develop the work, the database recorded by the x-ray detector for two periods of observation in Brazil will be used.

Discriminate lightning-related x-rays from their natural background

This is necessary because a ground-level x-ray detector also records x-rays and gamma-rays due to cosmic background radiation and also emissions from any other radioactive sources in the vicinity. In this work, the following criteria will be considered.

- All the x-ray data that are related to the lightning activity will be analyzed, mainly the emissions that happened or will happen in a radius, less than 7 km, from where the instruments are installed.
- x-ray emissions that have several consecutive pulses, which coincide with the pulses of the electric field.
- x-ray emissions that correlate with the stepped process or continuous leader (dart leader) from the electric field signatures.
- The x-ray pulses occur a few hundred microseconds before the return discharge is recorded.

One of the objectives of this work is to know the energy resulting from the interaction of particles and to understand the physical processes involved that produce x-rays. For this, we model particles, mainly photons, considering the atmosphere as an ideal gas and at a certain altitude due to the impossibility of analytically studying the interaction of these particles with matter, and also to the abundance of different particles, processes and phenomena involved. The code is based on a tool that completely simulates particle development at depth and altitude in the atmosphere, which can be used directly for studies of energetic radiation from lightning and storms.

Monte Carlo

Monte Carlo simulation is a computational method that uses random sampling to simulate mathematical or physical experiments. It is a statistical technique used to model complex systems or processes that are difficult or impossible to solve analytically. Furthermore, it can be used to simulate a wide range of experiments, including

physical experiments such as the behavior of materials or the flow of fluids, as well as mathematical experiments such as the performance of financial models or the behavior of complex algorithms (LEHTINEN et al., 1999). In this work, Monte Carlo was used to simulating the motion and collisions of photons. There is a relationship between the cross-section and the probability of each interaction occurring. This is because the sum of all cross-sections is inversely proportional to the mean free path of a particle, which determines the distance it will travel between collisions. As the collision frequency is used instead of the mean free path, this distance can also be interpreted as the time between collisions, making the code time-oriented. The Runaway Electron Avalanche Model (REAM) which was developed by Joseph Dwyer, was used, which includes all relevant physics for the interaction and propagation of energetic photons and electrons in air (DWYER, 2003; DWYER, 2007; DWYER, 2012; CRAMER et al., 2014).

REAM

REAM is a physical model used to simulate the development of runaway electrons in electric fields. It is based on the Monte Carlo method, which is a statistical technique used to model complex systems by simulating the behavior of individual particles or objects. This model has been used to study a range of phenomena related to lightning and thunderstorms. (LEHTINEN et al., 1999; DWYER, 2003). The code takes into account all the important interactions involving runaway electrons, including ionization, atomic excitation, and Møllller scattering. A shielded-Coulomb potential is implemented in order to fully model elastic scattering, and it also includes the production of x-rays and gamma-rays (γ) from radiation energy loss (Bremsstrahlung) and the propagation of the photons, by including photoelectric absorption, Compton scattering, and electron-positron pair production. The code also considers Bhabha scattering, which is used to generate energetic seed electrons during positron propagation. In addition, photons emitted by newly produced electrons and positrons are included (DWYER, 2003; DWYER, 2007; CRAMER et al., 2014).

In this work, a part of the described REAM equations is shown in Chapter 2 *e.g.* the minimum energy is used to produce RE as a function of the electric field $E_{th} = 2,84 \times 10^5$ V m^{-1}, Equations 2.2, 2.3, length of avalanche described in function of the electric field Equation 2.4 and the distance an electron must travel given by Equation 2.5. The modeling of a physical phenomenon is continually being optimized, so when new processes or parameters are added to a given model, the results can differ drastically. The relativistic feedback mechanism can be considered one of the most

complete models because it involves the other two processes. In the approximation when $\gamma \ll 1$ the relativistic feedback mechanism becomes equivalent to the RREA mechanism. If the avalanche multiplication factor is further reduced, it becomes equivalent to Wilson's RE mechanism (DWYER et al., 2012a).

The Monte Carlo here is used to figure out the characteristics of the dart-leader that produced the x-rays, including attenuation, energy, direction, and propagation of radiation at different angles. In this study, 3D leader propagation reconstruction data was used. Data was obtained from high-speed and common cameras and has a time series of 125 points. This work focuses exclusively on photon propagation, including photoelectric absorption, Compton scattering, and electron-positron pairs. Thus, in this work, the REAM model was used, based on the Monte Carlo method and developed by Professor Joseph Dwyer, and has been, in this work, adapted for the first time to simulations only with photons instead of runaway electrons, as is originally done in the model. With this new adaptation of the model, data from observation were simulated and described in Chapter 6.

Furthermore, the purpose of modeling the data (3D data) using Monte Carlo will be to validate and compare theoretical and observational results. For this reason, the simulation was adapted only for photon interactions. A simulation involves tracking individual particles and their interactions, whereas the actual behavior is determined at random by the distributions provided by the physics describing the interactions. Repeating this approach multiple times yields the average behavior of a system.

The developed source code for the photons simulations is available in the Appendix D.

In order to determine the location and orientation of the leader's tip at the moment of the occurrence of x-ray emission related to lightning activity, the videos of the high-speed cameras and the data provided by lightning detection and monitoring network (BrasilDat and RINDAT) will be used. Can be seen in the results and analysis of the x-ray observations in Chapter 5.

4 INSTRUMENTATION

In this work, we used primarily the data recorded by the x-ray detector, the electric field, the videos provided by different cameras to corroborate with the x-ray recordings, as well as the data from specialized sensors to detect cloud-to-ground lightning provided by the RINDAT and BrasilDAT networks in real time. Furthermore, we were able to collect data with these instruments in two different periods and locations, first in São Paulo between December 2018 and March 2019, and the second at National Institute for Space Research (INPE) between November 2019 and March 2020.

4.1 Instrument calibration

Our x-ray sensor was calibrated in Brazil and in Florida before installation. The same procedure was repeated, but with different radioactive samples, using the amplified mode and the non-amplified mode. Thus obtaining a response from the x-ray sensor (calibrated at INPE) similar to the calibration response in Florida for radioactive Cs-137 sample as shown in Figure 4.1. The calibrations were carried out in places other INPE, such as the Institute for Advanced Studies (IEAv) and Technological Institute of Aeronautics (ITA).

X-Ray Detector

The x-ray detector is composed of three main parts: the photomultiplier tube (PMT), scintillator crystal NaI (TI) and the PMT base, which is composed of a voltage divider and provides the high voltage (HV) required by the PMT. Thus, the complete detector is contained in a 0.38 cm thick aluminum case to protect the instrument from moisture and light. The aluminum housing allows x-rays with energies up to about 30 keV to enter in all directions, while it acts as a Faraday cage to protect instruments from external static electric fields and RF noise. This instrument was designed to measure energetic radiation (x-rays and gamma-rays) from storm clouds and lightning (SALEH et al., 2009; DWYER, 2003). The x-ray instrument was operating through a cooperation between at INPE and the Department of Physics and Space Sciences at the Florida Institute of Technology. In addition, these instruments were used in the observations of x-rays produced by lightning and sparks in the laboratory, involving hundreds of measurements.

As can be seen in Figure 4.2, there are two PMT sensors that contain a 7.6 $\times$7.6 cm NAI scintillator crystal, one attenuated with lead and the other non-attenuated;

Figure 4.1 - Calibration results with different radioactive samples in Florida and INPE.

Florida

NaI / PMT S/N	PMT Base S/N	Supply voltage (V)	Cs-137 Calibration (mV)
60003-06386-I	09166600	992	37.2
60009-01460-I	09159359	794	46.6

INPE		NaI (Tl) / PMT		PMT Base	NaI (Tl) / PMT	PMT Base	
		60003-06386-I		09166600	60009-01460-I	09159359	
Supply Voltage (V)		**990**			**830**		
Noise	Pick (mV)	**+/- 6000**		***-115448**	**7500**	***-124642**	
	Grass (mV)				**2**	***-124420**	
Radioative Source		^{137}Cs (662 keV)	^{241}Am (59 keV)	Monazitic Sand	^{137}Cs (662 keV)	^{241}Am (59 keV)	Monazitic Sand
Anode	(mV)	**300**	**30**	**600**	**400**	**35**	**600**
	Archive	***-115950**	***-121428**	***-122157**	***-125443**	***-125952**	***-130306**
Pré - Amplifier	(mV)	**400**	**60**	**900**	**600**	**60**	**1000**
	Archive	***-120802**	***-121248**	***-122620**	***-125700**	***-125910**	***-130517**

PMT base (high voltage source and voltage divider); 12V battery, PMT anode output, directly connected to fiber optic transmitter (THz); and 0.32 cm thick aluminum case.

Data acquisition

In the first observation period in São Paulo, two different optical link devices were used for data acquisition: DG-VXR-250-850 and Fast Precision Analog Fiber Optic Link LTX-5515. We used this system (different optical fibers) because we didn't have another instrument similar to the DG-VXR-250-850. Also, the difference between these data acquisition instruments seems to be noise filtering.

The observations with the x-ray sensors in São Paulo were in the amplified mode because it would be one of the first observations carried out in Brazil and for this reason, we wanted to be sure to record x-rays produced by lightning.

In the second observation period, the instruments used in data acquisition at INPE,

Figure 4.2 - Rays-x instruments.

(a) (b)

Photo (a) shows the lead and lead-free x-ray sensors (PMTs) and the batteries that power the voltage divider. Photo (b) shows the aluminum housing and module that turns the measuring system on and off.

Figure 4.3 - Local where x-ray instruments were calibrated and installed in São Paulo. As can be seen from the photo.

two Fast Precision Analog Fiber Optic Link LTX-5515 were used, unlike São Paulo. At INPE, we observed in the non-amplified mode because we wanted to see the peculiarities of the x-ray, to address our objectives. In both observation periods, data from these instruments are stored with two sampling rates of 33 MS/s and 5 MS/s in two different instruments *PXIe-1082-National Instruments* and *ADLINK PXIe-3985*. In addition, the x-ray sensor is triggered (triggered) by the high-gain electric field sensor. Figure 4.4 shows the place where the x-ray and electric field instruments were installed (INPE).

Figure 4.4 - Local where the electric field and x-ray instruments were installed.

4.2 Additional data obtained by other instruments

Electric Field

Electric field sensor, it consists of two sensors: high gain and low gain, each of which needs an integrator and a fiber optic communication system (transmitter and receiver). The electric field measurement system consists of a parallel plate antenna coupled to an integrator and amplifier, a GPS receiver and 12 V power supply. This sensor provides lightning development data, the purpose of using it is to validate data records of the x-ray sensor. This geometry was chosen because it enables the physically modeling of the lightning and thus the estimation of the electric field produced by it lightning. Figure 4.5 shows the outside and inside of the instrument.

Figure 4.5 - Electric field sensor that shows the internal and external part of the sensor.

The internal part is composed of two integrators, two Tera-Hertz and the optical fiber that transmits the electric field signal.

Cameras

A total of 8 cameras of different models were used, the cameras are summarized in Table 4.1. They are from the Phantom model and of high recording speed. In addition, surveillance cameras and photographic cameras are used, all these cameras were installed in different places in São Paulo and INPE, and all cameras have time synchronization via GPS.

The main objective of using high-speed cameras in this work is to be able to follow the propagation direction of the leader and to infer the distance between the lightning and the x-ray sensor. Also, the observations by theses cameras can be used to compare with data recorded by other instruments.

Table 4.1 shows the configurations of each Phantom high-speed camera that is installed at INPE.

Table 4.1 - Characteristics of the different high-speed cameras, which can record the peculiarities of lightning, such as leader propagation.

Camera	Resolution	Sample rate(fps)	Duration of cinema(sec)	Bits
V711	512×256	49000	0,887	12
V9	960 × 720	2500	0,895	8
V9	768×576	3200	0,728	12
V9	1008 ×400	4000	0.891	8
V2012	384×320	120000	0.663	12

Lightning detection and location network

RINDAT

The National Integrated Network for the Detection of Atmospheric Discharges (RINDAT) is a network of specialized sensors deployed in Brazil, this network detection is in LF and VHF that allows detecting cloud-to-ground lightning. The system records the precise instant of occurrence, the location of the point of impact and physical characteristics, such as intensity and polarity. This is done through a set of remote sensors that detect electromagnetic radiation (EM) emitted by lightning in the range between 100 kHz to 300 kHz, analyzes the received signals through specific algorithms and eliminates those whose sources have not been atmospheric discharges (<http://www.rindat.com.br/>).

BrasilDAT

BrasilDAT is a network for detecting and monitoring atmospheric discharges that reach the ground or that occur inside the clouds. Like the RINDAT network, BrasilDAT also allows knowing the precise moment of occurrence, the location of the point of impact and the physical characteristics such as intensity and polarity in specific databases, thus allowing subsequent queries to the determined solutions in real-time and the data reprocessing. These data are obtained by means of sensors, which detect electromagnetic radiation in VLF, LF and VHF emitted by atmospheric discharges, in the range between 10Hz and 10 MHz and which allows a better performance in

relation to other detection networks (<http://www.inpe.br/webelat/homepage/>).

The main objective of using this network of instruments is that they provide us with information on the time of the event, the strength of the signal, location of the point of impact of that lightning, peak current of the return and polarity of the current. In this work, some magnitudes were used, such as the time of the event, the location of the impact point and the peak of the return discharge current, with the purpose of comparing with the registration data of other instruments, such as, for example, the electric field, x-rays and cameras.

5 X-RAY OBSERVATIONS IN BRAZIL

In order to characterize x-ray emissions produced by lightning strikes over a one-microsecond period and to understand the mechanisms of these events, different instruments were used. We consider two x-ray events registered in the P1P2 building, in São Paulo. The first event occurred on December 16th, 2018 (at 18:43:37 UT) and the second event was registered on January 24th 2019 (at 17:52:20 UT). In both cases, the x-ray production was generated by negative cloud-ground lightning. In order to analyze the events, it is necessary to compare the registered time for the different instruments installed in the P1P2 buildings (detection system), as well as for an electric field sensor installed in the University of São Paulo (USP-IAG, located 7 km away from the P1P2 building) and different cameras, a set of which was installed in Banfruty (fruit trade) 415 m from the detection system and a high-speed camera located 215 m from the detection system. Furthermore, the lightning detection network was used to discover the generated peak current and the distance for the lightning strike.

First event, registered in December 2018

At the start of the third trimester of 2018, the x-ray detection system was installed in building P2 next to the building P1, at a height of 50m, in São Paulo, Brazil, the same location of the electric field sensor. The x-ray detector was located at a distance of 215 m of the Phantom V711 high-speed camera and at a distance of 415 m of a standard camera. Figure 5.1 shows the change in the vertical electric field during a negative cloud-ground lighting strike.

An important objective of this work was achieved by registering the first x-ray event in Brazil. On December 16th, 2018 (18:43:37 UT), a negative cloud-ground lightning strike hit the ground near the x-ray detection system, generating seven return discharges, as seen in Figure 5.1. The first three discharges followed different paths (with the second and the third completely outside the cameras field of vision). The fourth discharge, after following the same initial path of the first discharge, went on a different path toward the ground and split during its propagation. The x-ray register was generated by the fifth return discharge during the propagation of the leader, generating a high current of -38 kA in comparison to the other return discharges. Figure 5.2 shows the fifth return discharge. The upper panel shows the x-ray emission registered by the attenuated detector (green curve) and non-attenuated (blue curve). The bottom panel shows the electric field sensor response (red curve). The time $t = 0$ corresponds to 18:43:37.718065 UTC.

Figure 5.1 - Electric field variation during a negative cloud-ground lightning strike on December 16th, 2018.

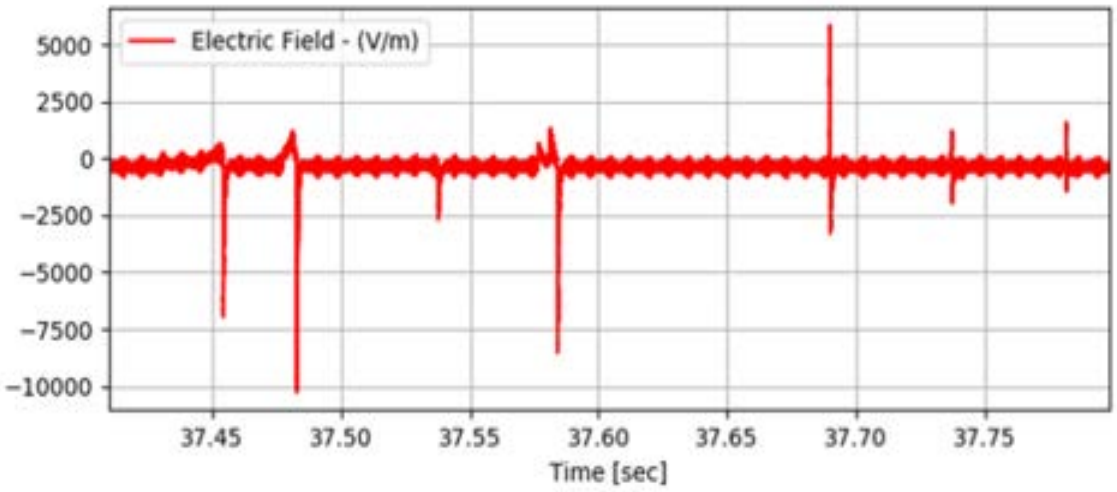

The BrasilDat and RINDAT networks detected this lightning strike, indicated an estimated peak for each return discharges. Considering the values described by the networks, as well as the image analysis, the continuous leader responsible for the x-ray emission hit the ground at a distance of 700 m from the x-ray detection system, as shown in our paper (SABA et al., 2019). Figure 5.3 shows the distribution of the lightning strikes registered of a period of 1 minute.

Second event registered in January 2019

On January 24th, 2019(17:52:20 UT), a negative cloud-to-ground lightning strike hit the ground near the P1P2 buildings. This event generated nine return strokes in a one-minute time interval, as can be seen in Figure 5.4. Furthermore, all return discharges followed the same path, as seen on Figures 5.5, 5.6, 5.7, and 5.8, registered by the V711 high-speed camera. In all images, the blue timestamp represents the return discharge occurrence time, in milliseconds.

The times of the return discharges shown in Table 5.1 were confirmed by the high-speed camera and the electric field sensors, as well as the lightning strike detection network. The second return discharge was not registered so, in order to estimate its

Figure 5.2 - X-ray emission associated to the fifth return discharge.

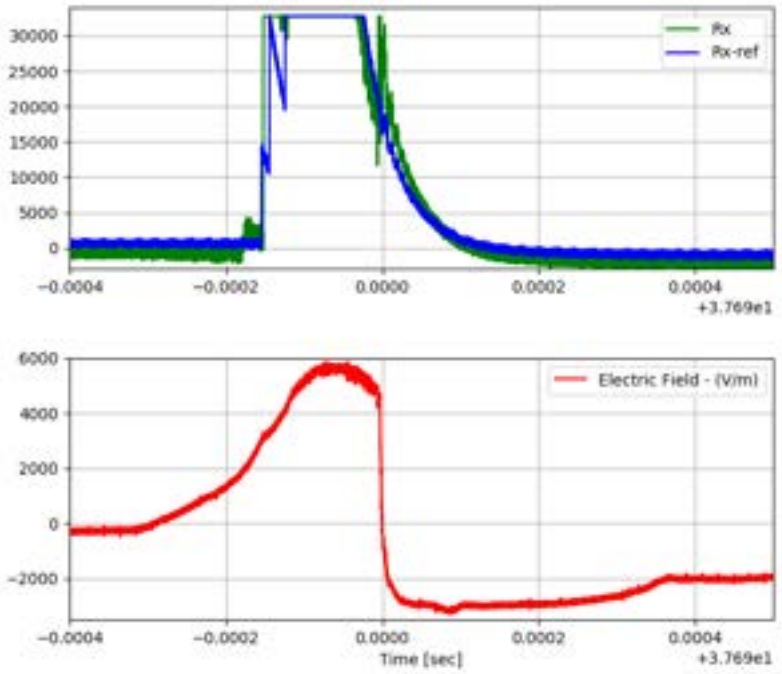

The time $t = 0$ corresponds to 18:43:37.718065 UTC. The x-ray emission is registered in the attenuated detector (green curve) and non-attenuated detector (blue curve). According to RINDAT and BrasilDat, the return discharge generated a current of -38 kA and occurred at a distance of 700 m from the P1P2 buildings.

generated current, we will consider the decrease in the return discharge, based on data from the electric field sensor installed at the University of Sâo Paulo (USP-IAG). The return discharges carry information about the lightning strike, such as current intensity, energy, momentum and peak irradiated potency (COORAY; LOBATO, 2020). Furthermore, the lightning magnetic field may modify the temperature of electrons in the high atmosphere, such as in the ionosphere, changing its electromagnetic propagation, as described in Inan et al. (2007). The energy transported by electromagnetic fields has a significant role in many of those interactions, which is why it is important to know the energy produced by lightning strikes.

In Figure 5.9, different colored curves show the development of the nine return discharges in different time periods, as registered by the electric field sensor installed at USP-IAG.

Figure 5.3 - Lightning up to 7 km around P2 on December 16, 2018.

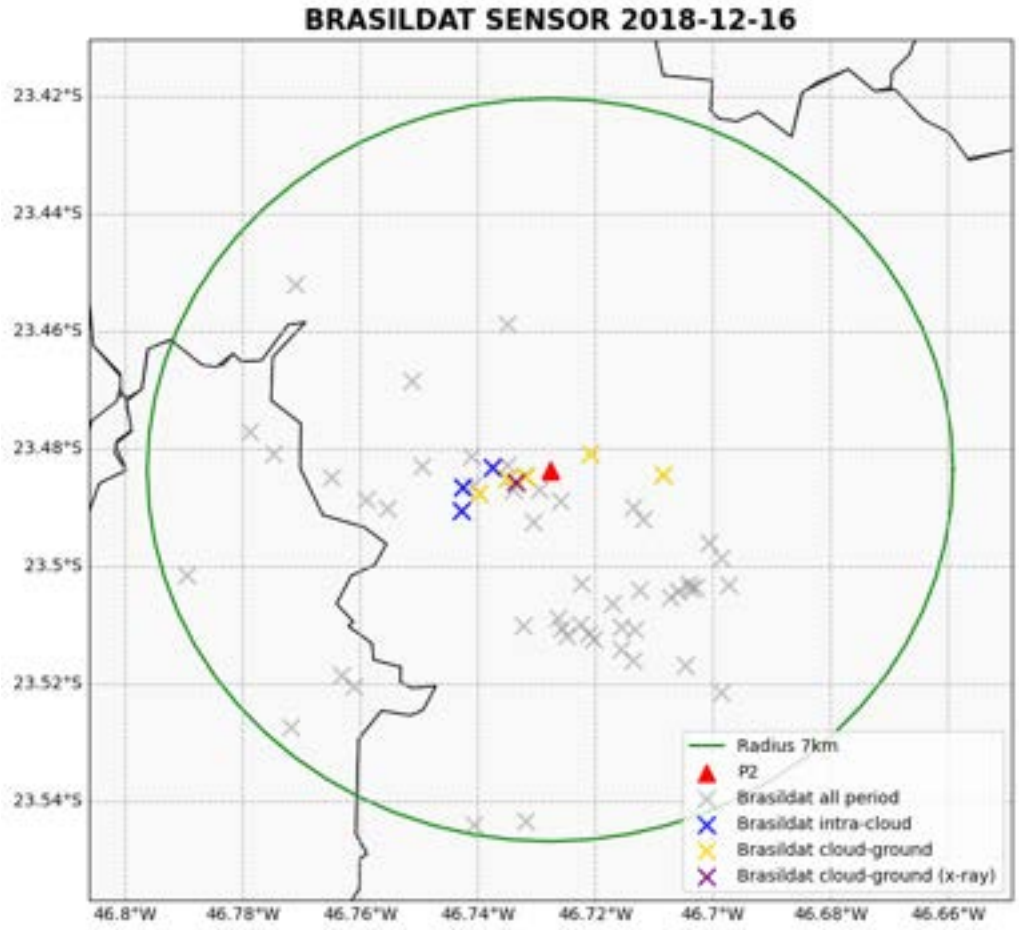

The triangular symbol represents the x-ray sensor location. The orange and blue X are lightning strike locations registered by BrasilDat which did not produce x-ray and the purple X is the lightning strike responsible for the x-ray emission.

These sensors were used because they provide a signal with low interference or saturation when compared to the lightning detection system (P1P2 buildings). Therefore, we can use this data to infer the current not registered by the lightning detection networks. Using this method, we may calculate the peak of current value for the non-registered cases. For instance, the second return discharge produced x-rays.

Figure 5.10 shows the linear correlation obtained from the values registered by the lightning network and the calculated variation in the return discharge, shown in Table 5.1.

Table 5.1 presents a summary of the nine return strokes, where the time values were

Figure 5.4 - Pulse variation in electric field data from the instruments installed in the P1P2 buildings.

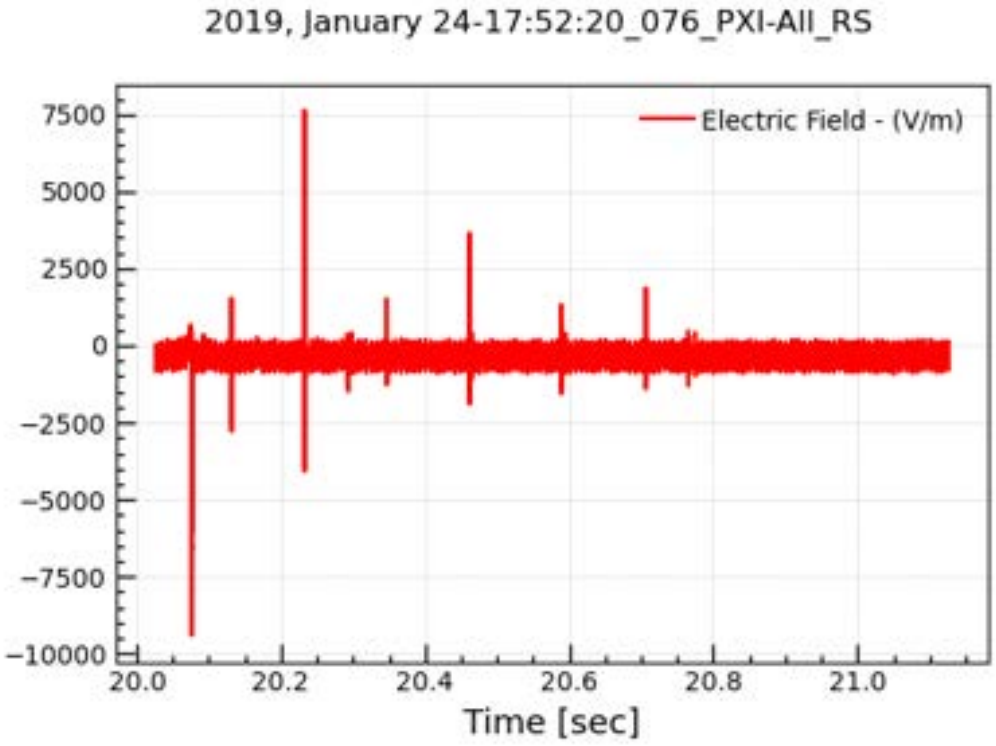

The signal is shown for a period of one minute on January 24th, 2019

Table 5.1 - Times verified by different instruments, as well as computed variations for each return discharge registered by the electric field sensors.

RS	t_{RS}(ms)	R_X		I_P(kA)	leader	ΔE_L	Efast-USP(ΔRS)
1	076018	-	138	-16	-	469	51
2	131464	yes		not registered		1025	41
3	232760	yes	171.0	-91	diffuse	4238	174
4	293628	-				303	20
5	346537	-				1006	43
6	461616	yes	167.8	-46	diffuse	2188	99
7	588926	-	70	-12	faint	908	33
8	706061	-				1240	48
9	764999	-		-5		449	18

verified using information from high-speed cameras (videos), electric field data with different temporal resolutions, as well as current sensors, and lightning detection

Figure 5.5 - The photos show the path followed before and after the first return stroke of 076018 ms.

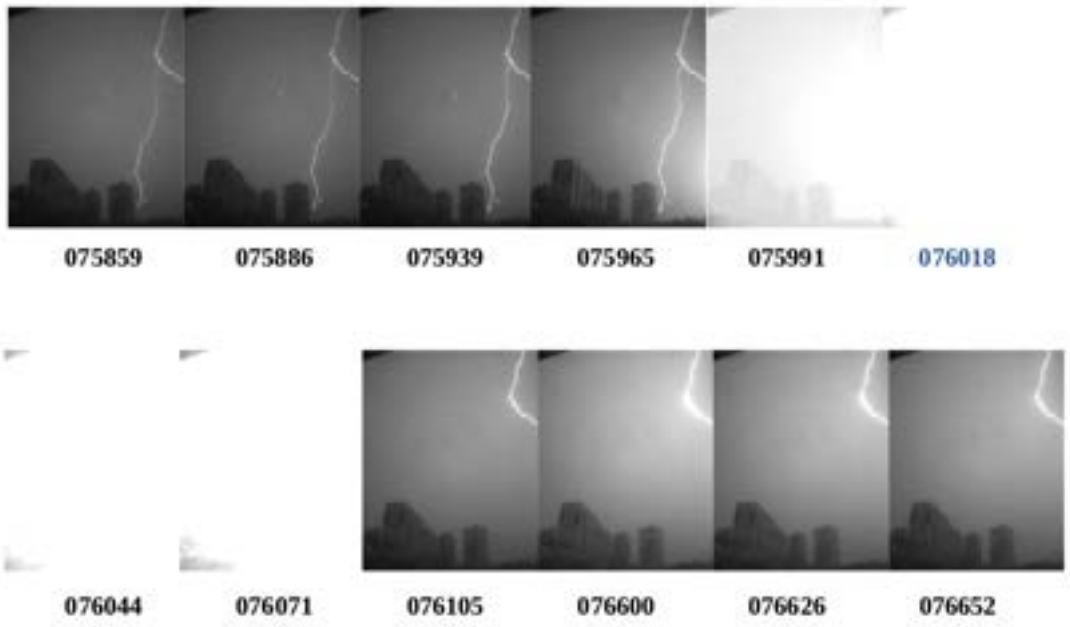

networks. However, for some of the return discharges, we do not have information on the lightning networks, most likely due to their detection efficiency. Leader propagation variance and return discharge variance values were calculated using 5 MS/s data from instruments in building P1P2 and at USP.

Furthermore, the ellipse values (this parameter defines the uncertainty of lightning location.) and I_p (peak current) are values registered by the detection networks. As mentioned previously, on January 24th, 2019 (at 17:52:20 UT), a cloud-to-ground lightning negative strike hit the ground near the x-ray detection system, generating nine return discharges. In this event, all return discharges followed the same path, and three generated x-ray emissions. The x-ray registry happened during the second, third, and sixth return discharge in different time periods, during the leader propagation. Two of these return strokes generated currents of -91 and -46 kA (the third and sixth ones return discharge) as shown in Table 5.1, occurring at distances of 3 km and 158 m from the x-ray detection system. For the second return discharge, the current was calculated at around -20 kA using the linear correlation shown in Figure 5.10. The ΔE_L and ΔRS values in the table were calculated from the electric field

Figure 5.6 - The photos show the path followed before and after the second return stroke of 131464 ms.

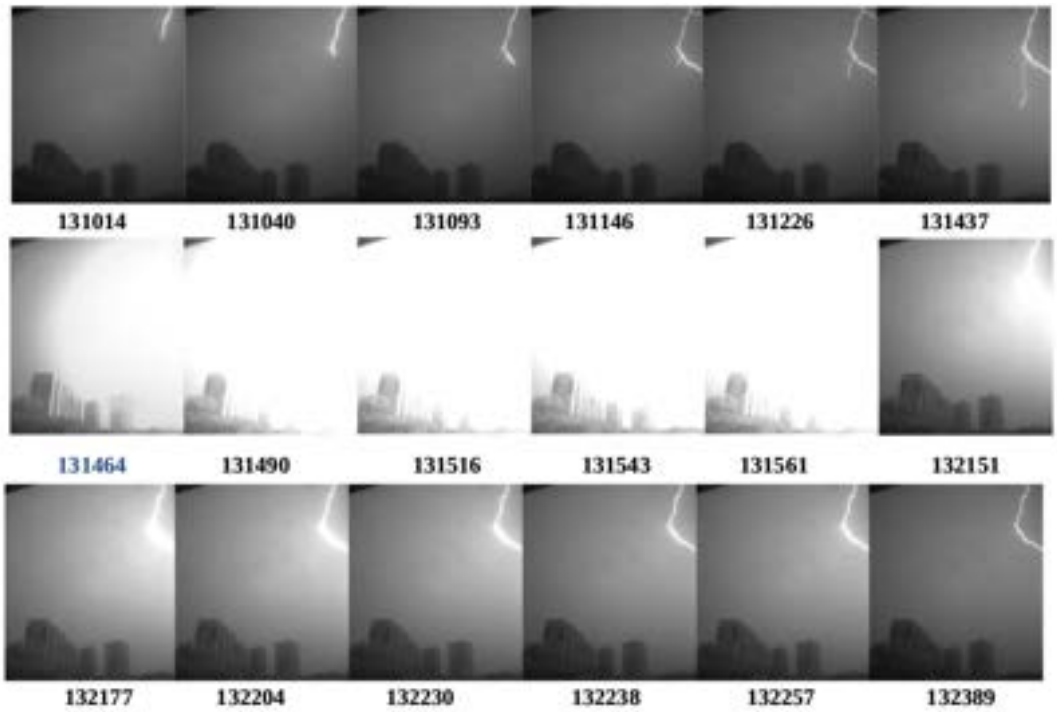

response. ΔE_L is the leader propagation variation for the 9 return strikes calculated from the electric field sensor located at P1P2 and ΔRS is the return stroke variation calculated from the electric field sensor located at IAG-USP.

As seen in Figures 5.11, 5.13 and 5.14, the electric field variation is divided in two phases: the first phase corresponds to the field generated by the leader propagation (slow increase) and the second phase is associated to the radiation electric field, which is proportional to peak current (signal decrease) generated by the return discharge. As the descending leader approaches the ascending leader, the electric field intensifies and the moment of the encounter (maximum peak) occurs the return discharge, where the electric field decreases until it reaches opposed polarity (negative). The observed x-ray emission in all three cases occurred during the leader dart step phase, just before the moment where the return discharge occurs. The timing of the x-ray emission followed the timing of the electric field variation, meaning the x-ray was emitted at the same time as the electrostatic field changes. However, one must remember that not all leaders produce detectable x-ray emissions, as shown by Mallick et al. (2012), Dwyer and Uman (2014).

Figure 5.7 - The photos show the path followed before and after the third return stroke of 232760 ms.

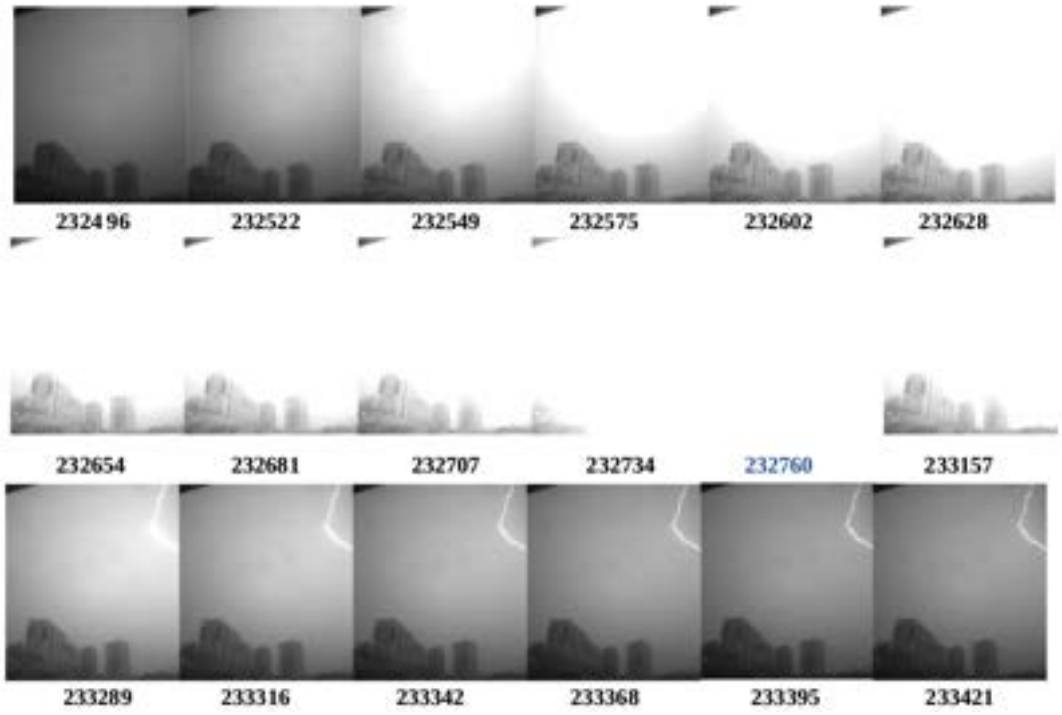

In the upper panel in Figure 5.11, we see the x-ray emission registered by the attenuated x-ray sensor (green curve) and non-attenuated (blue curve). In the lower panel, we see the electric field sensor response (red curve). The time t=0 corresponds to 17:52:20.1315 UTC. The lightning strike detection networks did not register this event. However, the peak current value is $\sim$ 20 kA, and it probably occurred at a distance of 150 m. According to image 5.12, which illustrates the development of the 2nd return stroke close to the observation building.

In the upper panel in Figure 5.13, we see the x-ray emission registered by the attenuated x-ray sensor (green curve) and non-attenuated (blue curve). In the lower panel, we may see the electric field sensor response (red curve). The time t=0 corresponds to 17:52:20.232760 UTC. This event was registered by the lightning detection network RINDAT with a current value of -91 kA, occurring 3 km away from the lightning detection system.

Figure 5.14 shows the x-ray emission registered by the attenuated x-ray sensor (green curve) and non-attenuated (blue curve). The time t=0 corresponds to

Figure 5.8 - The photos show the path followed before and after the sixth return stroke of 461610 ms.

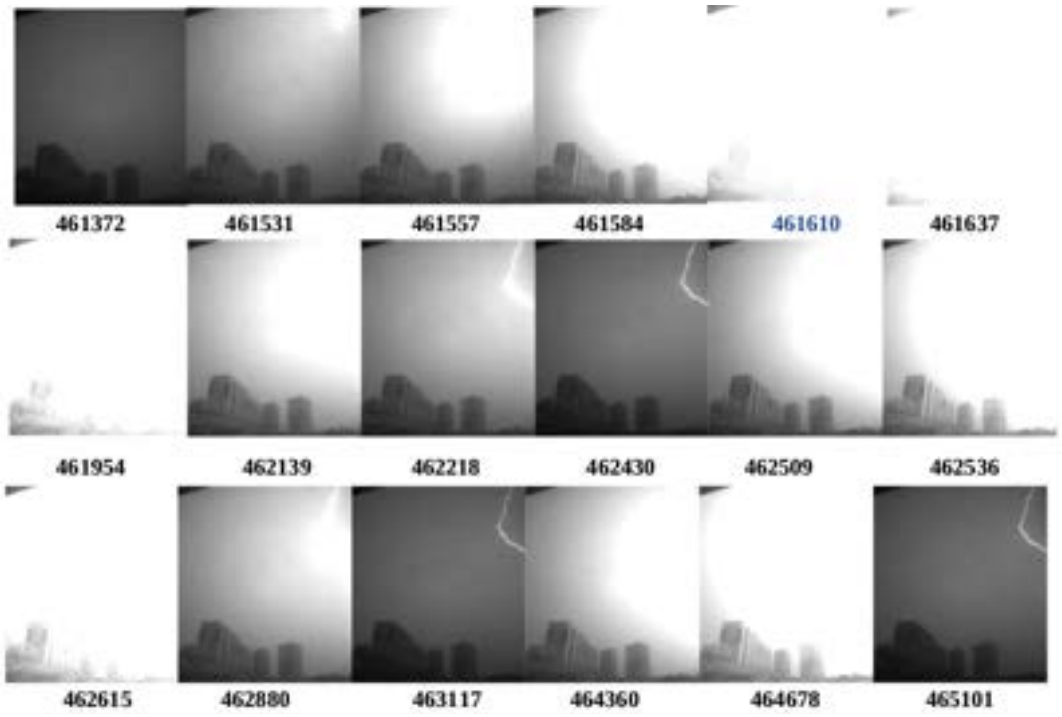

17:52:20.461621 UTC. This event was registered by the lightning detection network (RINDAT) with a current value of -91 kA, occurring 150 m away from the lightning detection system.

The differences observed in the signals from the three events (with and without lead) may be caused by the use of two different equipment during the data acquisition, as it was explained in Chapter 4. The sensors response shown in the amplified mode are similar to the first responses obtained by (DWYER et al., 2003) but, in this case, with triggered lightning strikes.

The graphs shown for the first and the second x-ray event were created using data with a temporal resolution of 33 MS/s, in order to show peculiarities in the x-ray response.

In order to show the location of the lightning strikes responsible for the x-ray emissions, we use Figures 5.15 and 5.3. The geographic coordinates (latitude and longitude) were used to calculate the distance, position, and azimuthal angle for the

Figure 5.9 - Different colored curves show the variations in the return discharges measured by the electric field sensor produced by a negative cloud-ground "flash" for the nine return discharges in different time periods.

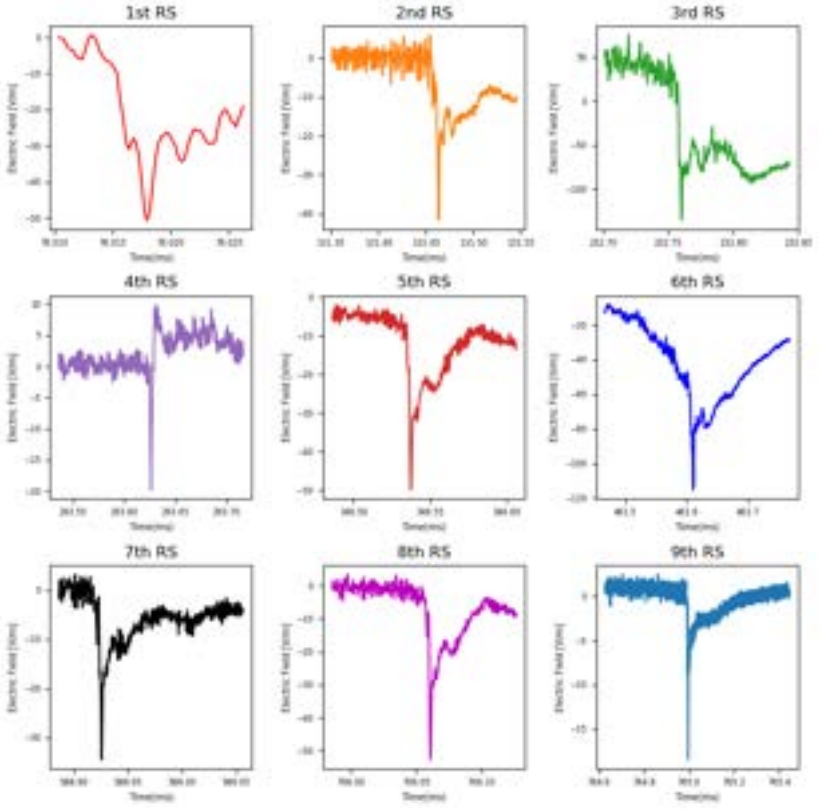

lightning strike with respect to the detection system, based on data from the Brazilian Lightning Detection Network. For this, the Haversine equation was used.

$$hav\left(\frac{d}{R}\right) = hav(lat2 - lat1) + cos(lat1)cos(lat2)hav(lng2 - lng1) \tag{5.1}$$

Where d is the distance between the two points (along a sphere), R is the sphere or Earth radius, $lng1$ and $lng2$ are the longitude of points 1 and 2, $lat1$ and $lat2$ are the latitudes of points 1 and 2, hav is a function defined by the Equation 5.2.

Figure 5.10 - Correlation between the values recorded by the lightning networks and the variation calculated from the electric field sensor (USP) data.

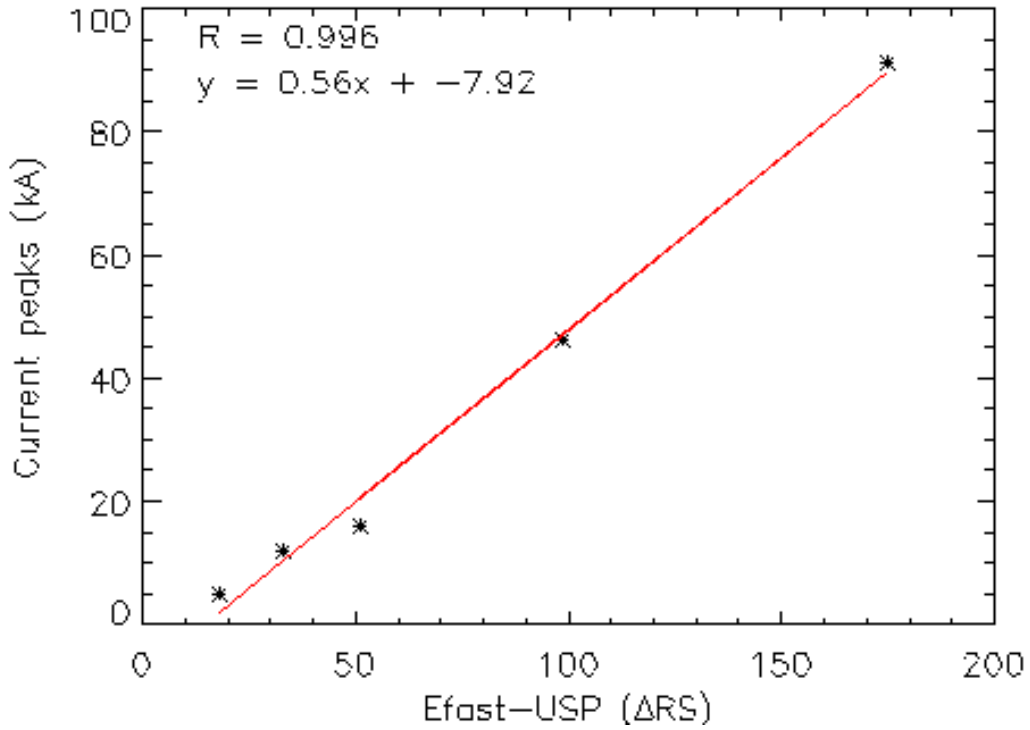

This method is used to measure the distance between two points in a sphere using latitude and longitude.

$$hav(\theta) \;=\; sin^2\left(\frac{\theta}{2}\right) \;=\; \frac{1 - cos(\theta)}{2} \tag{5.2}$$

In the first Equation 5.1, dR is considered an angle in radians. Therefore, we may rewrite the Haversine formula in a more familiar notation, as shown in Equation5.3.

$$d = 2r\, arsin\, \left(\sqrt{hav(lat2 - lat1) + \; cos(lat1)cos(lat2)hav(lng2 - lng1)}\right)$$

Figure 5.11 - X-ray emission associated to the second return discharge.

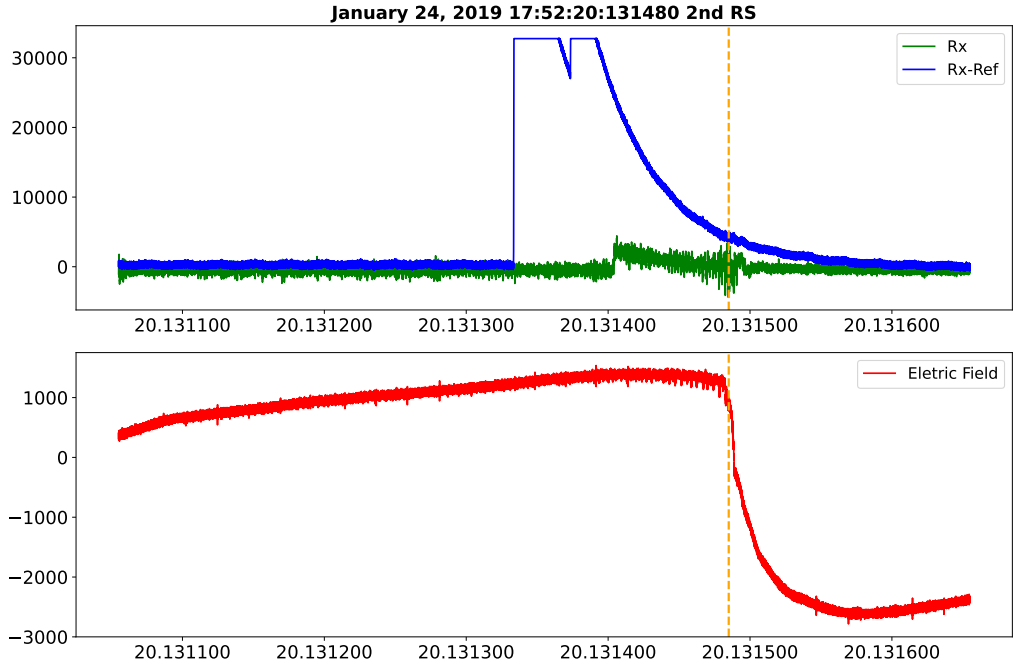

The blue (attenuated) and green (non-attenuated) curves are the x-ray sensor signals and the red curve is the electric field signal.

$$= 2r\, arsin\left(\sqrt{sin^2\left(\frac{lat2 - lat1}{2}\right) + cos(lat1)cos(lat2)\, sin^2\left(\frac{lng2 - lng1}{2}\right)}\right) \tag{5.3}$$

Figure 5.15 shows the location of the lightning strike registered by the two detection networks, as shown in Table 5.2. The triangular symbol shows the x-ray sensor location. The $\times$ markers in the colors orange and blue are the locations where the other return discharge occurred, as registered by the BrasilDat network, and did not produce high-energy radiation. The purple x markers were registered only by the RINDAT network and produced high-energy radiation (x-rays).

Table 5.2 shows the values for the five return discharges registered by the Brazilian lightning strike detection network BrasilDat and by the RINDAT such as the time in nanoseconds, peak current, azimuth angle and distance for a lightning strike occurring during a period of one minute and within 7 km of the x-ray sensor.

Figure 5.12 - Development of the second return stroke near the observation building.

Figure 5.13 - X-ray emission associated to the third return discharge.

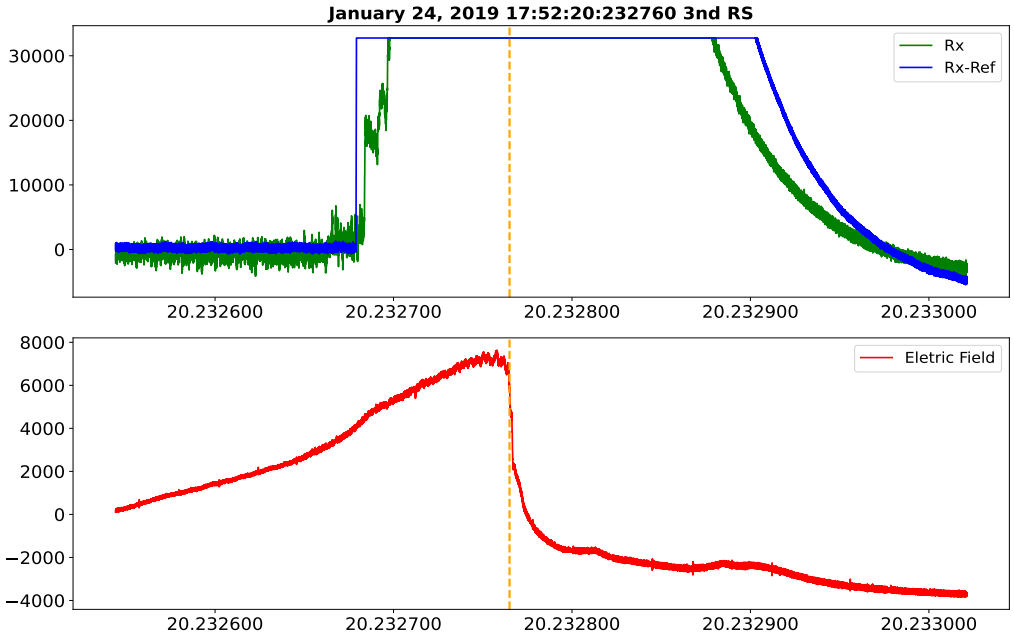

The blue (attenuated) and green (non-attenuated) curves are the x-ray sensor signals and the red curve is the electric field signal.

Figure 5.14 - X-ray emission associated to the sixth return discharge.

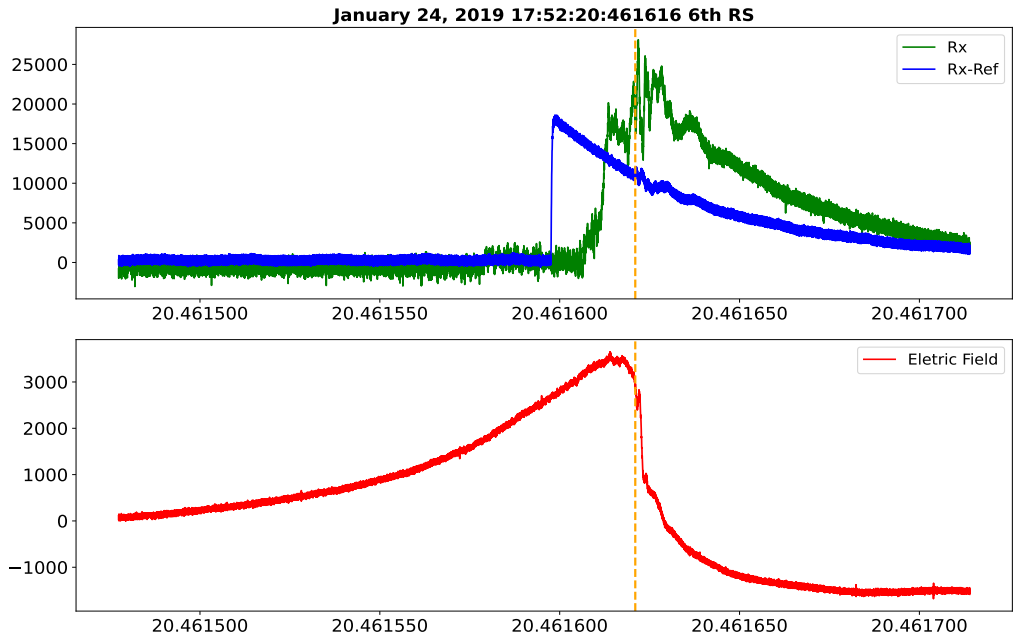

The blue (attenuated) and green (non-attenuated) curves are the x-ray sensor signals and the red curve is the electric field signal.

Table 5.2 - Five return discharges of the nine generated by a negative cloud-ground lightning strike, registered at about 7 km by the BrasilDat and RINDAT networks.

RS	Time (nanosec)	I_P (kA)	Semi axis(km)	Azimuth ellipse	Distance (km)	Azimuth angular	Geometry (Lat,Long.)
1	076001176	-16	0.5	138	1.24	342.18	(-46.73140 -23.47300)
2	-	-	-	-	-	-	-
3	232760854	-91	0.4	171	3.43	97.02	(-46.69430 -23.48740)
4	-	-	-	-	-	-	-
5	-	-	-	-	-	-	-
6	461616952	-46	0.6	167	0.15	259.14	(-46.72920 -23.48390)
7	588917376	-12	0.5	82	1.15	346.50	(-46.73030 -23.47360)
8	-	-	-	-	-	-	-
9	764995392	-5	0.3	97	1.18	306.51	(-46.73700 -23.47730)

X-ray emissions produced by natural lightning in Brazil were successfully measured during two observation periods at a distance of up to about 3.5 kilometers around the x-ray sensor, according to information obtained from the lightning detection and monitoring network (BrasilDat and RINDAT). According to observations made in

Figure 5.15 - Lightning up to 7 km around P2 on January 24, 2019.

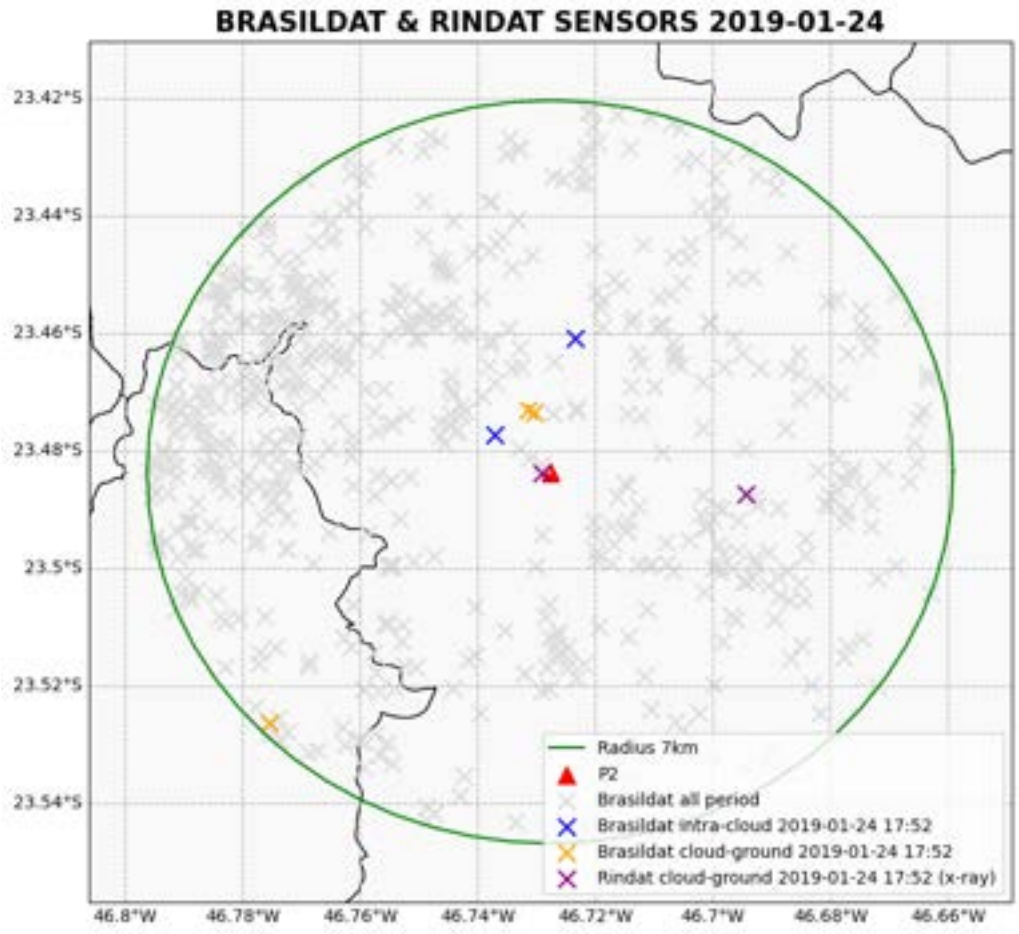

The triangular symbol shows the x-ray sensor location. The × markers in the colors orange and blue are the locations where the other return discharge occurred as registered by the BrasilDat network and did not produce high-energy radiation. The purple X markers were registered only by the RINDAT network and produced high-energy radiation (x-rays).

São Paulo, the x-ray emissions were produced by dart-stepped leaders associated with natural negative cloud-to-ground lightning (GAMEROTA et al., 2014). In the two observed events, the (x-ray) emissions begin approximately 100 to 330 μs before the return stroke, which is consistent with observations at (DWYER et al., 2003; HETTIARACHCHI et al., 2018).

Based on the simultaneous recording of high-speed video images, x-rays, and electric field measurements. We assumed that the x-rays were recorded only when the leader tip was located in a certain portion of the lightning channel. Detection of the x-rays occurs when the leader is likely oriented towards the detector, supporting the

hypothesis of a flowing beam of x-rays shown in Montanyà et al. (2014), presented in details of the first event in our paper and shown in Appendix C ((SABA et al., 2019)). In addition, for this first event, the 3D leader propagation reconstruction described in was performed (MEDEIROS, 2020). These data were used to perform the modeling, as explained in Chapter 6.

6 LEADER CHANNEL PROPAGATION MODELING

6.1 Motivation 1

In the description of our first observation, we mentioned that the natural lightning that produces x-rays has to be near or pointing to the x-ray sensor. We reached this conclusion through our analysis and optical observation (Saba et al. (2019)). As of now, there is no evidence that the lightning producing the x-rays must be pointed exactly toward the x-ray sensor to be detected.

Thus, to consolidate our theory that the lightning that produces x-rays has to be oriented towards the detector, we used the 3D reconstruction data to make the simulations. In this way try to explain how the x-ray emissions are produced. For this, we will only take into account some of the physical processes in the propagation of the dart-stepped leaders, in order to validate our analysis of the first observation. In this work, the REAM model will be used to simulate the propagation development of the leader using the Monte Carlo simulation method. It will be adapted to simulate only photons propagation. The purpose of modeling is to validate whether our hypothesis makes sense and to understand how x-rays are emitted.

6.2 Interactions of photons with matter

Photons interact differently in the matter than charged particles because photons have no electrical charge. As opposed to charged particles, photons do not experience continuous energy loss as they travel through matter. Instead, photons undergo interactions in which they transfer their energy to charged particles, typically electrons. These charged particles then give up their energy through secondary interactions, which are often related to ionization.

The lack of electrical charge in photons means that they do not experience electromagnetic interactions with matter in the same way that charged particles do. Instead, photons interact with matter through a variety of mechanisms, such as the photoelectric effect, Compton scattering, and pair production. These interactions involve the transfer of energy from the photon to the matter with which it interacts.

When a photon interacts with an atom, it can transfer its energy to one of the atom's electrons, causing it to be ionized. This electron may then go on to cause additional ionization events through further interactions with other atoms or molecules. In this way, the energy of the photon is transferred to the surrounding matter.

There are many possible photon interactions, but we will focus on the three main interactions mentioned above. Monte Carlo simulations are a powerful tool that can account for all interactions between photons and energetic electrons and positrons, including Rayleigh scattering, to provide accurate predictions of photon behavior in matter (CRAMER et al., 2014).

The Figure 6.1 illustrates the total cross-sections of these three processes in nitrogen as a function of photon energy. Rayleigh scattering, which changes only the direction of the photon, plays a minor role in the energies considered.

Figure 6.1 - The photon interaction cross-sections for energies ranging from keV to GeV.

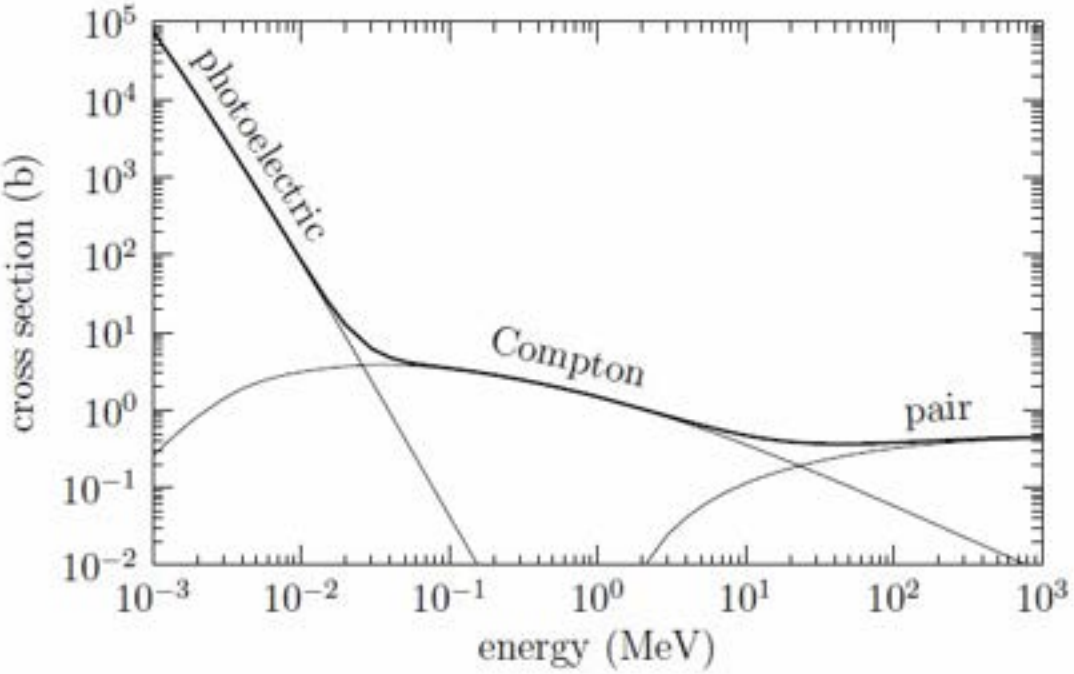

There are two types of curves: bold and solid. The bold curve represents the total cross-section, and solid curves represent each process

SOURCE: Cramer et al. (2014).

Photoelectric effect

The photoelectric effect is caused by an interaction between an atomic electron and a photon. During this interaction, the photon disappears and one of the atomic

electrons is ejected as a free electron (called the photo-electron), resulting in the ionization of the atom since the photons (x-rays) are completely absorbed and all their energy is transferred to the electrons.

The photoelectric process is the dominant interaction mode for gamma rays and x-rays of relatively low energy (KNOLL, 2010).

Compton effect

Compton scattering occurs when an incoming photon is deflected by an angle Θ with respect to its original direction (Figure 6.2). Photons transfer a portion of their energy to the electrons (supposed to be initially at rest), which are then called recoiled electrons.

Figure 6.2 - A schematic of Compton scattering, illustrating an input photon scattered by an electron at rest.

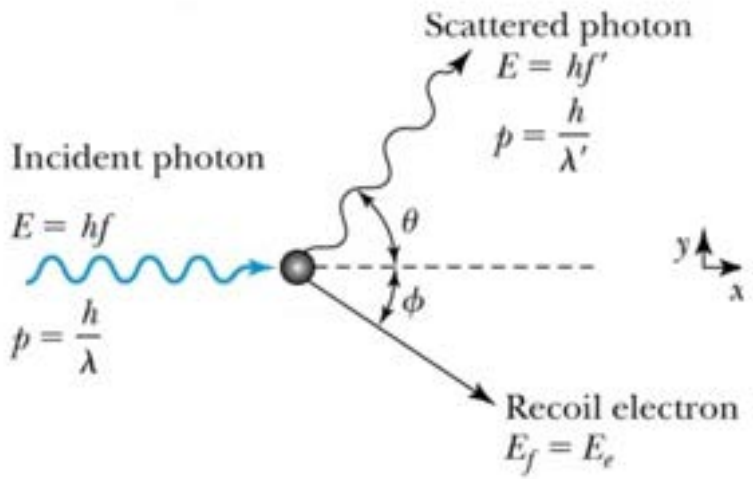

Pair Productions

Pair production occurs when a photon interacts with a nucleus. As a result of this interaction, an incident photon (x-ray) is completely absorbed and a positron (e^+) and electron (e^-) appear (KNOLL, 2010). However, this is only possible at energies above 1.02 MeV. The nucleus does not undergo any change as a result of this interaction, but its presence is necessary for pair production.

Rayleigh Scattering

A feature of Rayleigh scattering is that it does not excite or ionize the atom, and the scattered photons (x-ray) have energy identical to the incident photon (x-ray), but low photon energies (typically below a few hundred keV) have the highest scattering probability (KNOLL, 2010).

In summary, understanding photon interactions are fundamental in several fields of physics, such as High-energy Atmospheric Physics, Particle Physics, and Medical physics.

6.3 Photon attenuation

A photon with a given energy in a uniform medium proceeds with a certain probability (per unit distance) of having an interaction or collision. This probability is called the linear attenuation coefficient of the medium, given by $\lambda = 1/\mu$, for photons with that certain/given energy (KNOLL, 2010).

Therefore, the coefficient attenuation has dimension on inverse length (cm^{-1}). The exponential attenuation function describes the behavior of uncollided photons (Equation 6.1).

$$N = N_0 \, e^{-Z/\lambda} \tag{6.1}$$

where N is the energy of photons transmitted across some distance, N_0 is the energy initial of photons, λ mean path free, and Z is the absorption coefficient (μ the linear attenuation coefficient).

There are two quantities used to describe the probabilities of these interactions: linear attenuation coefficient (μ) and mass attenuation coefficient (μ/ρ). The linear

attenuation coefficient is the probability of an interaction per linear distance traveled by the photon. It corresponds to the sum of the probabilities of the photoelectric effect (τ), the Compton scattering (σ), and the pair production (k) (Equation 6.2).

$$\mu\,(m^{-1}) = \tau + \sigma + k \tag{6.2}$$

The attenuation coefficient determines how photons pass through matter. Unlike charged particles, photons have no associated range that limits their distance traveled. According to Equation 6.1, there is always a finite probability that some incident photons will get through a shield of any thickness without having an interaction. Physically, μ is the probability of interaction per unit distance (KNOLL, 2010).

The data used in the 3D reconstruction (time series of 125 points) provide the leader propagation, average speed (1.6x10^6 m/s), and only the start time that was used from the high-speed camera. We calculate the distance propagation from the average speed and, then, thus obtain the propagation time of the leader in each temporal series of the data.

The Monte Carlo simulation is used to propagate 100000 photons in the 3D reconstruction data. Therefore, it is useful to study the properties of the photons that reach each leader propagation point, in this study a set of 125 points. The leader propagation direction was downward.

In this analysis, we want to know the photon propagation behavior at different angles in each time series and to prove if the reason why x-rays turned on and then turned off is that the beaming is totally isotropic. If this hypothesis doesn't make sense, then we expect that: It does not matter if the leader is pointing at the detection sensor, that is, how close or far they are, what matters is that the photons propagate in all directions and all the on and off is only due to distance, so the influences would be the distance or the effect of distance.

The simulation was repeated 10 times in order to statistically analyze to the behavior of the data since we are considering a random simulation. Figure 6.2 shows the results of the simulation done in Monte Carlo using the number of photons and the four physical processes mentioned above.

The results presented here were made using the REAM model, based on the Monte

Figure 6.3 - The results of the simulation done in Monte Carlo using the amount of photons and the four physical processes mentioned.

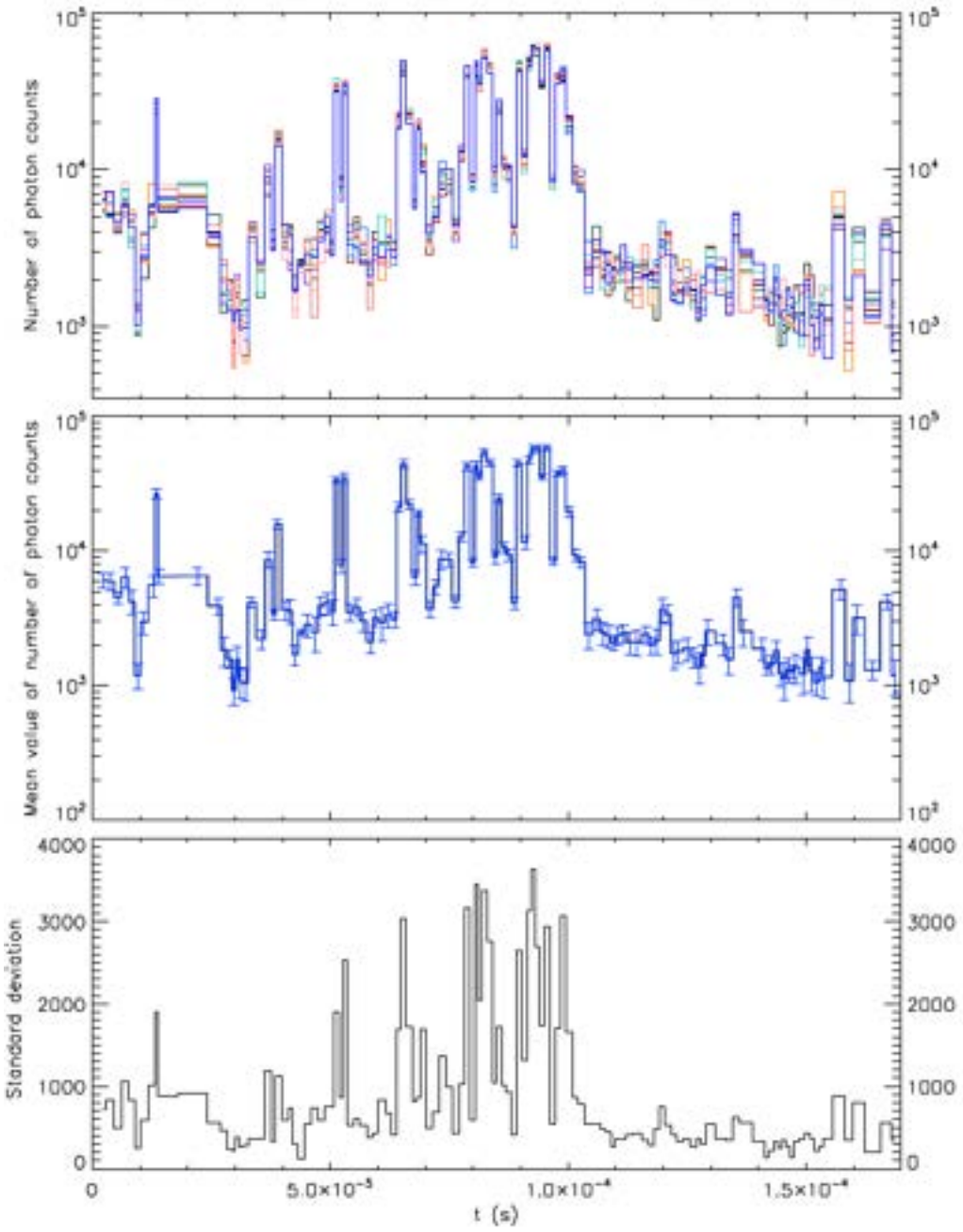

The curves of different colors are the 10 times simulations, the blue solid curve is the mean value of the number of photons counts of the 10 simulations made and the black color curve is the standard deviation.

Carlo method and developed by Professor Joseph Dwyer, and were, in this work, adapted for the first time to simulations with only photons instead of runaway electrons, as is originally done in the model. In Figure 6.3 you can see curves of different colors, each color represents a simulation, the solid blue curve is the average value of the number of simulated photons (simulations performed 10 times) and the black curve is the standard deviation. and as we can see the variation in the standard deviation is small compared to the simulated data.

One example of the theoretical model of photon propagation using REAM is shown in Figure 6.4. In this model, a source height from 0 to 1000 m was used to propagate the photons through the atmosphere to know the variation of energy (photon attenuation) generated by the three physical processes involved, described in Equation 6.2. The results of these simulations show that there is a difference in energy loss that will depend on the E-folding input indicated in Figure 6.4. The variation of energy depends inversely on the altitude of the photons. The higher the altitudes the energy decreases, according to the Equation 6.1 and Figure to 6.4. Furthermore, Figure 6.4 shows that the model is a good fit for the data. In this figure, the black diamonds are the data and the blue and red diamonds are the exponential fit.

The theoretical result shows that there is attenuation of the particles (photons in this case), which indicates that the modeled data suffers the loss of energy. The data were modeled using 100 keV E-folding, so the energy range is likely to be approximately between 10^3 to 10^7 keV as shown in Figure 6.4. Since we already know the energy range, we can assume from Figure 6.1 that the physical processes involved in leader propagation are possibly due to Compton scattering and Pair creation.

As we can see in Figure 6.5, the model response shows variations in the average number of photon counts. These variations occur between a time period of 0 to 80 micro-seconds and correspond to the portion marked with dashed red lines in the image on the right side. When modeling the leader propagation data we also consider the perfect atmosphere (ideal gas).

Figures 6.6 and 6.7 show the variation of energy as a function of different angles. In these theoretical tests, a fixed height of 100 m (z = 100 m) and a theta angle ranging from 0^o to 315^o were considered. This was made with the objective of testing if the angle of incidence influences the propagation of the photons. What we also want to see is if the photons have a preferred angle for their propagation. In addition, wanted to know at which angle the energy loss is greater and to rule out whether the angle influences the propagation of photons. From these theoretical tests, we

Figure 6.4 - Theoretical model of photon propagation.

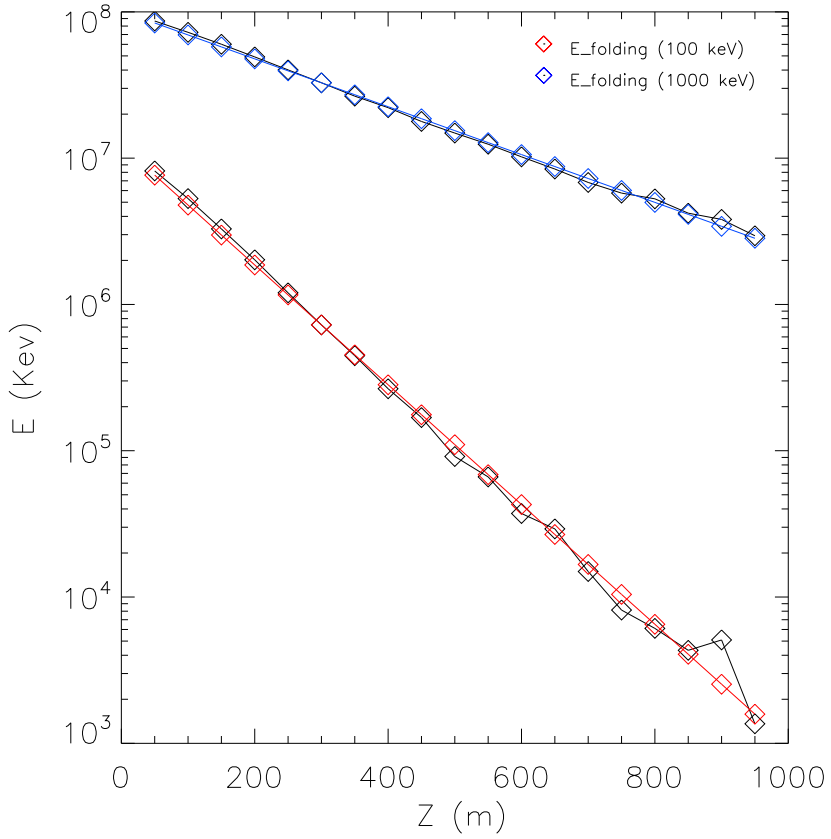

The black diamonds are the theoretical data and the blue and red diamonds are the exponential fit.

observed that for angles from 0^o to 90^o including 270^o and 315^o there is an energy variation of approximately 10^5 to 10^7 keV, that is, two orders of magnitude and the aperture for each angle is also different.

Figures 6.8 and 6.9 show height as a function of energy. Photon propagation was modeled to determine the variation of energy at a given height, in this case, Z, which varies between 0 to 1000 m, taking into account different propagation angles.

After modeling the propagation of the leader, we make the comparison of the modeled (optical) and observational data (Figure 6.10) to see the behavior and try to explain the variations found. What we want to know is whether these variations correspond to the variations of the x-ray pulse and in which part of the x-ray signal it is found. For this, the initial time that was considered for the calculation of the 3D

Figure 6.5 - Variations in the mean value of the number of photons counts.

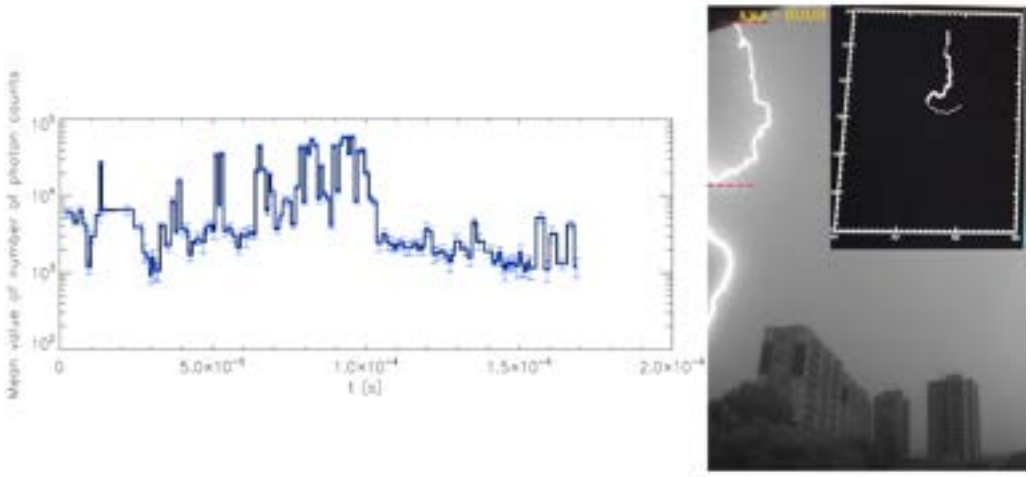

These variations occur over a period of time from 0 to 80 microseconds and correspond to the between the dashed lines of the photo.

data was the time of 37:717853, which was based on the high-speed camera, which is 37:717853. This initial time was added to the time that we calculated from the data. In this way, we look for the times in the x-ray data and we obtain the comparison shown in Figures 6.11 and 6.12. The black and purple curves are the mean number of photon counts (modeled data) and the green and blue curves are the x-ray signal as a function of time and of the number of points.

Figure 6.6 - Based on a fixed height of 100 meters, the energy variation as a function of angles (0^0 to 90^0).

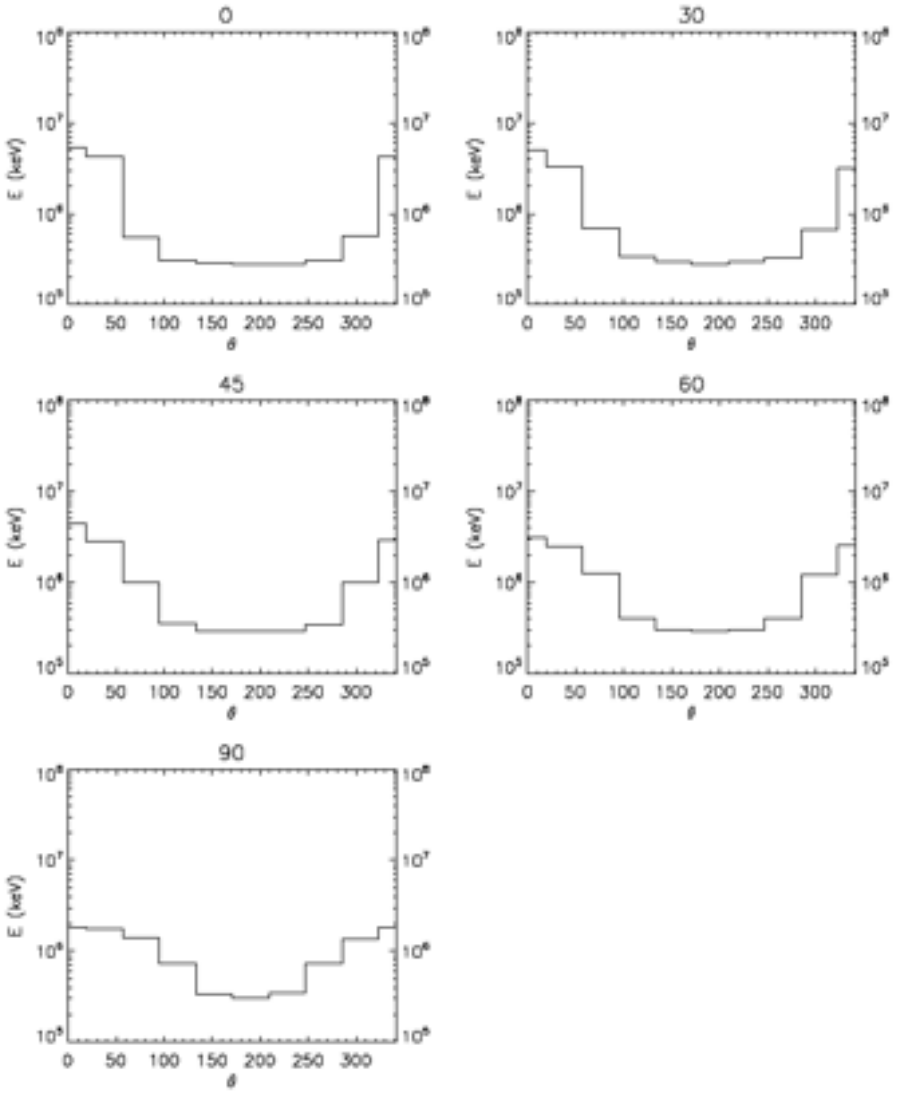

Comparison of the propagation of the modeled leader with observational data

In the present work, we present the comparison of the results of the data that we modeled (the propagation of the dart stepped leader) and the data registered by the x-ray and electric field sensors. With the purpose of understanding and knowing which part of the recorded data that variation of the displayed model result. In this way, it can be assumed that these variations may be caused by the physical processes

Figure 6.7 - Based on a fixed height of 100 meters, the energy variation as a function of angles (120^0 to 315^0).

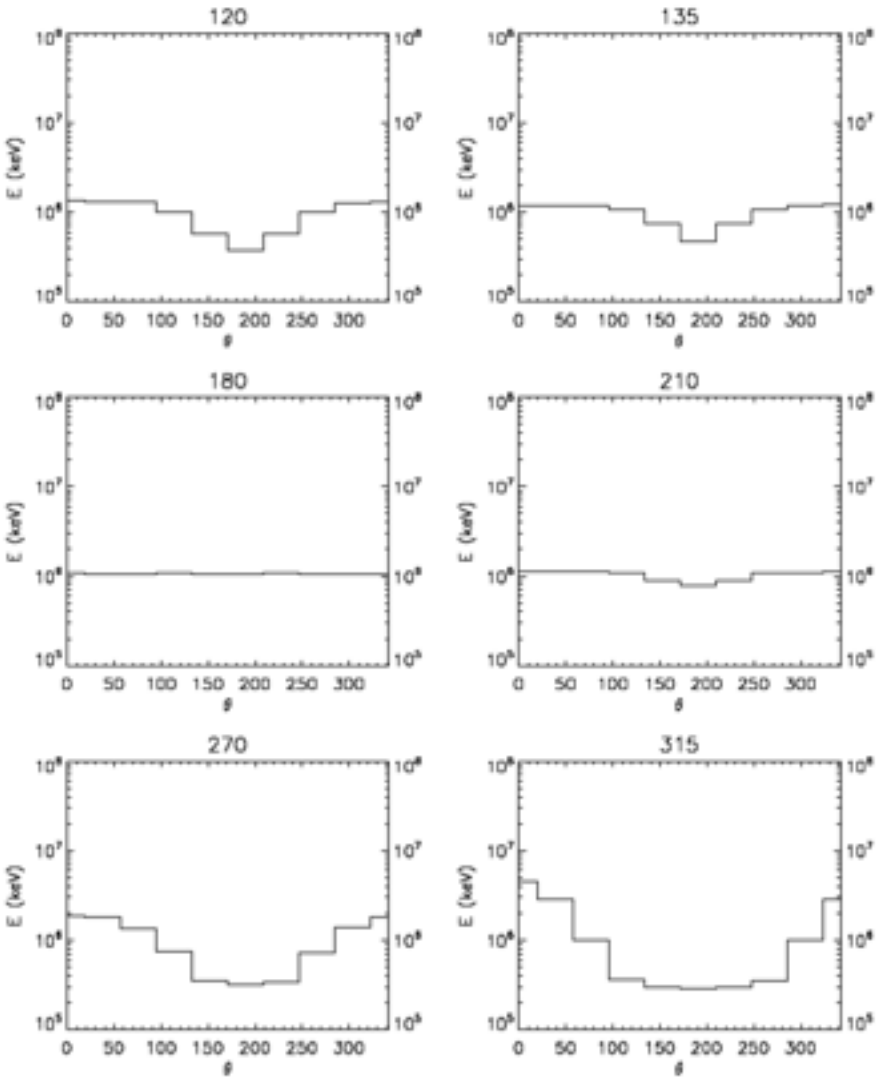

involved during the occurrence of x-rays generated by stepped leaders.

The 3D leader reconstruction data was made from this first event shown in Figure 6.10. We use all the information shown in this graph such as the electric field (red curve) and the response of the PMTs (blue and green curves) to then make a comparison with the results of the modeled and registered data. The dashed line indicates the time 718069 μs when the return discharge occurred.

Figure 6.14 shows the comparison of observed data with the simulations. The red

Figure 6.8 - Measurements of the energy based on the height (Z) which varies from 0 to 1000 meters and at angles of 60, 90, 315 and 45.

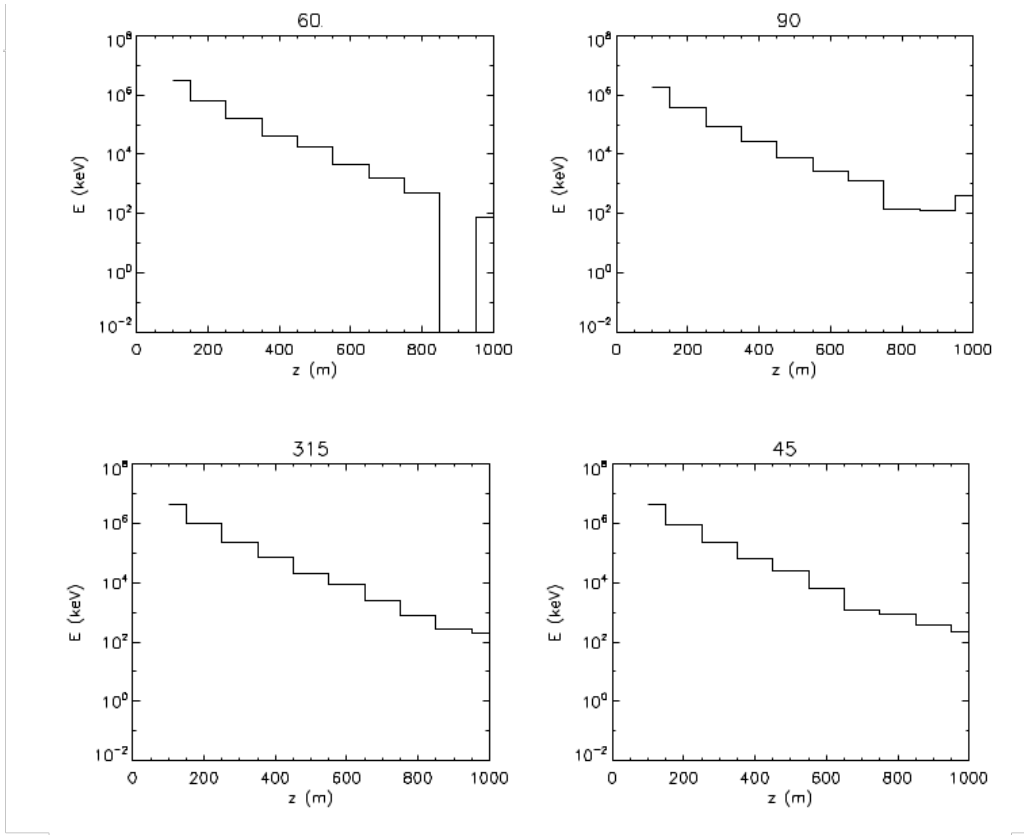

and black color curves are x-ray signals, the electric field sensor color curve is blue, and the green color curve is the response of the modeled data. The time interval between labels on the x-axis (26.44 μs) of the graph corresponds to the duration of each high-speed camera frame. The numbers 1 to 9 in the graph correspond to the nine frames of high-speed video recorded during the dart leader propagation (shown in Figure 6.13). It can be observed that the three x-ray pulses were observed during intervals 3 and 4 (SABA et al., 2019).

Figure 6.9 - Measurements of the energy based on the height (Z) which varies from 0 to 1000 meters and at angles of 0, 120, 135, 180, 210 and 30.

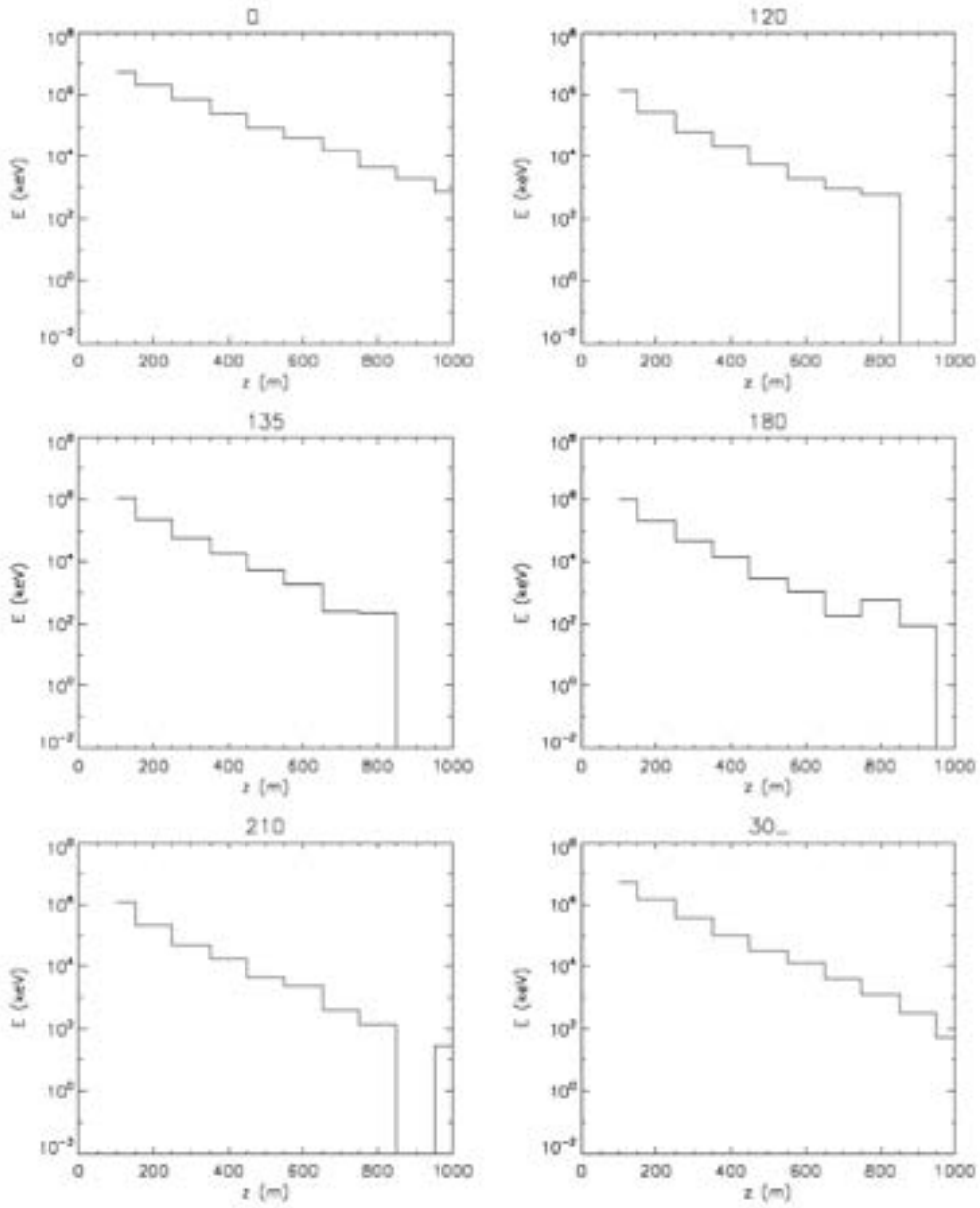

We also present the comparison of the model output with recorded data of temporal resolution of 5MS/s (x-ray and electric field data). These data were used in our publication of the first x-ray observation result (SABA et al., 2019). The comparison was also made to see if the x-ray variations are associated with the variations found in the model result.

Figure 6.10 - The 3D leader reconstruction data was made from first event on December 16, 2018.

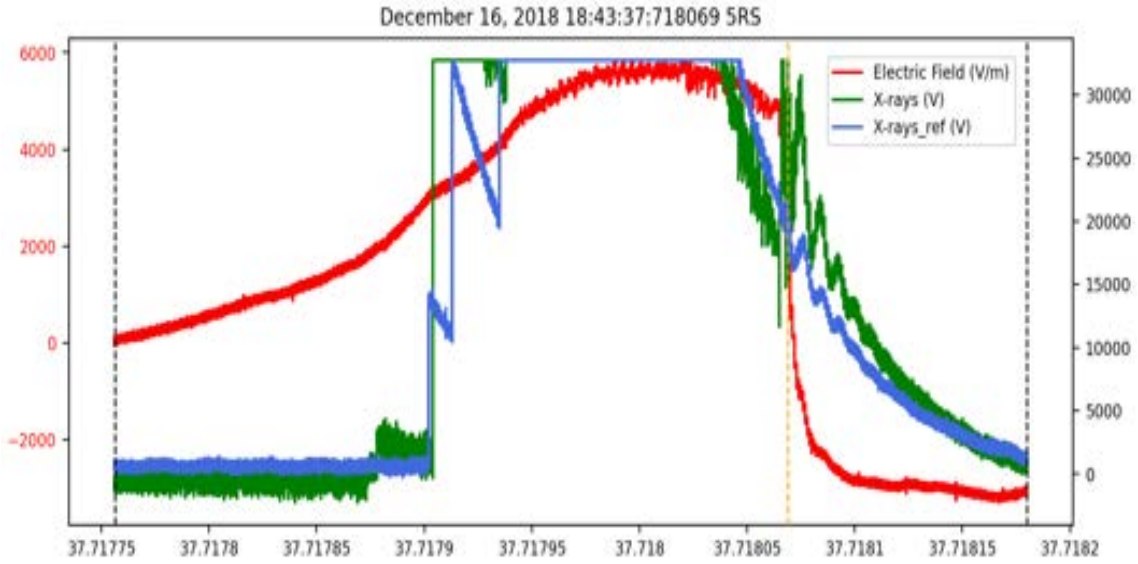

The curves of the colors green and blue, are the output signals of the x-ray (PMT) and the color red is the signal of the electric field. The vertical dotted lines in the graph correspond to the beginning of the return stroke.

Figure 6.11 - Comparison of the mean number of photons counts as a function of time.

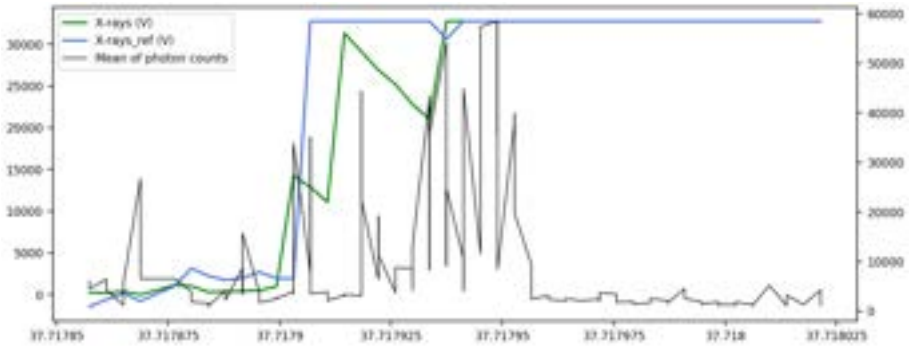

The black curve is the modeled data, and the green/blue curves represent the x-ray signal.

We calculate the difference between the final (37.718091) and initial (37.717853) time over the total time series (125) and thus create a 125-point array with this high-speed camera information. In this way we make the graph considering this time obtained, shown in Figure 6.15. In order to verify how the model behaves we

Figure 6.12 - Comparison of the mean number of photons counts as a function of points (time series).

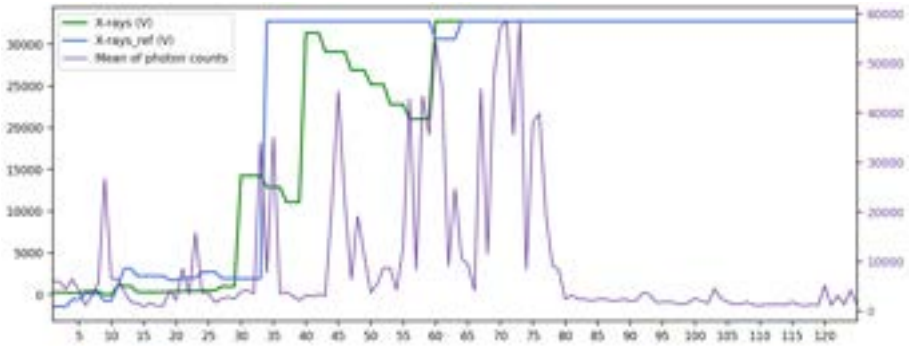

The purple curve is the modeled data, and the green/blue curves represent the x-ray signal.

Figure 6.13 - Images from two nearly orthogonal standard video cameras.

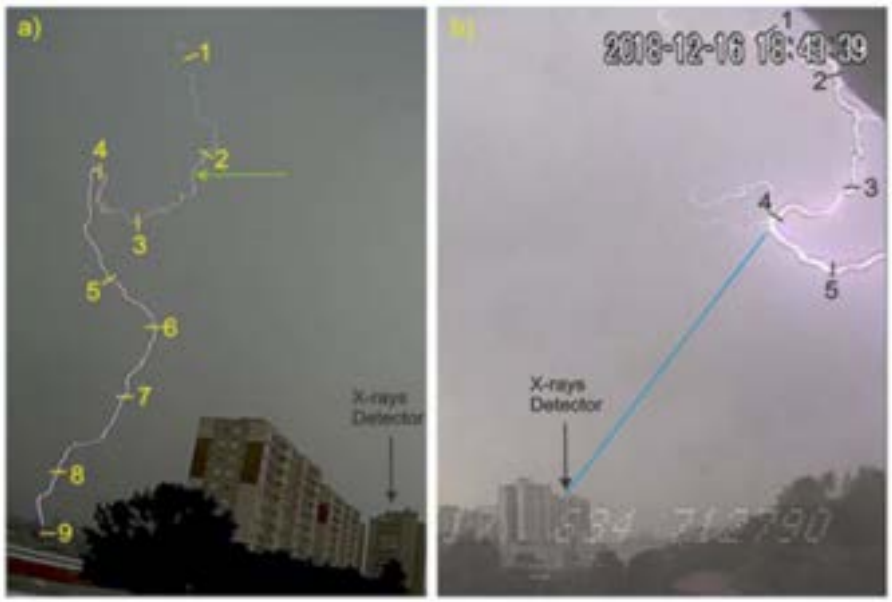

The numbered marks indicate the approximate location of the tip of the continuous leader at the end of each video frame recorded by the high-speed camera during the fifth return stroke

consider the initial and final time of the camera based on the development of the leader shown in Figure 6.13 and also corroborate with the final time of the x-ray development shown in Figure 6.10 to have a reference. The manipulation proceeded

Figure 6.14 - Electric field and x-ray measurements during continuous leader approach of fifth return flash.

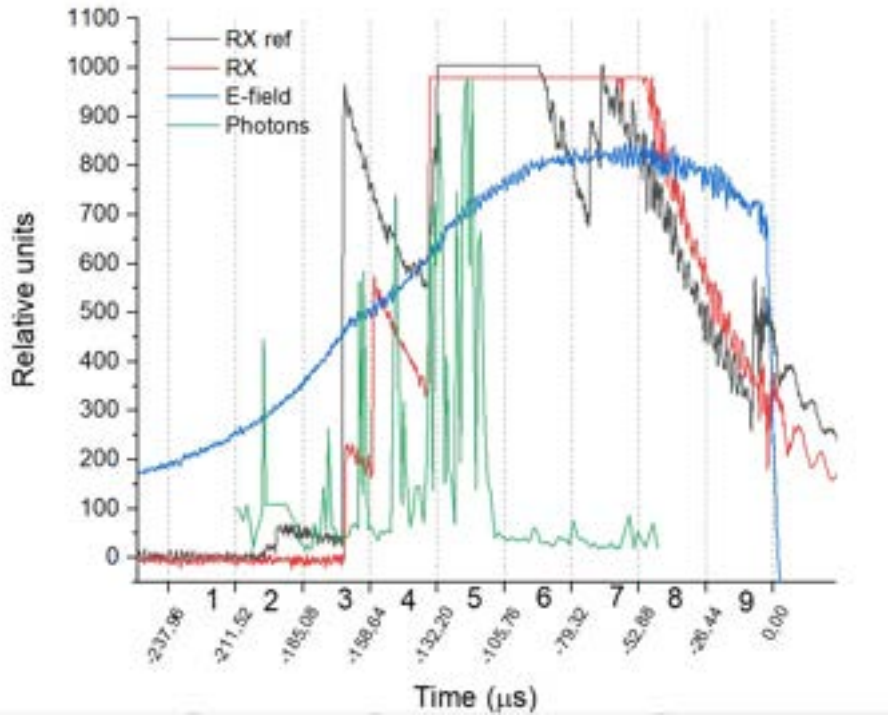

The red and black curves are the x-ray signal, the blue curve is the signal of the electric field and the green curve is the response of the modeled data.

because the time is unknown as mentioned above, but the initial time is the same as the time considered in the first point (time series) of 3D reconstruction. Also in that period of time, there are only 10 frames recorded in the high-speed camera. Supported by this result, we can once again associate the variations in the modeling data to be related to physical processes, the x-ray sensor response is in amplified mode and, it is saturated, and each x-ray pulse is integrated at 150 μ, which limits us to have complete information on the development of the x-ray pulses.

Figure 6.15 - Comparison of the mean number of photons counts as a function of time.

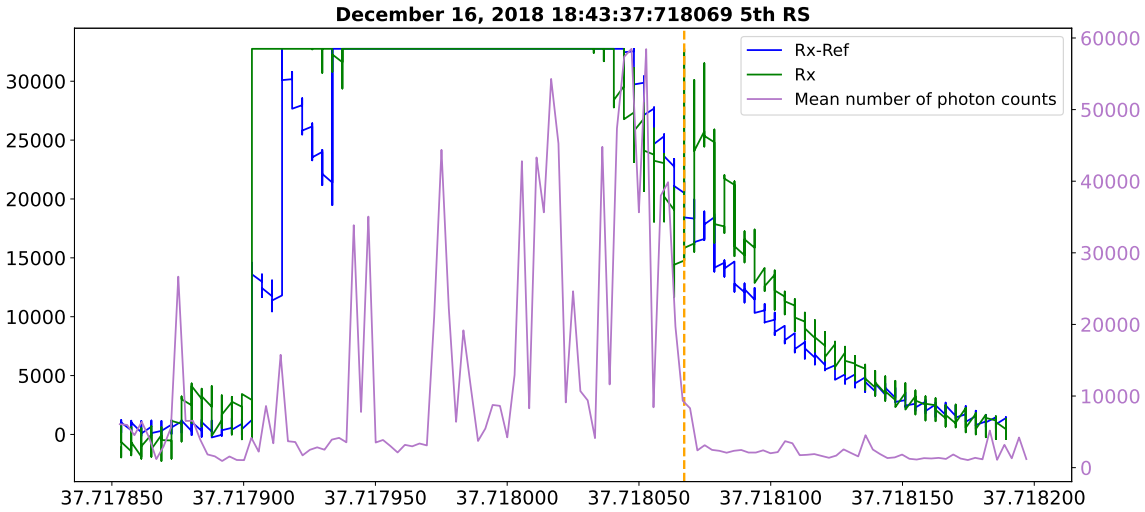

The purple curve is the modeled data, and the green/blue curves represent the x-ray signal.

7 CONCLUSIONS AND SUGGESTIONS FOR FUTURE WORK

Two x-ray events were recorded for the first time in Brazil, with the entire complete system (x-ray sensor, electric field sensor, high-speed and common cameras) in the building located in the city of São Paulo, called P1P2. The first x-ray event was recorded on December 16, 2018 (18:43:37 UT) and the second event on January 24, 2019 (17:52:20 UT), in both cases generated the production of x-rays was the dart-stepped leaders. In the two observed events, the (x-ray) emissions begin approximately 100 to 330 μs before the return stroke.

Calibration of sensors and installations of x-ray instruments and electric fields were carried out in both observation periods.

An analysis was made of all the data recorded by the PXI instruments from the first moment of operation until the end (both observation periods) as shown in the Tables in the appendix, finding two x-ray events.

To analyze the events produced, it was necessary to compare the recording time with the different instruments installed in the P1P2 building (detection system), the electric field sensor that was installed at the University of Sao Paulo (USP-IAG), lightning networks Brasildat and Rindat and the cameras.

X-ray emissions produced by natural lightning in Brazil were successfully measured during two observation periods at a distance of up to about 3.5 kilometers around the x-ray sensor, according to information obtained from the lightning detection and monitoring network (BrasilDat and RINDAT).

During the first observation period, a total of 85 lightning strikes in the P1P2 building were recorded by the x-ray and electric field sensor, the data were stored in the data acquisition system in the instruments PXI-National Instruments and a PC with a Meinberg GPS170PCI GPS card (NI PCI-6110 12-bit data acquisition card). In order to have time synchronization of all measurements, each of the devices has a GPS receiver.

In this work, the REAM model was used, based on the Monte Carlo method and developed by Professor Joseph Dwyer, and has been, in this work, adapted for the first time to simulations only with photons instead of runaway electrons, as is originally done in the model; in order to know the energy and compare the results of theoretical models and observational models.

For data processing, a data pre-processing methodology was created, which consists of selecting the maximum or minimum peaks of the electric field, in order to know the exact position of each variation of the electric field, thus creating a methodology for the rapid analysis of events related to x-rays. Due to the high temporal resolution of the data (33 MS/s), we had to optimize the computer's memory and facilitate the search for events related to x-rays. One of the codes is found in Appendix C.

The theoretical result shows that there is attenuation of the photons, which indicates that the modeled data suffers the loss of energy. The data were modeled using 100 keV E-folding, so the energy range is likely to be approximately between 10^3 to 10^7 keV as shown in Figure 6.4, so, we can assume that the physical processes involved in the development of the model vary in that energy range.

In this study, we have for the first time observed, modeled and analyzed the propagation of natural lightning that produced the x-rays, which were observed in São Paulo on 16 December 2018 at 18:43:37:718065. We have used 3D leader propagation data obtained from high-speed and common cameras. Based on our analysis of the modeled and recorded data (x-rays and electric field sensors), we found a difference in leader development when using time calculated from the 3D data. We believe that this occurs because, when performing the 3D reconstruction, the corresponding time in each time series found was not taken into account. Perhaps due to the limitations of the common camera with low resolution, and this difference can be seen in the Figures 6.11 and 6.12. The modeled data (purple curve) does not follow the response of the mentioned sensor (green, blue and red curves).

The result of the manipulation that was carried out taking into account the initial and final time of the camera (only 10 frames) based on the development of the leader, we can say that the results of the modeled data (purple curve) accompany the observed data (blue and green curves). Apart from that, the variation of the model result occurs before the return discharge occurs, as can be seen in Figure 6.15.

Our comparison of the model results using optical data(cameras) and data recorded by x-ray sensors shows variations that may be attributed to the physical processes involved during the occurrence of x-rays. Perhaps more comparisons are needed to determine what exactly is happening and what these variations are related to. In our case we are considering only photon interaction and taking into account the four physical processes mentioned above. Furthermore, this is the first comparison of optical and recorded data considering photons as propagation source in the stepped

leader. To analyze the physical processes in more detail and know, for example, the x-ray energy produced by the stepped leaders, it is necessary that the PMTs (x-ray sensors) are operating in non-amplified mode.

In order to obtain information about the time, the development of the leader's propagation, and possibly more details when comparing the results of modeled data and registered data, it is recommended to use several high-speed cameras in different positions and with the same temporal resolution for the next observations.

REFERENCES

BABICH, L. P.; DONSKOY, E. N.; KUTSYK, I. M.; ROUSSEL-DUPRÉ, R. A. The feedback mechanism of runaway air breakdown. **Geophysical Research Letters**, v. 32, n. 9, p. L09809, May 2005. 16

BABICH, L. P.; DONSKOY, E. N.; ROUSSEL-DUPRÉ, R. A. Study of relativistic electron avalanche enhancement in the atmosphere at low overvoltages due to avalanche bremsstrahlung. **Geomagnetism and Aeronomy**, v. 47, n. 4, p. 515–524, Aug 2007. 16

BEASLEY, W.; UMAN, M. A.; RUSTAN P. L., J. Electric fields preceding cloud-to-ground lightning flashes. **Journal of Geophysical Research: Oceans**, v. 87, n. C7, p. 4883–4902, Jun 1982. 1

COLEMAN, L. M.; DWYER, J. R. Propagation speed of runaway electron avalanches. **Geophysical Research Letters**, v. 33, n. 11, p. L11810, Jun 2006. 11

COORAY, V. **Lightning**. [S.l.: s.n.], 2003. 698 p. 1

COORAY, V.; LOBATO, A. The Energy, momentum, and peak power radiated by negative lightning return strokes. **Atmosphere**, v. 11, n. 12, p. 1288, nov. 2020. 33

CRAMER, E. S.; DWYER, J. R.; ARABSHAHI, S.; VODOPIYANOV, I. B.; LIU, N.; RASSOUL, H. K. An analytical approach for calculating energy spectra of relativistic runaway electron avalanches in air. **Journal of Geophysical Research (Space Physics)**, v. 119, n. 9, p. 7794–7823, Sep 2014. 10, 11, 12, 13, 14, 20, 48

DWYER, J. R. A fundamental limit on electric fields in air. **Geophysical Research Letters**, v. 30, n. 20, p. 2055, Oct 2003. 3, 7, 9, 15, 16, 20, 23

DWYER, J. R. Implications of x-ray emission from lightning. **Geophysical Research Letters**, v. 31, n. 12, p. L12102, Jun 2004. 3, 8, 15

DWYER, J. R. The initiation of lightning by runaway air breakdown. **Geophysical Research Letters**, v. 32, n. 20, p. L20808, Oct 2005. 15

DWYER, J. R. Relativistic breakdown in planetary atmospheres. **Physics of Plasmas**, v. 14, n. 4, p. 042901–042901, Apr 2007. 20

DWYER, J. R. The relativistic feedback discharge model of terrestrial gamma ray flashes. **Journal of Geophysical Research (Space Physics)**, v. 117, n. A2, p. A02308, Feb 2012. 9, 20

DWYER, J. R.; SMITH, D. M. A comparison between Monte Carlo simulations of runaway breakdown and terrestrial gamma-ray flash observations. **Geophysical Research Letters**, v. 32, n. 22, p. L22804, Nov 2005. 3

DWYER, J. R.; SMITH, D. M.; CUMMER, S. A. High-energy atmospheric physics: terrestrial gamma-ray flashes and related phenomena. **Space Science Reviews**, v. 173, n. 1-4, p. 133–196, Nov 2012. 3, 21

DWYER, J. R.; SMITH, D. M.; CUMMER, S. A. High-energy atmospheric physics: terrestrial gamma-ray flashes and related phenomena. **Space Science Reviews**, v. 173, n. 1-4, p. 133–196, Nov 2012. 11, 15, 16, 17

DWYER, J. R.; UMAN, M. A. The physics of lightning. **Physics Reports**, v. 534, n. 4, p. 147–241, Jan 2014. 37

DWYER, J. R.; UMAN, M. A.; RASSOUL, H. K.; AL-DAYEH, M.; CARAWAY, L.; JERAULD, J.; RAKOV, V. A.; JORDAN, D. M.; RAMBO, K. J.; CORBIN, V. et al. Energetic radiation produced during rocket-triggered lightning. **Science**, v. 299, n. 5607, p. 694–697, 2003. Available from: <<https://www.science.org/doi/abs/10.1126/science.1078940>>. 39, 45

EACK, K. B.; BEASLEY, W. H.; RUST, W. D.; MARSHALL, T. C.; STOLZENBURG, M. X-ray pulses observed above a mesoscale convective system. **Geophysical Research Letters**, v. 23, n. 21, p. 2915–2918, Jan 1996. 3

GAMEROTA, W. R.; IDONE, V. P.; UMAN, M. A.; NGIN, T.; PILKEY, J. T.; JORDAN, D. M. Dart-stepped-leader step formation in triggered lightning. **Geophysical Research Letters**, v. 41, n. 6, p. 2204–2211, 2014. Available from: <<https://agupubs.onlinelibrary.wiley.com/doi/abs/10.1002/2014GL059627>>. 45

GUREVICH, A. V.; MILIKH, G. M.; ROUSSEL-DUPRE, R. Runaway electron mechanism of air breakdown and preconditioning during a thunderstorm. **Physics Letters A**, v. 165, n. 5-6, p. 463–468, Jun 1992. 1, 9

GUREVICH, A. V.; VALDIVIA, J. A.; MILIKH, G. M.; PAPADOPOULOS, K. Runaway electrons in the atmosphere in the presence of a magnetic field. **Radio Science**, v. 31, n. 6, p. 1541–1554, Nov 1996. 1, 8

GUREVICH, A. V.; ZYBIN, K. P. Reviews of topical problems: runaway breakdown and electric discharges in thunderstorms. **Physics Uspekhi**, v. 44, n. 11, p. 1119–1140, Nov 2001. 9

HETTIARACHCHI, P.; COORAY, V.; DIENDORFER, G.; PICHLER, H.; DWYER, J.; RAHMAN, M. X-ray observations at gaisberg tower. **Atmosphere**, MDPI, v. 9, n. 1, p. 20, 2018. 3, 45

INAN, U. S.; PIDDYACHIY, D.; PETER, W. B.; SAUVAUD, J.; PARROT, M. Demeter satellite observations of lightning-induced electron precipitation. **Geophysical research letters**, Wiley Online Library, v. 34, n. 7, 2007. 33

JACKSON, J. D. **Classical electrodynamics**. [S.l.]: American Association of Physics Teachers, 1999. 13

JERAULD, J.; UMAN, M. A.; RAKOV, V. A.; RAMBO, K. J.; SCHNETZER, G. H. Insights into the ground attachment process of natural lightning gained from an unusual triggered-lightning stroke. **Journal of Geophysical Research (Atmospheres)**, v. 112, n. D13, p. D13113, Jul 2007. 2

KNOLL, G. F. **Radiation detection and measurement**. [S.l.]: John Wiley & Sons, 2010. 49, 50, 51

LEHTINEN, N. G.; BELL, T. F.; INAN, U. S. Monte carlo simulation of runaway mev electron breakdown with application to red sprites and terrestrial gamma ray flashes. **Journal of Geophysical Research: Space Physics**, v. 104, n. A11, p. 24699–24712, 1999. Available from: <<https://agupubs.onlinelibrary.wiley.com/doi/abs/10.1029/1999JA900335>>. 20

MALLICK, S.; RAKOV, V.; DWYER, J. R. A study of x-ray emissions from thunderstorms with emphasis on subsequent strokes in natural lightning. **Journal of Geophysical Research: Atmospheres**, v. 117, n. D16, 2012. 3, 37

MARSHALL, T. C.; MCCARTHY, M. P.; RUST, W. D. Electric field magnitudes and lightning initiation in thunderstorms. **Journal of Geophysical Research: Atmospheres**, v. 100, n. D4, p. 7097–7103, 1995. Available from: <<https://agupubs.onlinelibrary.wiley.com/doi/abs/10.1029/95JD00020>>. 7

MCCARTHY, M.; PARKS, G. K. Further observations of X-rays inside thunderstorms. **Geophysical Research Letters**, v. 12, n. 6, p. 393–396, Jun 1985. 3

MCCARTHY, M. P.; PARKS, G. K. On the Modulation of X Ray Fluxes in Thunderstorms. **Journal of Geophysical Research: Atmospheres**, v. 97, n. D5, p. 5857–5864, Apr 1992. 9

MEDEIROS, D. d. S. F. **Estudo dos processos físicos de relâmpagos com a utilização de imagens em 3D**. Dissertação (Mestrado em Geofísica Espacial) — Instituto Nacional de Pesquisas Espaciais (INPE), São José dos Campos, 2020. 46

MONTANYà, J.; FABRó, F.; VELDE, O. van der; ROMERO, D.; SOLà, G.; HERMOSO, J. R.; SOULA, S.; WILLIAMS, E. R.; PINEDA, N. Registration of x-rays at 2500m altitude in association with lightning flashes and thunderstorms. **Journal of Geophysical Research: Atmospheres**, v. 119, n. 3, p. 1492–1503, 2014. Available from: <<https://agupubs.onlinelibrary.wiley.com/doi/abs/10.1002/2013JD021011>>. 46

MOORE, C. B.; EACK, K. B.; AULICH, G. D.; RISON, W. Energetic radiation associated with lightning stepped-leaders. **Geophysical Research Letters**, v. 28, n. 11, p. 2141–2144, Jan 2001. 3, 15

PARKS, G. K.; MAUK, B. H.; SPIGER, R.; CHIN, J. X-ray enhancements detected during thunderstorm and lightning activities. **Geophysical Research Letters**, v. 8, n. 11, p. 1176–1179, Nov 1981. 3

RAKOV, V. A.; UMAN, M. A. **Lightning**. [S.l.: s.n.], 2003. 698 p. 1, 2, 4, 9

ROSSI, B. **High energy particles**. Amsterdam: No. OCLC-289682, 1952. 12

SABA, M. M. F.; FERRO, M. A. S.; CUADROS, E. T.; CUSTÓDIO, D. M.; NAG, A.; SCHUMANN, C.; COORAY, V.; PAIVA, A. R.; LAURIA, P. B.; MEDEIROS, D. S. F.; HETTIARACHCHI, P.; RASSOUL, H. K. High-speed video observation of a dart leader producing x-rays. **Journal of Geophysical Research (Space Physics)**, v. 124, n. 12, p. 10,564–10,570, Dec 2019. 32, 46, 47, 58, 59

SALEH, Z.; DWYER, J.; HOWARD, J.; UMAN, M.; BAKHTIARI, M.; CONCHA, D.; STAPLETON, M.; HILL, D.; BIAGI, C.; RASSOUL, H. Properties of the X-ray emission from rocket-triggered lightning as measured by the Thunderstorm Energetic Radiation Array (TERA). **Journal of Geophysical Research (Atmospheres)**, v. 114, n. D17, p. D17210, Sep 2009. 3, 23

SIZYKH, S. V. Runaway electron production rate in gaseous discharges. **High Temperature**, v. 31, p. 1–6, 1993. 15

WILSON, C. T. R. The Acceleration of β-particles in Strong Electric Fields such as those of Thunderclouds. **Proceedings of the Cambridge Philosophical Society**, v. 22, n. 4, p. 534, Jan 1925. 3, 7

WINN, W. P.; MOORE, C. B. Electric field measurements in thunderclouds using instrumented rockets. **Journal of Geophysical Research**, v. 76, n. 21, p. 5003–5017, Jul 1971. 1

APPENDIX A

A.1 x-ray and electric field data recorded by *PXI-National Instruments*

Plots and analyzes were made of all data recorded by PXI from the beginning of operations until January 16, 2020 (both periods). All tables show the dates and times of lightning activity recorded simultaneously, with the Lightning Detection and Location Networks (BrasilDAT and RINDAT). In addition, the Tables, it is shown only for the years 2018 and 2019.

Table A.1 - It shows the dates and times of lightning activity recorded by PXI and some parameters provided between December 2018 and March 2019 Lightning Detection and Location Network.

Date and Time	**Data recorded by PXI**			
	Intensity of current	**Electric Field**	**NET Lightning**	**Rx**
2018-12-01 01:00:01	87	yes	27.216 km (P1P2)	-
2018-12-01 03:00:50	171	yes	22.964 km (P1P2)	-
2018-12-01 03:00:50	28	yes	25.579 km (P1P2)	-
2018-12-16 18:43:37	-7	yes	12.572 km (P1P2)	-
2018-12-16 18:43:37	-19	yes	12.503 km (P1P2)	-
2018-12-16 18:43:37	-18	yes	11.249 km (P1P2)	-
2018-12-16 18:43:37	-12	yes	9.859 km (P1P2)	-
lightgray 2018-12-16 18:43:37	-38	yes	11.997 km (P1P2)	yes
2018-12-16 18:43:37	-3	yes	12.625 km (P1P2)	-
2018-12-16 18:43:37	-6	yes	12.185 km (P1P2)	-
2018-12-16 18:43:37	-6	yes	12.792k km (P1P2)	-
2018-12-16 18:43:37	-12	yes	11.855 km (P1P2)	-
2018-12-16 20:41:12	28	yes	20.579 km (P1P2)	-
2018-12-16 20:41:12	27	yes	21.685 km (P1P2)	-
2018-12-16 20:41:12	4	yes	21.707 km (P1P2)	-
2018-12-16 20:48:18	7	yes	22.127 km (P1P2)	-
2018-12-16 20:48:18	5	yes	22.078 km (P1P2)	-
2018-12-16 20:48:18	6	yes	21.554 km (P1P2)	-

continue

Table A.1 Continuation.

Date and Time	Data recorded by PXI			
	Intensity of current	**Electric Field**	**NET Lightning**	**Rx**
2018-12-16 21:01:52	-6	yes	14.737 km (P1P2)	-
2018-12-18 06:34:58	14	yes	19.871 km (P1P2)	-
2018-12-18 06:34:58	-6	yes	20.603 km (P1P2)	-
2018-12-18 06:34:58	-15	yes	23.612 km (P1P2)	-
2018-12-18 06:34:58	5	yes	16.547 km (P1P2)	-
2018-12-18 06:34:58	4	yes	21.644 km (P1P2)	-
2018-12-18 06:36:25	7	yes	5.917 km (P1P2)	-
2018-12-18 06:38:41	-13	yes	23.654 km (P1P2)	-
2018-12-18 06:43:54	9	yes	12.471 km (P1P2)	-
2018-12-19 02:18:01	-4	-	22.321 km (P1P2)	-
2018-12-19 02:18:01	-31	-	19.795 km (P1P2)	-
2018-12-19 02:18:01	-10	-	19.798 km (P1P2)	-
2018-12-19 02:18:01	-16	-	21.250 km (P1P2)	-
2018-12-18 02:19:30	-100	-	22.375 km (P1P2)	-
2018-12-18 02:19:30	-38	-	22.699 km (P1P2)	-
2018-12-18 02:19:30	-18	-	22.522 km (P1P2)	-
2018-12-23 22:33:43	-17	yes	13.883 km (P1P2)	-
2019-01-11 00:11:22	-22	yes	13.914 km	-
2019-01-11 00:19:18	4	yes	12.399 km (P1P2)	-
2019-01-11 00:19:18	4	yes	14.178 km (P1P2)	-
2019-01-11 00:19:18	-5	yes	15.363 km (P1P2)	-
2019-01-11 00:19:18	10	yes	12.863 km (P1P2)	-
2019-01-11 00:19:18	3	yes	10.344 km (P1P2)	-
2019-01-11 00:26:32	-16	yes	11.658 km (P1P2)	-
2019-01-11 00:27:59	-23	yes	10.895 km (P1P2)	-
2019-01-11 00:27:59	-7	yes	11.754 km (P1P2)	-
2019-01-11 00:32:21	-17	yes	10.860 km (P1P2)	-
2019-01-11 00:32:21	-20	yes	10.678 km (P1P2)	-
2019-01-11 00:32:21	-4	yes	13.035 km (P1P2)	-
2019-01-11 00:32:21	-32	yes	10.632 km (P1P2)	-

continue

Table A.1 Continuation.

Date and Time	Data recorded by PXI			
	Intensity of current	**Electric Field**	**NET Lightning**	**Rx**
2019-01-11 00:32:21	5	yes	9.941 km (P1P2)	-
2019-01-17 20:34:20	5	yes	15.819 km (P1P2)	-
2019-01-17 20:34:20	-16	yes	15.177 km (P1P2)	-
2019-01-17 20:34:20	-6	yes	14.115 km (P1P2)	-
2019-01-17 20:36:28	-8	yes	14.966 km (P1P2)	-
2019-01-17 20:36:28	-33	yes	15.641 km (P1P2)	-
2019-01-17 20:36:28	-12	yes	15.207 km (P1P2)	-
2019-01-17 20:36:28	-28	yes	15.698 km (P1P2)	-
2019-01-17 20:36:28	-19	yes	14.925 km (P1P2)	-
2019-01-17 20:36:28	-22	yes	15.563 km (P1P2)	-
2019-01-17 20:36:28	-13	yes	14.940 km (P1P2)	-
2019-01-23 19:53:03	-35	yes	17.268 km (P1P2)	-
2019-01-23 19:53:03	-7	yes	17.384 km (P1P2)	-
2019-01-23 19:53:03	-4	yes	16.880 km (P1P2)	-
2019-01-23 19:53:03	-4	yes	16.747 km (P1P2)	-
2019-01-23 19:53:03	-6	yes	17.090 km (P1P2)	-
2019-01-23 19:53:03	-9	yes	17.289 km (P1P2)	-
2019-01-23 19:53:03	-6	yes	17.886 km (P1P2)	-
2019-01-23 19:53:03	-6	yes	17.646 km (P1P2)	-
2019-01-23 19:53:03	-6	yes	17.102 km (P1P2)	-
2019-01-24 17:16:57	-4	yes	16.946 km (P1P2)	-
2019-01-24 17:20:53	-6	yes	17.320 km (P1P2)	-
2019-01-24 17:21:36	-17	yes	15.224 km (P1P2)	-
2019-01-24 17:23:17	-9	yes	14.921 km (P1P2)	-
2019-01-24 17:47:36	-19	yes	13.843 km (P1P2)	-
2019-01-24 17:47:36	-45	yes	17.720 km (P1P2)	-
2019-01-24 17:47:36	-24	yes	14.142 km (P1P2)	-
2019-01-24 17:47:36	-8	yes	13.661 km (P1P2)	-
2019-01-24 17:52:20	-12	yes	12.493 km (P1P2)	-
2019-01-24 17:52:20	-12	yes	12.643 km (P1P2)	-

continue

Table A.1 Continuation.

Date and Time	Data recorded by PXI			
	Intensity of current	**Electric Field**	**NET Lightning**	**Rx**
2019-01-24 17:52:20	-5	yes	12.818 km (P1P2)	-
2019-01-24 17:55:52	-12	yes	13.5533 km (P1P2)	-
2019-01-24 18:00:59	-17	yes	13.532 km (P1P2)	-
2019-01-24 18:16:42	-9	yes	10.223 km (P1P2)	-
2019-01-24 18:16:42	-18	yes	13.650 km (P1P2)	-
2019-01-24 18:16:42	-8	yes	8.233 km (P1P2)	-
2019-01-25 19:56:05	-18	yes	17.023 km (P1P2)	-
2019-01-25 19:56:05	-25	yes	16.908 km (P1P2)	-
2019-01-25 20:07:35	25	yes	36.704 km (P1P2)	-
2019-01-25 20:07:35	8	yes	27.161 km (P1P2)	-
2019-01-25 20:11:21	28	yes	4.636 km (P1P2)	-
2019-01-25 20:11:21	-17	yes	16.676 km (P1P2)	-
2019-01-25 20:16:34	38	yes	43.661 km (P1P2)	-
2019-01-25 20:21:35	8	yes	46.706 km (P1P2)	-
2019-01-25 20:23:49	-9	yes	25.621 km (P1P2)	-
2019-01-25 20:23:49	-8	yes	19.225 km (P1P2)	-
2019-01-25 20:23:49	-8	yes	21.353 km (P1P2)	-
2019-01-25 20:25:20	51	yes	19.772 km (P1P2)	-
2019-01-25 20:25:20	6	yes	21.374 km (P1P2)	-
2019-01-25 20:25:20	5	yes	20.874 km (P1P2)	-
2019-01-30 19:31:41	-5	yes	9.906 km (P1P2)	-
2019-01-30 19:31:41	21	yes	13.469 k km (P1P2)	-
2019-01-30 19:33:54	-20	yes	15.128 km (P1P2)	-
2019-01-30 19:37:46	-18	yes	35.157 km (P1P2)	-
2019-01-30 19:40:04	-26	yes	9.946 km (P1P2)	-
2019-01-30 19:40:04	-32	yes	11.420 km (P1P2)	-
2019-01-30 19:40:04	-20	yes	12.704 km (P1P2)	-
2019-01-30 19:40:04	-7	yes	14.461 km (P1P2)	-
2019-01-30 19:40:04	-17	yes	14.498 km (P1P2)	-
2019-01-30 19:40:04	-18	yes	14.534 km (P1P2)	-
2019-01-30 19:40:04	-6	yes	14.916 km (P1P2)	-

continue

Table A.1 Continuation.

Date and Time	Data recorded by PXI			
	Intensity of current	**Electric Field**	**NET Lightning**	**Rx**
2019-01-30 19:40:04	-8	yes	14.639 km (P1P2)	-
2019-01-30 19:40:04	-6	yes	15.107 km (P1P2)	-
2019-01-30 19:40:04	-16	yes	15.121 km (P1P2)	-
2019-01-30 19:41:21	-15	yes	11.699 km (P1P2)	-
2019-01-30 19:42:07	-50	yes	12.477 km (P1P2)	-
2019-01-30 19:42:07	-28	yes	12.980 km (P1P2)	-
2019-01-30 19:42:07	-20	yes	12.467 km (P1P2)	-
2019-01-30 19:42:07	-24	yes	12.296 km (P1P2)	-
2019-01-30 19:42:07	-23	yes	12.332 km (P1P2)	-
2019-01-30 19:42:07	-6	yes	12.056 km (P1P2)	-
2019-01-30 19:43:01	-25	yes	20.874 km (P1P2)	-
2019-02-22 20:10:47	-7	yes	15.134 km (P1P2)	-
2019-02-22 20:10:47	-9	yes	18.179 km (P1P2)	-
2019-02-22 20:15:34	-4	yes	10.142 km (P1P2)	-
2019-02-22 20:15:34	-6	yes	9.966 km (P1P2)	-
2019-02-22 20:15:34	-5	yes	10.793 km (P1P2)	-
2019-02-22 20:15:34	-6	yes	15.083 km (P1P2)	-
2019-02-22 20:49:51	16	yes	19.181 km (P1P2)	-
2019-02-22 20:49:51	8	yes	18.761 km (P1P2)	-
2019-02-22 20:49:51	-9	yes	15.225 km (P1P2)	-
2019-02-22 20:49:51	-4	yes	18.361 km (P1P2)	-
2019-02-22 20:49:51	9	yes	21.051 km (P1P2)	-
2019-02-22 20:49:51	10	yes	17.085 km (P1P2)	-
2019-02-22 20:49:51	-7	yes	14.575 km (P1P2)	-
2019-02-22 20:49:51	-4	yes	19.219 km (P1P2)	-
2019-02-22 20:49:51	5	yes	16.494 km (P1P2)	-
2019-02-22 20:49:51	3	yes	18.436 km (P1P2)	-
2019-02-22 21:01:37	249	yes	27.422 km (P1P2)	-
2019-02-22 21:01:37	109	yes	6.900 km (P1P2)	-
2019-02-26 01:06:28	-21	yes	17.110 km (P1P2)	-
2019-02-26 01:06:28	5	yes	17.047 km (P1P2)	-

continue

Table A.1 Continuation.

Date and Time	Data recorded by PXI			
	Intensity of current	**Electric Field**	**NET Lightning**	**Rx**
2019-02-26 01:06:28	-5	yes	17.525 km (P1P2)	-
2019-03-02 21:56:04	-5	yes	7.335 km (P1P2)	-
2019-03-02 21:56:04	-2	yes	7.080 km (P1P2)	-
2019-03-02 21:56:04	4	yes	6.215 km (P1P2)	-
2019-03-02 21:56:04	-27	yes	11.897 km (P1P2)	-
2019-03-02 21:56:04	-16	yes	12.230 km (P1P2)	-
2019-03-02 21:56:04	-7	yes	3.060 km (P1P2)	-
2019-03-02 22:00:44	3	yes	8.404 km (P1P2)	-
2019-03-02 22:00:44	5	yes	10.572 km (P1P2)	-
2019-03-02 22:00:44	3	yes	11.636 km (P1P2)	-
2019-03-02 22:00:44	-70	yes	15.141 km (P1P2)	-
2019-03-02 22:00:44	-2	yes	10.100 km (P1P2)	-
2019-03-02 22:12:48	9	yes	10.275 km (P1P2)	-
2019-03-02 22:12:48	-5	yes	11.239 km (P1P2)	-
2019-03-02 22:12:48	4	yes	9.723 km (P1P2)	-
2019-03-02 22:18:35	6	yes	8.644 km (P1P2)	-
2019-03-02 22:18:35	-5	yes	9.333 km (P1P2)	-
2019-03-02 22:18:44	-16	yes	14.657 km (P1P2)	-
2019-03-02 22:18:44	-10	yes	10.248 km (P1P2)	-
2019-03-02 22:18:44	-22	yes	9.564 km (P1P2)	-
2019-03-02 22:18:44	-12	yes	13.549 km (P1P2)	-
2019-03-02 22:18:44	-23	yes	14.040 km (P1P2)	-
2019-03-02 22:32:35	9	yes	13.681 km (P1P2)	-
2019-03-02 22:32:35	-5	yes	19.939 km (P1P2)	-
2019-03-02 22:32:35	-6	yes	15.067 km (P1P2)	-
2019-03-07 18:00:34	-12	yes	9.616 km (P1P2)	-
2019-03-07 18:00:34	-16	yes	8.434 km (P1P2)	-
2019-03-07 18:04:14	-41	yes	5.800 km (P1P2)	-
2019-03-07 18:04:14	-36	yes	5.975 km (P1P2)	-

continue

Table A.1: Conclusão.

Date and Time	**Data recorded by PXI**			
	Intensity of current	**Electric Field**	**NET Lightning**	**Rx**
2019-03-19 21:20:40	4	yes	7.815 km (P1P2)	-
2019-03-19 21:21:51	-4	yes	11.570 km (P1P2)	-
2019-03-19 21:21:51	6	yes	12.267 km (P1P2)	-
2019-03-12 20:52:41	-15	yes	7.938 km (P1P2)	-
2019-03-12 20:52:41	-24	yes	7.317 km (P1P2)	-

APPENDIX B

B.1 Testing of x-ray detectors

These instruments were calibrated at the Department of Physics and Space Sciences at the Florida Institute of Technology and verified prior to operating in Brazil. These tests were carried out in the Dosimetry Laboratory at the Institute for Advanced Studies (IEAv), in the plasma laboratory of the Technological Institute of Aeronautics (ITA), and at the National Institute for Space Research (INPE) at the laboratory (ELAT). The peaks of the amplitudes of the wave-forms of the x-ray sensors named PMT1 (serial number: 60009-01460-l(NaI (Tl)/PMT)) and serial number: 09159359 of PMT base (voltage divider) were measured) and PMT2 (sensor serial number 60003-06386-l(NaI(Tl)/PMT) and base PMT (voltage divider) serial number: 09166600). Figure B.1, shows the response of the sensors to different radioactive samples such as cesium-137(Cs), americium-241(Am), and sodium iodide(NaI).

Figure B.1 - The x-ray sensor response.

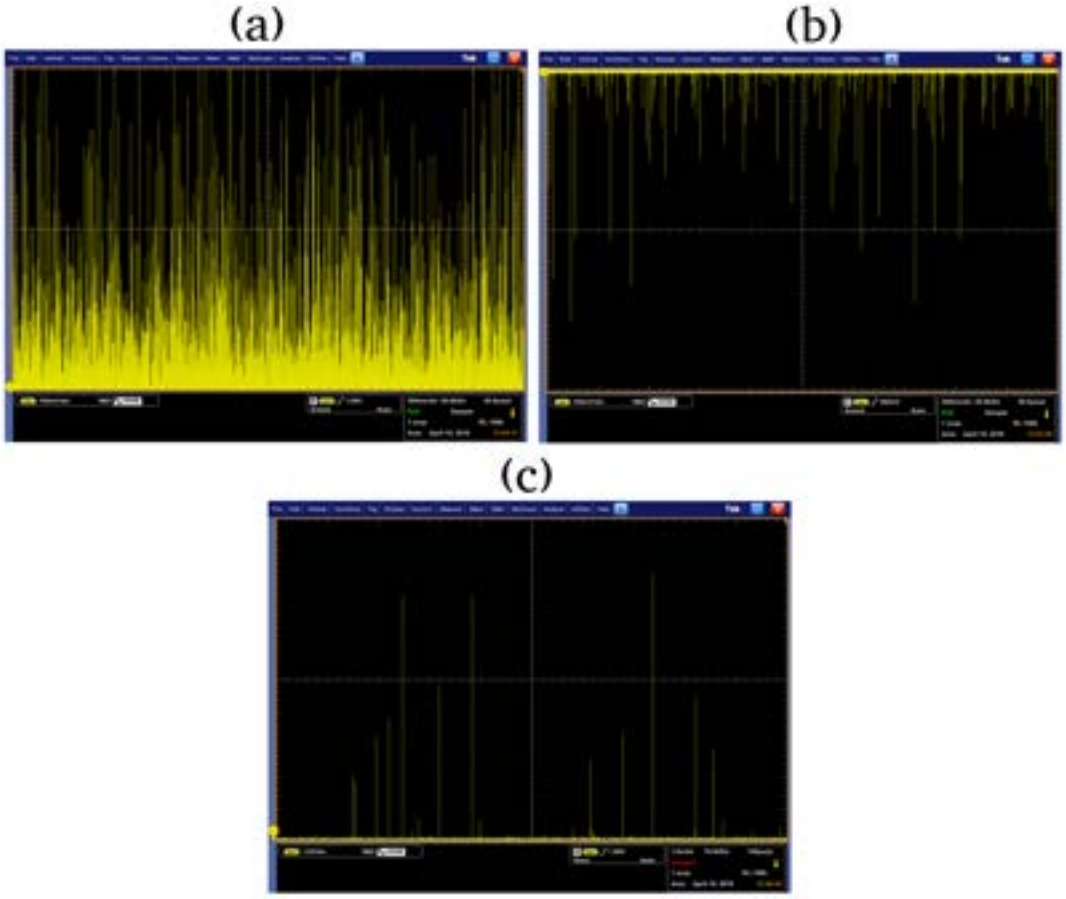

(a) Cathode output signal if 137Cs (662 keV) radiative sample source was used, (b) Anode output signal if americium was used, and (c) background noise, pre-amplifier output signal.

APPENDIX C

C.1 High-speed video observation of a dart leader producing x-rays

The first x-ray observation in Brazil is described in this article in more detail.

AGU100 ADVANCING EARTH AND SPACE SCIENCE

JGR Space Physics

RESEARCH ARTICLE
10.1029/2019JA027247

Key Points:
- First high-speed video observation of a natural lightning leader producing X-rays during its propagation to ground
- Experimental confirmation that the production of X-rays depends on the leader charge density in natural lightning
- The orientation of the leader plays an important role in the detection of X-rays

Correspondence to:
M. M. F. Saba,
marcelo.saba@inpe.br

Citation:
Saba, M. M. F., Ferro, M. A. S., Cuadros, E. T., Custódio, D. M., Nag, A., Schumann, C., et al (2019). High-speed video observation of a dart leader producing X-rays. *Journal of Geophysical Research: Space Physics*, *124*, 10,564–10,570. https://doi.org/10.1029/2019JA027247

Received 19 AUG 2019
Accepted 17 OCT 2019
Accepted article online 7 NOV 2019
Published online 13 DEC 2019

High-Speed Video Observation of a Dart Leader Producing X-rays

M. M. F. Saba[1], M. A. S. Ferro[2], E. T. Cuadros[1], D. M. Custódio[2], A. Nag[3], C. Schumann[4], V. Cooray[5], A. R. Paiva[1], P. B. Lauria[1], D. S. F. Medeiros[1], P. Hettiarachchi[5], and H. K. Rassoul[3]

[1]National Institute for Space Research, São José dos Campos, Brazil, [2]Institute of Aeronautics and Space, São José dos Campos, Brazil, [3]Florida Institute of Technology, Melbourne, FL, USA, [4]School of Geosciences, University of Witwatersrand, Johannesburg, South Africa, [5]Department of Engineering Sciences, Uppsala University, Uppsala, Sweden

Abstract This work presents the first simultaneous X-ray measurement and high-speed video observation of the propagation of a lightning leader producing X-rays. As a result, the three-dimensional leader distance from the X-ray measurement and, for the first time, the conditions of the preexisting channel during the leader propagation were observed. Although four leaders in this seven-stroke flash followed the same path to ground, X-rays were only observed during the leader before the return stroke with the highest peak current. The fact that the other three leaders following the same path to ground did not produce detectable X-rays confirms the hypothesis that leader line charge density is an important factor that determines X-ray production. The fact that X-rays was recorded only when the leader tip was at a certain portion of the lightning channel confirms that the orientation of the leader plays an important role in the detection of X-rays.

Plain Language Summary It was known that lightning can produce X-rays. However, in this study, thanks to the use of a high-speed video camera it was possible to determine when lightning produces X-rays, how far it was, how it was oriented when the detection of X-rays, and what the conditions of the preexisting channel were during the leader propagation. The observations of the present work allow for new insights, confirmation of some hypotheses, and comparison with past studies. The results presented help to understand why X-rays are sometimes detected and sometimes not. It is shown that the amount of charge transferred by the discharge plays a crucial role. This study also confirms that the orientation of the descending leader plays an important role in the detection of X-rays.

1. Introduction

Lightning emits X-rays. Although progress has been achieved in quantifying some properties of the lightning-leader X-ray emission in natural, rocket-triggered, and upward lightning (e.g., Moore et al., 2001, Dwyer et al., 2003, Dwyer et al., 2004, Dwyer et al., 2005, Dwyer et al., 2011; Saleh et al., 2009; Yoshida et al., 2008; Howard et al., 2008, Howard et al., 2010; Mallick et al., 2012; Hettiarachchi et al., 2018), it is still uncertain why not all strokes in the same flash and not all leader steps in the same stroke produce detectable X-rays.

Howard et al. (2010) reported observations of leader electric fields and generation of energetic radiation close to triggered lightning. The authors suggest that the X-ray emissions may be beamed to some degree in the direction of the leader propagation. Saleh et al. (2009) however found that their observations were most consistent with an isotropic radiation source, although they could not rule out the possibility that the emissions become slightly beamed as the leader approaches very near the ground. More recently, Dwyer et al. (2011) and Schaal et al. (2014) used a pinhole-type X-ray imaging camera in order to produce two-dimensional "photos" and "movies" of the X-ray source regions of dart leaders in triggered lightning. They found that the X-ray source is located near and descends with the leader front and that two distinct X-ray emission patterns (compact and diffuse) may be present in lightning leaders.

Montanya et al. (2012) attribute the difficulty of measuring X-rays to some beaming of the high-energy particles from the leader and to the requirement that the detectors must be close enough in order not to receive completely attenuated radiation. This may explain why the catalogue of X-ray measurements produced by

natural lightning is very small (Moore et al., 2001; Dwyer et al., 2005a; Howard et al., 2008; Howard et al., 2010; Mallick et al., 2012; Montanyà et al., 2012; Schaal et al., 2012). All these observations, except those of Mallick et al. (2012), correspond to stepped leaders, not natural dart leaders.

Furthermore, a theoretical work conducted by Cooray et al. (2010) states that charge that exists at the tip of the dart leader is responsible for driving the electrons to runaway energies, resulting in X-ray emissions. Therefore, some dart leaders may not produce X-rays at all or at least not at a detectable level.

In order to understand the mechanisms producing the X-rays and the source regions of the emissions, simultaneous recording of high-speed video of the leader together with X-ray measurements have been tried in past studies but has not been successful (e.g., Montanyà et al., 2012; Montanyà et al., 2014; Schaal et al., 2012).

This work presents the measurements of X-rays from a natural lightning dart leader. Moreover, it presents the first high-speed video observation of a leader producing X-rays during its propagation to ground. The high-speed video images in conjunction with other measurements not only made it possible to address some factors considered important in theoretical studies but also factors that affected the observation of X-rays in all previous studies such as distance, leader charge, trajectory, and channel temperature.

In contrast with previous studies, video images from different angles allowed us to calculate the three-dimensional distance from the X-ray detector and the orientation of the channel when the X-ray detector observed radiation from the leader. It also made possible to check the status of the lightning channel by knowing how many strokes and continuing current events had previously conditioned the channel. It was also possible to compare the luminosity of the dart leader producing X-rays with the other ones that did not produce any detectable radiation. The use of a fast electric-field sensor together with the estimated peak current of the prospective return stroke made possible to qualitatively estimate the charge involved in each dart leader. The reported observations have important implications for understanding why some leaders produce detectable energetic radiation and some leaders not.

2. Instrumentation

The X-ray detection system was installed inside an aluminum box of thickness 3.1 mm on the top of 50-m-tall building located in the city of São Paulo (785 m above sea level), Brazil. The detecting system was composed by a 7.6 × 7.6-cm cylindrical NaI (Tl)/Photomultiplier tube (PMT) which contained internal HV supplies and divider chains. The detector used is identical to the detector described in more detail in the papers of Saleh et al. (2009). However, as a preamplified output coming from the PMT was used instead of the direct anode output (see Saleh et al., 2009; Figure 2), the X-ray detecting system had a slower response due to the higher decay constant of the preamplifier. A fiber-optic link (a DG Instruments FOS1 with a bandwidth of 5 MHz, and input voltage ±1 V) carried the detector signal through a 120-m-long fiber optic to a data logger recording at a sampling rate of 5 MS/s. The X-ray detection system (the detector and fiber-optic transmitter) was powered by two 12-V batteries also housed inside the same aluminum box and replaced by charged ones when necessary. This arrangement guaranteed very good noise immunity.

The 5-MS/s sample rate data logger was also utilized to record the vertical electric-field measurements. In order to have time synchronization in all measurements a GPS receiver is connected to the data logger (a PC with a GPS card Meinberg GPS170PCI and a 12-bit data acquisition card NI PCI-6110).

The electric field sensor consisted of a flat plate antenna with an integrator and amplifier. It was also located at the top of the building, 3 m away from the X-ray system. A fiber-optic link was also used to transmit the signal from the integrator/amplifier to the digitizer. The bandwidth of the system ranged from 306 Hz to 1.5 MHz. The physics sign convention will be used when referring to the electric field and its change. The approach of a nearby negative leader produces positive electric field change and a negative CG return stroke produces a negative field change.

In addition to the X-rays and vertical electric field sensors, a high-speed camera and two standard speed cameras were also used. The high-speed camera used was a Phantom V711 operating at 37,819 frames per second with time interval between frames of 26.44 μs and exposure time of 26.08 μs (at the end of each frame the camera is blind for 0.36 μs due to data transfer). Each frame of the video is time stamped by means of a

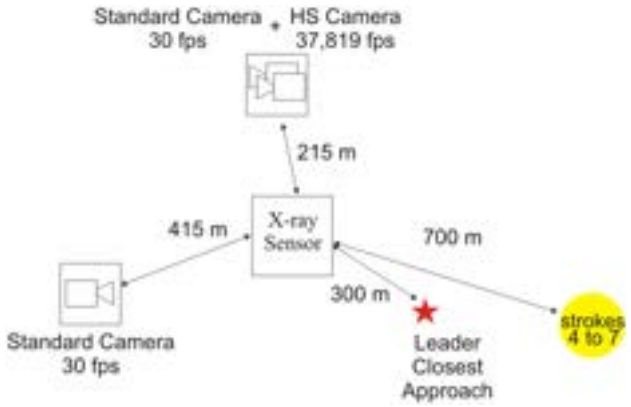

Figure 1. X-ray measurement system and the distances from cameras, from ground contact strike point of strokes 4 to 7, and from the closest segment of the lightning stroke that produced X-ray radiation. All distances are ground projection distances, except the leader closest approach distance, which is a 3-D distance.

GPS antenna. The Phantom V711 and a standard video camera (30 frames per second) were installed at a distance of 220 m from the X-ray sensor. The other standard camera was at 415 m from the X-ray sensor but at an angle of 108° with the high-speed camera (Figure 1).

Information obtained from two lightning location systems was used to estimate the location and the peak current of the return strokes. More details about these lightning location systems and their performances can be found in Naccarato and Pinto (2009) and Saba et al. (2017).

3. Data Presentation

On 16 December 2018 (18:43:37 UT) a seven stroke downward negative cloud-to-ground flash followed by a very long continuing current (lasting 630 ms) struck the ground close to the X-ray system. Some characteristics of the strokes are documented in Table 1.

The first three strokes of the seven-stroke flash followed different paths to ground. The second and the third strokes were completely out of the field of view of the cameras. The fourth leader after following the initial portion of the first return stroke channel, initiated a new path to ground and branched during its propagation. The subsequent stroke leaders used the same path to ground as the leader of the fourth return stroke but without branching and with a much higher speed. The average 2-D speed of the fourth leader and the relative average speed of subsequent leaders across the path observed by the high-speed camera are also indicated in Table 1. The X-ray detection occurred before the fifth return stroke (shown in bold numbers in Table 1) during the dart leader propagation. Upon inspecting the *E* field data during the leader propagation, we could not see a clear indication of discrete microsecond-scale electric field pulses that accompany leader steps in a dart-stepped leader. It seems that the fifth stroke may have been preceded by what is sometimes called a "chaotic leader" (as indicated in the paper of Stolzenburg et al. (2014)), although there is no branching during the occurrence of the dart leader and therefore it is not conclusive that it is a "chaotic leader."

Two lightning detection networks detected this flash. One of them (BrasilDAT) indicated the estimated peak current of each of the seven strokes. The other network (RINDAT) estimated the peak current of the first, second, and fifth strokes (indicated in brackets in Table 1). The reported peak current values by both lightning detection networks were almost identical. Based on the reported data given by the lightning detection networks and on the analysis of the images, the dart leader producing X-rays struck the ground at a distance of approximately 700 m from the X-rays detecting system (Figure 1).

Figures 2a and 2b show sequences of images of the leader propagation before the occurrence of return stroke 4 (RS 4) and return stroke 5 (RS 5), respectively. The electric field changes caused by the leaders are shown in

Table 1
Characteristics of the Return Strokes of the Negative Cloud-To-Ground Flash

Return stroke	1	2	3	4	**5**	6	7
Time of each return stroke (UT)	18:43:37 458.725	490.040	550.482	601.615	**718.067**	770.178	818.985
X-ray detection	No	No	No	No	**Yes**	No	No
Continuing current duration (ms)	8	-	-	20	**17**	35	630
Time elapsed from previous stroke (ms)	-	31	60	51	**116**	52	49
Estimated peak current (kA)	−19 (−18)	−18 (−17)	−12	−6	**−38 (−38)**	−6	−12
Leader positive field change (relative units)	498	820	88	859	**3398**	810	1064
Ground contact point	1	2	3	4	**4**	4	4
Propagation time of the leader along the visible portion of the channel (ms)	-	-	-	7.48	**0.27**	0.53	0.15
Relative speed (V_n/V_4) (V_4 is the average 2-D speed of leader preceding the fourth stroke = 49.2×10^3 m/s)	-	-	-	1.0	**28.1**	14.2	49.2

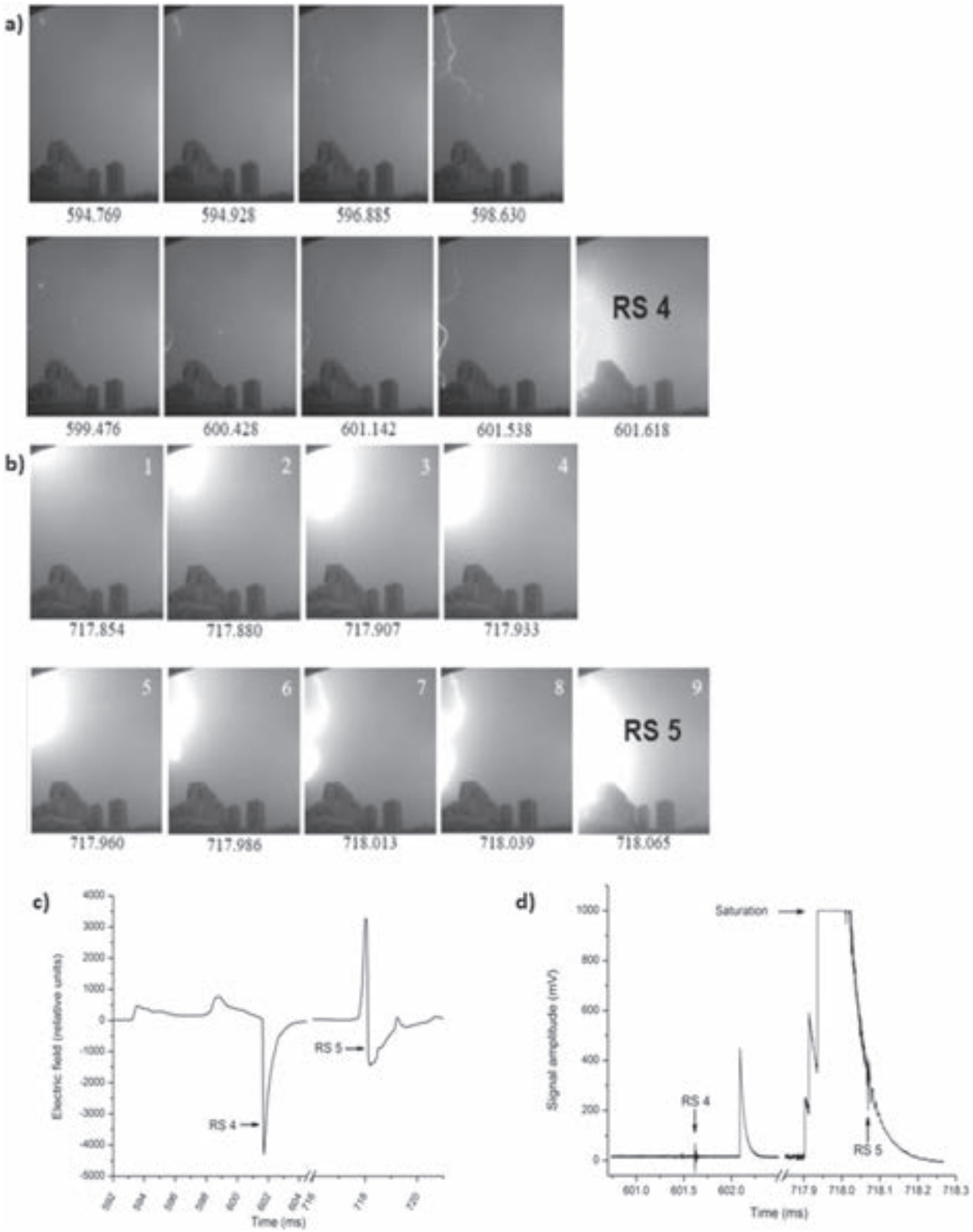

Figure 2. (a and b) Sequence of images of the leader propagation that preceded return strokes 4 and 5 and (c and d) the electric field changes and X-ray measurements before and after the return strokes. The numbers below the video images indicate the time of each frame in milliseconds at the end of the frame integration. The occurrence of the return strokes 4 and 5 and the saturation of the X-ray measurement are indicated by arrows in the plots.

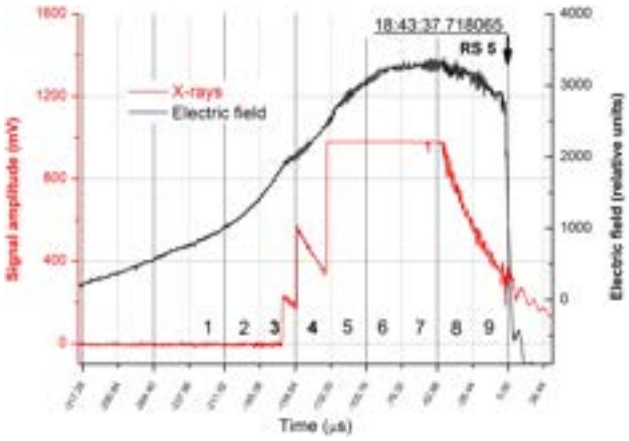

Figure 3. Electric field and X-ray measurements during the approach of the dart leader of RS 5.

Figure 2c. Both abrupt negative field changes caused by return strokes RS 4 and RS 5 are preceded by positive field changes. A long duration and small positive change due to the approach of a stepped leader precedes RS 4 and a short but intense positive change due to the dart leader precedes RS 5. The differences between the luminosity of each leader and the electric field change caused by each leader are patent. The X-ray measurements are shown in Figure 2d. Note the complete absence of X-ray detection during the leader propagation before return stroke 4. Similarly, no X-rays were detected during the propagation of the leaders that caused the other return strokes, except for stroke 5. The pulse occurring at approximately 0.5 ms after return stroke 4 in Figure 2d is a pulse of background radiation. The record of this pulse was included in the plot to illustrate how different it is from the radiation that is produced by the leader before return stroke 5. The pulses that appear at the moment of the return stroke 4 and 5, and indicated by arrows in the X-ray plot (Figure 2d), are due to the interference caused by these strokes in the data acquisition system.

In Figure 3 X-rays and the electric-field measurements are shown for the return stroke 5. The time interval between labels in the *x* axis (26.44 μs) of the graph corresponds to the time duration of each frame of the high-speed camera. Numbers 1 to 9 in the graph correspond to the nine high-speed video frames recorded during the propagation of the dart leader (shown in Figure 2). The integration of the image in frame number 9 in Figure 2 ends when the luminosity of the return stroke was already present, but not at its maximum value. Considering that (according to the lightning location system) the peak current of the return stroke occurred at 18:43:37.718067 and that the estimated zero-to-peak time was 3.7 μs, the return stroke may have started 2 or 3 ms before the end of the integration of frame 9 at 18:43:37.718065 (Figure 3).

One can observe in Figure 3 that three X-ray pulses were observed during intervals 3 and 4 (marked in bold numbers). The X-ray pulse at the end of frame interval 4 was very intense and saturated the measurement.

Figure 4 shows images of the lightning channel used by the last four strokes from two almost orthogonal standard video cameras. The numbered marks on the images show where the leader tip was at the end of the numbered intervals in Figure 3. Combining the video images of the high-speed camera and of the two almost orthogonal standard cameras it is possible to define with good approximation where the tip of the dart leader was during the detection of the X-rays.

4. Discussion

The high-speed video images showed that the first three strokes of the seven-stroke flash followed different paths to ground. All these different paths were at a greater distance from the X-ray detector than the path followed by the four last strokes. The fourth leader after following the same path as the first leader up to point indicated by the green arrow in Figure 4a, deviated from it through a new path and branched during its propagation to ground. The leader in this new path made a curve towards the X-ray detector and then away from it (Figure 4b). The following three dart leaders did not branch and followed the same path to ground as the fourth return stroke.

In previous theoretical and observational studies some features have been suggested as important factors that enable the detection of X-rays from lightning. Using the concurrent information from the high-speed images, electric-field sensor, X-ray sensor, and auxiliary cameras, four of them will be discussed: distance, leader charge, trajectory, and channel temperature.

If the X-ray source is far away from the sensor, air will attenuate the radiation and prevent any detection. This could be one of the reasons for the absence of any detection during the occurrence of the first three strokes. However, as all last four leaders followed the same path and only one of them produced detectable X-rays, trajectory, tortuosity, and distance from the sensor are not influencing the detection.

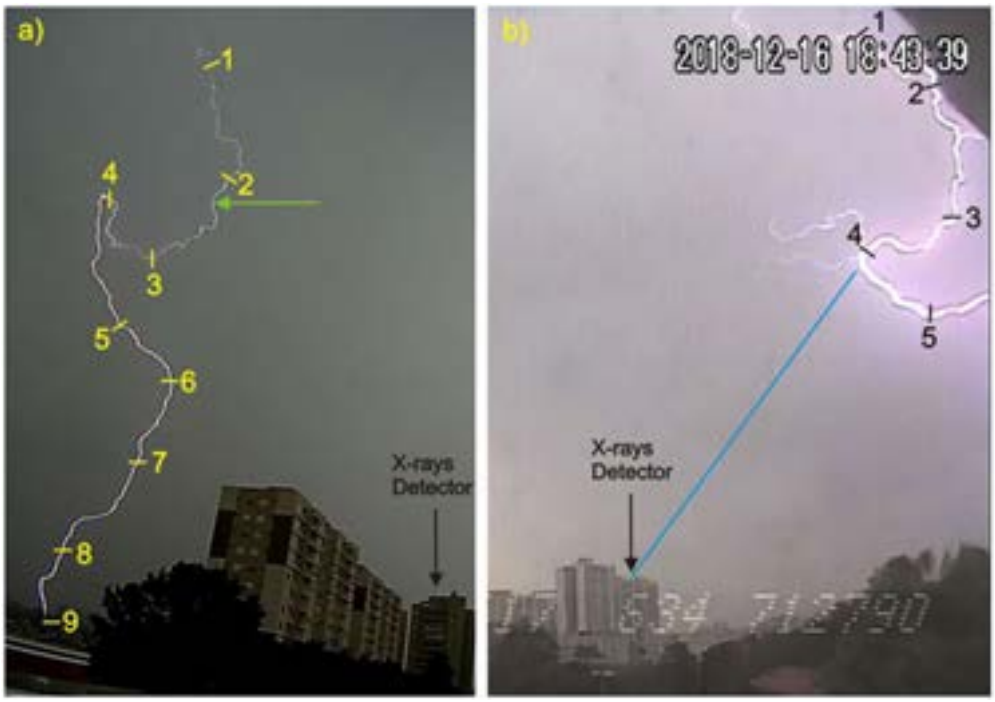

Figure 4. Images from two almost orthogonal standard video cameras. The numbered marks indicate the approximate location of the dart leader tip at the end of each video frames recorded by the high-speed camera during the fifth return stroke.

What is significantly different in the characteristics of the leader that produced X-rays is the luminosity (see Figure 2), the amplitude of the positive field change produced during the approach of the leader, and the estimated peak current of the prospective return stroke (Table 1). All these three characteristics are well associated. The return stroke peak current depends on the line charge density of the descending leader (Kodali et al., 2005), and the higher the charge is, the higher will be the current and the brighter will be the leader in the images. Therefore, high peak current return strokes are produced by highly charged and luminous leaders. We conclude that only the highly charged leader produced an electric field intense enough to produce detectable X-rays. This is an experimental confirmation, for natural lightning, of the theoretical prediction of Cooray et al. (2010) that the electric field at the tip of dart leaders is capable of producing high-energy radiation. An experimental evidence of this relationship had been previously reported by Schaal et al. (2012) for triggered lightning.

The analysis of the images also shows that during the descent of the leader of the fifth return stroke, the detection of the X-rays occurred only when the leader was at the closest distance from the detector (estimated three-dimensional distance of 300 ± 20 m). However, the leader was not only at the closest distance, but perhaps at such a position/orientation that the detector was within the X-ray flux beam as discussed by Howard et al. (2010) and Montanyà et al. (2014). Note that the most intense pulse of radiation (Figure 3) occurred when the leader was around mark 4 in Figure 4. The blue line drawn over Figure 4b connects this mark to the location of the detector on top of the building and suggests that the leader may have had been oriented towards the X-ray sensor when travelling around mark 4. Also, the abrupt rise of the X-ray intensity suggests that it was the orientation of the leader and not its distance that modulated the detected signal.

Finally, according to calculations performed by Cooray et al. (2010), the density of the defunct return stroke channel decreases with increasing temperature, and therefore, in a given dart leader electric field, the possibility of accelerating electrons to runaway mode increases with increasing temperature. They suggest that if it is higher than about 2,500 K, a typical dart leader with prospective return stroke current of 12 kA could accelerate electrons into energies in the range of MeV. Considering the long interstroke time interval (116 ms) preceding the fifth stroke, a low temperature in the defunct channel would be expected (even if

the 20-ms duration continuing current following the previous return stroke is considered; see Table 1). However, their model also predicts that this critical temperature (of 2,500 K) decreases with the increase in dart leader current (the peak of the prospective return stroke current). This may also be the case here. Therefore, our observations and measurements show that not only their hypothesis are confirmed but that the long interstroke interval, and therefore the lower channel temperature, is compensated by a relatively large leader current (as indicated by its luminosity), electric field change, and the peak current of the following return stroke (38 kA).

In conclusion, based on the simultaneous recording of high-speed video images, X-ray, and electric-field measurements we show that (a) for dart leaders following the same trajectory equally distant from the X-ray detector, only the highly charged leader will produce detectable X-rays; (b) although the leader was highly luminous (and therefore highly charged) throughout the trajectory, X-rays were recorded only when the leader tip was located at a certain portion of the lightning channel; (c) detection occurs when the leader is probably oriented toward the detector, supporting the hypothesis of a beamed X-ray flux; and (d) the measurements confirm the hypothesis by Cooray et al. (2010) that, although the possibility of accelerating electrons to runaway mode increases with increasing temperature, the lower channel temperature of a defunct channel is compensated by a relatively large leader current.

Acknowledgments
The authors would like to thank Lie L. Bie (Benny), Kleber P. Naccarato, Paulo A. L. C. B. Pino, Jorge Yamasaki, José Claudio O. Silva, Guilherme F. Aminger, and Ricardo M. B. Soares, for all the support in data acquisition. The authors would also like to thank all dwellers for allowing and supporting this research to take place in their buildings. One of the co-authors would like to thank the research grants from Claude Leon Foundation. The participation of Vernon Cooray and Pasan Hettiarachchi in the project is funded by grants 621–2003–3465 and 621–2006–4299 from the Swedish National Research Council (VR). The images, videos, and the measurements supporting the conclusions are available at http://urlib.net/rep/8JMKD3MGP3W34R/3TG44DP.

References

Cooray, V., Dwyer, J. R., Rakov, V., & Rahman, M. (2010). On the mechanism of X-ray production by dart leaders of lightning flashes. *Journal of Atmospheric and Solar-Terrestrial Physics*, *72*(11-12), 848–855. https://doi.org/10.1016/j.jastp.2010.04.006

Dwyer, J. R., Rassoul, H. K., Al-Dayeh, M., Caraway, L., Chrest, A., Wright, B., et al. (2005). X-ray bursts associated with leader steps in cloud to ground lightning. *Geophys. Res. Lett*, *32*(1), L01803. https://doi.org/10.1029/2004GL021782

Dwyer, J. R., Rassoul, H. K., Al-Dayeh, M., Caraway, M., Wright, B., Chrest, A., et al. (2004). Measurements fo X-ray emission from rocket-triggered lightning. *Geophys. Res. Lett*, *31*(5), L05118. https://doi.org/10.1029/2003GL018770

Dwyer, J. R., Schaal, M., Rassoul, H. K., Uman, M. A., Jordan, D. M., & Hill, D. (2011). High-speed X-ray images of triggered lightning dart leaders. *J. Geophys. Res.*, *116*(D20), D20208. https://doi.org/10.1029/2011JD015973

Dwyer, J. R., Uman, M., Rassoul, H. K., Al-Dayeh, M., Caraway, M., Jerauld, J., et al. (2003). Energetic radiation produced during rocket-triggered lightning. *Science*, *299*(5607), 694–697. https://doi.org/10.1126/science.1078940

Hettiarachchi, P., Cooray, V., Diendorfer, G., Pichler, H., Dwyer, J., & Rahman, M. (2018). X-ray observations at Gaisberg Tower. *Atmosphere*, *9*(1), 20. https://doi.org/10.3390/atmos9010020

Howard, J., Uman, M. A., Biagi, C., Hill, D., Jerauld, J., Rakov, V. A., et al. (2010). RF and X-ray source locations during the lightning attachment process. *Journal of Geophysical Research*, *115*(D6). https://doi.org/10.1029/2009JD012055

Kodali, V., Rakov, V. A., Uman, M. A., Rambo, K. J., Schnetzer, G. H., Schoene, J., & Jerauld, J. (2005). Triggered-lightning properties inferred from measured currents and very close electric fields. *Atmospheric Research*, *76*(1-4), 355–376. https://doi.org/10.1016/j.atmosres.2004.11.036

Mallick, S., Rakov, V. A., & Dwyer, J. R. (2012). A study of X-ray emissions from thunderstorms with emphasis on subsequent strokes in natural lightning. *Journal of Geophysical Research*, *117*, D16107. https://doi.org/10.1029/2012JD17555

Montanyà, J., Fabró, F., van der Velde, O. A., Romero, D., Solà, G., Hermoso, J. R., et al. (2014). Registration of X-rays at 2500 m altitude in association with lightning flashes and thunderstorms. *Journal of Geophysical Research*, *119*. https://doi.org/10.1022/2013JD021011

Montanyà, J., O.A. van der Velde, V. March, D. Romero, G. Solà, N. Pineda, (2012), High-speed video of lightning and X-ray pulses during the 2009-2010 observation campaigns in northeastern Spain. *Atmospheric Research*, *117*, D16107. https://doi.org/10.1016/j.atmosres.2011.09.013, 91, 98

Moore, C. B., Eack, K. B., Aulich, G. D., & Rison, W. (2001). Energetic radiation associated with lightning stepped-leaders. *Geophys. Res. Lett.*, *28*(11), 2141–2144. https://doi.org/10.1029/2001GL013140

Naccarato, K. P., & Pinto, O. Jr. (2009). Improvements in the detection efficiency model for the Brazilian lightning detection network (BrasilDAT). *Atmos. Res.*, *91*(2-4), 546–563. https://doi.org/10.1016/j.atmosres.2008.06.019

Saba, M. M. F., Paiva, A. R., Schumann, C., Ferro, M. A. S., Naccarato, K. P., Silva, J. C. O., et al. (2017). Lightning attachment process to common buildings. *Geophys. Res. Lett.*, *44*(9), 4368–4375. https://doi.org/10.1002/2017GL072796

Saleh, Z., Dwyer, J., Howard, J., Uman, M., Bakhtiari, M., Concha, D., et al. (2009). Properties of the X-ray emission from rocket-triggered lightning as measured by the Thunderstorm Energetic Radiation Array (TERA). *Journal of Geophysical Research*, *114*(D17), D17210. https://doi.org/10.1029/2008JD011618

Schaal, M. M., Dwyer, J. R., Arabshahi, S., Cramer, E. S., Lucia, R. J., Liu, N. Y., et al. (2014). The structure of X-ray emissions from triggered lightning leaders measured by a pinhole-type X-ray camera. *J. Geophys. Res. Atmos.*, *119*(2), 982–1002. https://doi.org/10.1002/2013JD020266

Schaal, M. M., Dwyer, J. R., Saleh, Z. H., Rassoul, H. K., Hill, J. D., Jordan, D. M., & Uman, M. A. (2012). Spatial and energy distributions of X-ray emissions from leaders in natural and rocket triggered lightning. *J. Geophys. Res.*, *117*(D15), D15201. https://doi.org/10.1029/2012JD017897

Stolzenburg, M., Marshall, T. C., Karunarathne, S., Karunarathna, N., & Orville, R. E. (2014). Branched dart leaders preceding lightning return strokes. *J. Geophys. Res. Atmos.*, *119*(7), 4228–4252. https://doi.org/10.1002/2013JD021254

APPENDIX D

D.1 Codes

Here we show some code developed: Monte Carlo to model the propagation of the leader, IDL to make the comparison of the modeled and registered data, and finally the 33MS/s PXI data reading code (data processing) in Python.

```
pro mainream
;++++++++++++++++++++++++++++++++++++++++
; modified by Edith Tueros Cuadros &
; Dr.Joseph Dwyer
;++++++++++++++++++++++++++++++++++++++++
filename00 = "Xray"
Efield00 = [0.0]
Bfield00 = [0.0]
;-----------------------------------------------------------------------
;-----------------------------------------------------------------------
pointsxyz_filename = 'F:\REAM\Data_XYZ.txt'
openr, lun, pointsxyz_filename, /get_lun

xstart = fltarr(125)
ystart = fltarr(125)
zstart = fltarr(125)
xstart0 = data(0,*)
ystart0 = data(1,*)
zstart0 = data(2,*)
for i=0,124 do begin
    readf, lun, xx, yy, zz
    xstart[i] = xx
    ystart[i] = yy
    zstart[i] = zz
endfor
free_lun, lun
print, N_elements(xstart), xstart(0), xstart(-1)
print, n_elements(xstart0), xstart0(0), xstart0(-1)

n = n_elements(xstart)
nxstart = fltarr(n)
nystart = fltarr(n)
nzstart = fltarr(n)
tstart = fltarr(n)
dis = fltarr(n)
;-----------------------------------------------------------------------
; Average speed
```

```
;-------------------------------------------------------------------
v = [replicate(double(1.6E6),125)] ;average speed (m/s)
;-------------------------------------------------------------------
for xx=0,n-2 do begin
    dis(xx) = sqrt((double(xstart(xx+1))- double(xstart(xx)))^2+
    (double(ystart(xx+1))-double(ystart(xx)))^2 &+
    (double(zstart(xx+1))-double(zstart(xx)))^2)

    ;-------------------------------------------------------------------
    ; Time
    ;-------------------------------------------------------------------
    tstart(xx+1) = tstart(xx)+ dis(xx)/v(xx)
    ;-------------------------------------------------------------------
    nxstart(xx+1) = double(xstart(xx+1)) - double(xstart(xx))
    nystart(xx+1) = double(ystart(xx+1)) - double(ystart(xx))
    nzstart(xx+1) = double(zstart(xx+1)) - double(zstart(xx))
    norm1 = sqrt(nxstart(xx+1)*nxstart(xx+1)+nystart(xx+1)*
    nystart(xx+1)+nzstart(xx+1)*nzstart(xx+1))

    nxstart(xx+1)=nxstart(xx+1)/norm1
    nystart(xx+1)=nystart(xx+1)/norm1
    nzstart(xx+1)=nzstart(xx+1)/norm1
endfor

nxstart(0)=nxstart(1)
nystart(0)=nystart(1)
nzstart(0)=nzstart(1)
;-------------------------------------------------------------------
;-------------------------------------------------------------------
nfiles = n_elements(xstart)
nfilesB = n_elements(Bfield00)
lam00 = 7300.0/(Efield00-276.0*0.9413)
L00 = 7.0*lam00
nphotons_1MeV=0L
grammage1all = fltarr(10)
grammage2all = fltarr(10)

for j = 0,nfiles-1 do begin
    for kkk = 0,nfilesB-1 do begin
        Bfield000 = Bfield00(kkk)

        nelectrons_1MeV = 1.0;
        Efield000 = Efield00(0)*1000.0
        L000 = L00(0)

```

```
83          filename = filename00+STRTRIM(String(fix(Efield00(0))),2)+'
    _'+
84          STRTRIM(String(j),2)
85          print, filename,' ',j
86          for k = 1,1 do begin
87              if (k eq 0) then Efield000 = Efield000 ;700000.0 ; use
    this when
88              propagating to space
89              if (k eq 1) then Efield000 = 0.0
90              ;
    ----------------------------------------------------------------
91              xstartin = xstart(j)
92              ystartin = ystart(j)
93              zstartin = zstart(j)
94              tstartin = tstart(j)
95              nxstartin=nxstart(j)
96              nystartin=nystart(j)
97              nzstartin=nzstart(j)
98              ;
    ----------------------------------------------------------------
99              ream,
100             Efield000,Bfield000,L000,filename,0,nphotons_1MeV,
101             nelectrons_1MeV,0,0.0,grammage1,&grammage2,tstartin,
102             xstartin,ystartin,zstartin,nxstartin,nystartin,
    nzstartin
103             ;
    ----------------------------------------------------------------
104         endfor
105     endfor
106 endfor
107
108 stop
109 end
110 @ream
```

Code D.1 - IDL Code 1

```
1 ;pro Comparation_Edith
2 ;+++++++++++++++++++++++++++++++++++++++++
3 ; Author : Edith Tueros Cuadros
4 ;+++++++++++++++++++++++++++++++++++++++++
5 file_in= 'E:\data2\5RS.txt'
6 d=read_ascII(file_in, DATA_START=1, HEADER=str_data, count=nr)
7 data=d.(0)
8 tempo = data(0,*)
9 c4 = data(1,*)
```

```
c5 = data(2,*)
c6 = data(3,*)

id = where(tempo ge 37.717853 and tempo lt 37.719205, count) ;
   37.718170 s -->
%dos dados (no gr fico)
tempo_new = tempo(id)
;================================================================
;Model 1
;add = (3.7718200000000000306e+01 - 37.717853)/124 ; (Final time -
   Start Time)/
(n-1)
;time=DINDGEN(125, increment=add , start=37.717853)
;print, time(0), time(-1)
;considering camera time
;================================================================
;Model 2
; Considering the calculated time variation between points:
;time=DINDGEN(125, increment=0.0000002 , start=37.717853)
;print, time(0), time(-1)
;================================================================

Modelo 3
add = (37.718170 - 37.717853)/124 ; (Final Time - Start Time)/(n-1)
time=DINDGEN(125, increment=add , start=37.717853)
print, time(0), time(-1)
print, add
;Considering X-ray time and electric field
;================================================================
c4_new = c4(id)
c5_new = c5(id)
c6_new = c6(id)

restore, 'Xray_102TIME.hitp';,/v
tm = tstart ; tempo
;print,tm(0)
restore, 'testedith.save';, /v
mm = valor ; mean value
tm_new = tm + double(time)
;================================================================
; Plot
; ================================================================
set_plot, 'ps'
device, filename ='testando_5_Modelo1.ps'
device,/portrait
```

```
device,/color
!p.charsize=1
!p.multi=[0,1,3]

loadct,39
plot, tempo_new, c6_new, ystyle=0, /nodata, title='c6', xtitle='
    time (s)', $
XTICKINTERVAL = 0.00005, xtickformat='(3F0)'
axis, yaxis=1, /save, /ystyle, yrange=[0,40000], ytitle='c6 (orange
    )'
oplot, tempo_new, c6_new, color=215, linestyle=0, thick=3
axis, yaxis=0, /save, /ystyle, yrange=[0,60000], ytitle= 'mm (blue)
    '

oplot, tm_new, mm, color=90, linestyle=0, thick=3
oplot, [37.718069,37.718069], [0,60000], linestyle=2, color=0,
    thick=1

loadct,39
plot, tempo_new, c5_new, ystyle=4, /nodata, title='c5', xtitle='
    time (s)', $
XTICKINTERVAL = 0.00005, xtickformat='(3F0)'
axis, yaxis=1, /save, /ystyle, yrange=[0,40000], ytitle='c5 (purple
    )'
oplot, tempo_new, c5_new, color=20, linestyle=0, thick=3
axis, yaxis=0, /save, /ystyle, yrange=[0,60000], ytitle= 'mm (blue)
    '
oplot, tm_new, mm, color=90, linestyle=0, thick=3

oplot, [37.718069,37.718069], [0,60000], linestyle=2, color=0,
    thick=1

plot, tempo_new, c4_new, ystyle=4, /nodata, title='c4', xtitle='
    time (s)', $
XTICKINTERVAL = 0.00005, xtickformat='(3F0)'
axis, yaxis=1, /save, /ystyle, yrange=[0,6000], ytitle='c4 (red)';,
ytickformat='(I04)'
oplot, tempo_new, c4_new, color=250, linestyle=0, thick=3
axis, yaxis=0, /save, /ystyle, yrange=[0,60000], ytitle= 'mm (blue)
    ';,
ytickformat='(I04)'
oplot, tm_new, mm, color=90, linestyle=0, thick=3

oplot, [37.718069,37.718069], [0,60000], linestyle=2, color=0,
    thick=1
```

```

device, /close
end
```

Code D.2 - IDL Code 2

```
"""
++++++++++++++++++++++++++++++++++++++++++
Author : Edith Tueros Cuadros

++++++++++++++++++++++++++++++++++++++++++
"""
%matplotlib nbagg
import matplotlib.pyplot as plt
import numpy as np
import pandas as pd
from nptdms import TdmsFile
from nptdms import tdms
from glob import glob
import datetime as dt
import dask.array as da
"""
=========================================
                READ DATA TDMS -PXI
=========================================
"""
tdms_file = TdmsFile.read('/media/edith/EDITH-SMASU/SP-PXI
    /2019-01-24/PXI/20190124_175220_076_PXI-5105.tdms')

for name, value in tdms_file.properties.items():
    print("{0}: {1}".format(name, value))

#-----------------------------------------------
tdms_groups = tdms_file.groups()
tdms_groups
"""
-----------------------------------------------
   Show Channels
-----------------------------------------------
"""
channel_0 = tdms_file['PXI-5105-Ch0']['Frame_1']
channel_1 = tdms_file['PXI-5105-Ch1']['Frame_1']
channel_2 = tdms_file['PXI-5105-Ch2']['Frame_1']
channel_3 = tdms_file['PXI-5105-Ch3']['Frame_1']
channel_4 = tdms_file['PXI-5105-Ch4']['Frame_1']
channel_5 = tdms_file['PXI-5105-Ch5']['Frame_1']
```

```
channel_6 = tdms_file['PXI-5105-Ch6']['Frame_1']

data_0 = np.array(channel_0.data)
data_1 = np.array(channel_1.data)
data_2 = np.array(channel_2.data)
data_3 = np.array(channel_3.data)
data_4 = np.array(channel_4.data)
data_5 = np.array(channel_5.data)
data_6 = np.array(channel_6.data)
print ("Tamanho dos dados")
print (len(data_0))
print (len(data_1))
print (len(data_2))
print (len(data_3))
print (len(data_4))
print (len(data_5))
print (len(data_6))
data_0 [0:10]
"""
++++++++++++++++++++++++++++++++++++++
    Extract Time Stamp
++++++++++++++++++++++++++++++++++++++
 Extraindo o TimeStamp do inicio de asquisi  o do arquivo
StartTime = tdms_file.properties['Timestamp']
----------------------------------------
  TIME
----------------------------------------
"""
Time = np.arange(0,1.,1/33e6)-0.05 + 20.076004933
print (len(Time))
print (len(data_0))
++++++++++++++++++++++++++++++++++++++
   Parameters to be taken into account
++++++++++++++++++++++++++++++++++++++
"""
data_0_corre = (data_0)/500.
data_1_corre = (data_1)/500.
data_2_corre = (data_2)/15.8
data_3_corre = (data_3)/15.8
data_4_corre = (data_4)*1.
data_5_corre = (data_5)*1.
data_6_corre = (data_6)*1.
"""

----------------------------------------
Find max and min
```

```
85 ---------------------------------------
86 """
87 valu = data_4_corre
88 x = valu
89 ind = detect_peaks(x, mph=410, mpd=7600, show=True)
90 print(ind)
91 #---------------------------------------
92
93
94 def myfigstyle():
95     # Reference:
96     # http://space.mit.edu/home/turnerm/python.html
97     plt.rcParams['axes.titlesize'] = 15
98     plt.rcParams['axes.labelsize'] = 13
99     #plt.rcParams['legend.fontsize'] = 11
100    plt.rcParams['path.simplify']    = True
101    #plt.rcParams['figure.figsize'] = 7,6
102    #plt.rcParams['font.family']  = 'monospace'
103    plt.rcParams['mathtext.fontset'] = 'custom'
104    plt.rcParams['xtick.major.size'] = 7
105    plt.rcParams['ytick.major.size'] = 7
106    plt.rcParams['xtick.minor.size'] = 3
107    plt.rcParams['ytick.minor.size'] = 3
108    plt.rcParams['xtick.major.width'] = 1
109    plt.rcParams['ytick.major.width'] = 1
110    plt.rcParams['xtick.minor.width'] = 1
111    plt.rcParams['ytick.minor.width'] = 1
112    plt.rcParams['lines.markeredgewidth'] = 1
113    plt.rcParams['legend.numpoints'] = 1
114    plt.rcParams['legend.frameon'] = False
115    plt.rcParams['legend.handletextpad'] = 0.3
116    plt.rcParams['xtick.minor.visible'] = True
117    plt.rcParams['ytick.minor.visible'] = True
118    #plt.rcParams['grid.color'] = 'k'
119    plt.rcParams['grid.linestyle'] = ':'
120    plt.rcParams['grid.linewidth'] = 0.5
121    #grids
122    plt.rcParams['xtick.direction'] = 'in'
123    plt.rcParams['ytick.direction'] = 'in'
124    #start sticks
125    #plt.rcParams['xtick.top'] = True
126    #plt.rcParams['ytick.right'] = True
127    # restore defaults
128    # plt.rcdefaults()
129 myfigstyle()
```

```
#_______________________________________
fig, ax1 = plt.subplots()

plt.plot(Time, data_4_corre,'r-', label='Electric Field - (V/m)')
plt.grid()
plt.legend()

plt.show()
#_______________________________________
```

Code D.3 - Python Code 3